Photon Management on a Photonic Crystal Platform

POLITECNICO DI TORINO

DISAT - Dipartimento di Scienza Applicata e Tecnologia

Dottorato in Dispositivi Elettronici XXVII Ciclo

Photon management assisted by Bloch Surface Waves on one dimensional photonic crystals

Tesi di dottorato

Relatori

Prof. Emiliano Descrovi

Prof. Fabrizio Giorgis

Co-relatori

Dr.ssa Natascia De Leo

Dr. Luca Boarino

Candidato

Angelo Angelini

Che cosa è verità? Inerzia; l'ipotesi che ci rende soddisfatti;
il minimo dispendio di forza intellettuale.
Friederich Nietzsche

Contents

Introduction

In the recent past, the emerging field of nanotechnologies has stimulated intense research efforts, since it holds promise for opening new scenarios in a wide variety of fields. Although *"this field [...] will not tell us much more about fundamental physics"*, as stated by Feynman in 1959, *"it might tell us much more about all the strange phenomena that occur in complex situations. Furthermore [...] it would have an enormous number of technical applications"*. As expected by Feynman, fifty years later nanotechnologies have become pervasive in almost all the research fields, from biology to medicine, from material sciences to information technologies just to give few examples.

Within the world of nanotechnologies, nanophotonics and, more generally, technologies devoted to the manipulation of light have gained relevance in several fields. The conversion of far-field electromagnetic radiation into localized energy as well as the control of the radiation angular pattern of energy emitted by localized sources is of outstanding relevance in a wide variety of fields.

Nowadays a plethora of wireless applications make use of antennas to transmit and receive informations, from satellite communications to mobile phones. The extension of this concept to the visible regime has led to develop the idea of optical antennas.

A general concept in antennas theory is the scalability of parameters, that is the antenna parameters are determined by the wavelength of incident radiation. For a long time, the main challenge in designing antennas for visible light has been related to fabrication capabilities, since the typical size of an optical antenna should be of the order of tens of nanometers, with a resolution of few nanometers.

Before the introduction of fabrication techniques such as Electron

Beam Lithography (EBL) or Focused Ion Beam Lithography (FIB), the main road followed to manipulate the visible light has been the use of Photonic Crystals (PCs). PCs are periodic dielectric structures whose periodicity is of the order of visible wavelengths. The ability of controlling the propagation of light by employing such structures has been known for more than one century and, although the promising results and the wide employment of PCs in many applications, the request for confining the electromagnetic energy in deep-subwavelength volumes as well as the growing capability of fabricating objects at the nanometric scale with a resolution of few nanometers has opened the novel field of nanophotonics.

A wide variety of optical antennas have been proposed in the recent past, based on dielectric and metallic nanostructures. Particular attention have gained the metallic ones, since the exploitation of Surface Plasmon Resonances allows for confining the electromagnetic field in deep subwavelength volumes and allows for controlling the radiation patter, making such structures effective optical antennas. The compression of the electromagnetic field in small volumes allows to greatly enhance the light-matter interaction. Unfortunately, SPR relies on the oscillations of free electrons in metal, and such phenomenon is intrinsically affected by the scattering of electrons with metallic ions. The scattering results in ohmic losses that affect the performances of such devices.

The subject of this thesis is the attempt to overcome some of the limitations of the two approaches presented by employing properly designed one dimensional photonic crystals sustaining Bloch Surface Waves (BSWs), i.e. surface electromagnetic waves, that enable the conversion of free space radiation into localized energy and vice versa.

The first chapter deals with a brief description of the basic principles underlying the physics of BSWs on 1DPC. In the second chapter, I will show that surface relief structures with deep sub-wavelength thickness are an effective way to manipulate radiation coupled to the surface modes sustained by the photonic crystal. The third chapter will deal with the so called Bloch Surface Wave Coupled Emission (BSW-CE), that is the natural coupling of light emitters with BSW, that results in a reshape of the radiation pattern and in a highly directional fluorescence beam. The fourth and fifth chapters will discuss the use of surface diffraction gratings to manipulate BSW-coupled flu-

orescence and redirect it in preferred directions. In particular, in the fourth chapter a sensing implementation of the directional extraction of fluorescence will be presented, while in the fifth, the beaming of fluorescence radiated from localized sources will be discussed.

Chapter 1

Bloch Surface Waves on a one dimensional photonic crystal

1.1 Photonic Crystals, photonic band structure and photonic band gap

The first observations of Lord Rayleigh about the reflective properties of certain crystals of chlorate of potash in 1888,[1] led him to hypotize that *"on the whole, the character of the reflected light appears to me to harmonize generally with the periodical theory"*. The wave-like nature of light is indeed fully coeherent with the observation of interference effects in periodic structures or in thin film, such as iridescence in natural systems. Unfortunately, at that time Lord Rayleigh could only hypotize the effect of periodicity on the photonic properties of crystals. Nowadays, it is known that also many biological systems exploit a sub-micrometric structuration of dielectric materials in order to take advantage of their photonic properties.[2,3]

When, some decades later, the theory of quantum mechanics successfully explained the propagation of electrons in a crystal lattice in terms of travelling waves in a periodic potential by means of the Bloch Theorem, the same picture was ready to be applied to the propagation of photons in photonic crystals.[4] When the ionic potential, that in solids gives rise to the electronic band structure, is replaced by the dielectric function and the electronic wavefunction is replaced with an electromagnetic wave, a periodic dielectric structure produces a photonic band structure. The periodicity of the refractive index

may concern one, two or three directions, and the systems associated are consequently called one, two or three dimensional photonic crystals, as sketched in fig. 1.1. The dimensionality of the photonic band structure reflects the dimensionality of the periodicity of the dielectric function.

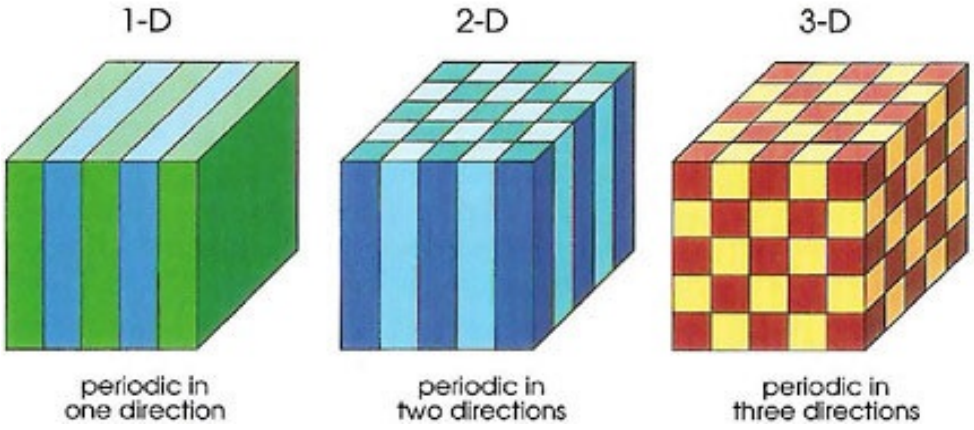

Figure 1.1: Schematic view of photonic crystals with different dimensionality.

Many of the most remarkable effects in crystalline structures are related with the formation of forbidden gaps within the band structure (fig. 1.2). The high reflectivity along certain directions of different wavelengths, as the one observed by Rayleigh in the crystals of chlorate of potash, can be explained by looking at the dispersion diagram of the crystals. The ability of structuring the dielectric function at the optical wavelengths scale allows for a certain degree of manipulation of light, as well as the ability of controlling the crystalline structures of solids allows for controlling the electronic properties of solids. For example, the ability of controlling the photonic disperison relation allowed to fabricate structures capable of slowing down light.[5,6]

The increased capability, in the last decades, to fabricate structures at the nanoscale and the high degree of control of material properties achieved by modern deposition systems has led to a plethora of photonic applications based on the control of the dispersion relation of light in solids, such as laser technology,[7] lighting systems[8] and many others.[9,10]

Trapping states, i.e. evanescent states within the photonic band gap, can be eventually created by inserting defects in the crystalline

structure.[11] In this case it is possible, by properly tailoring the defect dimensions, to confine photons inside an optical cavity.[12] Photon confinement means that the energy density function shows the maximum of intensity inside the cavity and an exponentially decaying profile in all directions. When properly tailored, such confined states can resonate at specific wavelengths with extremely high Q-factors, increasing significatively the Local Density of Electromagnetic States (LDOS).[13] Such effect can be exploited to control spontaneous emission.[14,15]

When an emitter is placed inside the optical cavity, the emission can be enhanced or suppressed in the ideal case of a photonic bandgap.[16] The influence of the photonic environment on the emitting properties of spontaneous emitters is also known as the Purcell effect,[17] and it may concern both the radiation pattern and the decay time.

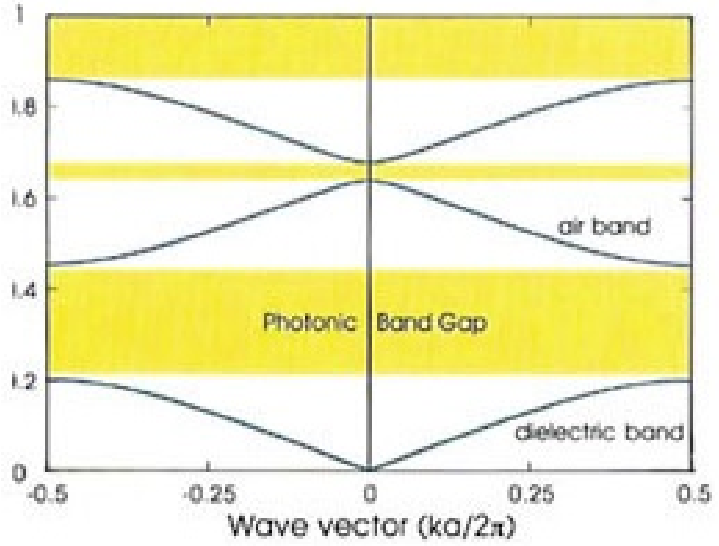

Figure 1.2: Exemplary dispersion diagram associated to a photonic crystal exhibiting a photonic band gaps.

1.2 Bloch Surface Waves: general properties

In the following, we will focus on one dimensional photonic crystals (1DPCs). A 1DPC is a periodic stack of dielectric thin films

with alternating high and low refractive index layers. Such system, also known as Bragg Mirror, always supports a forbidden band, or stop-band, in a certain wavelength-wavevector range.[4] If we consider a wavelength range for which the photonic crystal stop-band lies beyond the light line, such system may support resonant surface electromagnetic modes,[18–20] that we call Bloch Surface Waves (BSWs). The propagation of such mode in the direction normal to the 1DPC surface is prohibited both in the external dielectric medium (because of TIR) and in the multilayer, since it lyes within the stop-band.

BSWs are characterized by a well defined dispersion relation and polarization and by a field distribution exhibiting the maximum of intensity at the 1DPC/dielectric interface. Moreover the wavevector component perpendicular to the surface is complex both in the dielectric medium and in the multilayer, and, because of the above mentioned reasons, BSWs can be considered as the photonic counterpart of Surface Plasmon Polaritons (SPPs), although the physics is completely different: in the case of a metallic surface, the localization of the field at the metal/dielectric interface is due to a negative dielectric constant in the metal,[21] while BSWs localization occurs because of interference effects in the 1DPC.[22]

Due to the phenomenological analogy among SPPs and BSWs, many of the concepts and methods that apply to SPPs can be imported when dealing with BSWs, as will be evident in the following where literature about SPPs will support our hypothesis about BSWs. Compared to SPPs, BSWs exhibit some inherent advantages, mainly related to the lack of ohmic losses. This leads to higher quality factor resonances with consequently longer typical propagation distances.[23] A wide spectral tunability from UV[24] to IR,[25] polarization selection, the use of functional dielectric materials[26] can be further considered as advantages in particular applications.

In the ideal case of a semi-infinte 1DPC, the reflectivity inside the forbidden band is 1. In real systems with a finite number of layers, an evanescent tail is always crossing the Bragg Mirror, giving rise to a non-perfect reflectance. Such evanescent tail allows to couple the far-field radiation to BSW whenever the substrate has a refractive index higher than the effective index of BSW.[27]

Till now, I've briefly discussed general properties of 1DPC. Let's now consider a specific layout of 1DPC (fig. 1.3a). The photonic

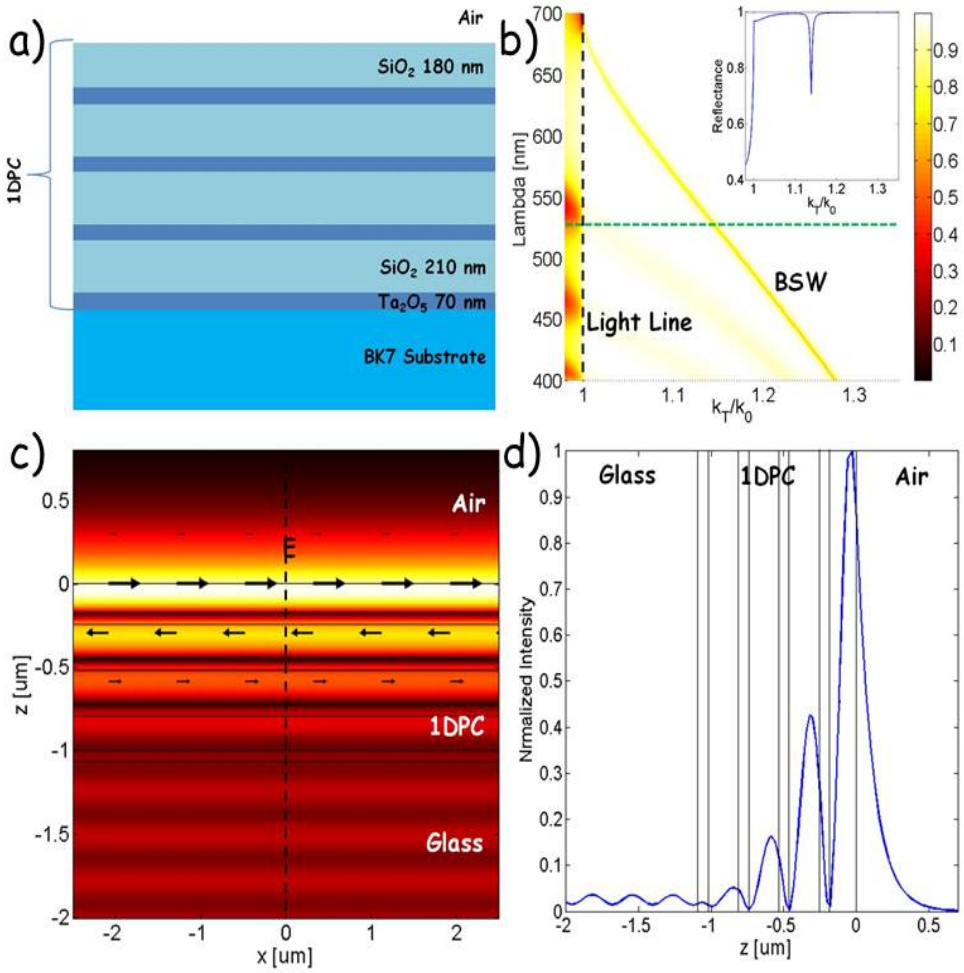

Figure 1.3: (a) Cross-sectional view of the 1DPC grown on a glass substrate. (b) Calculated TE reflectance map as function of λ and θ. The inset shows an intensity profile extracted along the green dashed line (at $\lambda = 532nm$). (c) Electric field distribution across the multilayer of the BSW mode calculated at $\lambda = 532nm$. The black arrows indicate the in-plane orientation of the electric field. (d) Normalized intensity profile of the electric field extracted along the black dashed line in (c).

crystal we will employ in the following is a stack of Ta_2O_5 ($n_h = 2.08 + i2e-4$) and SiO_2 ($n_l = 1.45 + i2e-4$) thin films deposited on a glass coverslip (BK7, $n_{sub} = 1.5$, thickness 150 μm)by plasma ion-assisted deposition under high vacuum conditions (APS904 coating system, Leybold Optics). The high and low refractive index layers have a thickness of 70 nm and 210 nm respectively and there are 3 pairs of layers, whereas the fourth pair is terminated with a layer of SiO_2 180 nm thick.

The reflectance map associated to the described photonic structure

has been calculated by Transfer Matrix Method (TMM). Basically, a TE polarized plane wave coming from a semi-infinite glass substrate impinges at specific angles on the multilayer. The TE reflectance map (fig. 1.3b) function of (λ,θ) shows that, beyond the light line and in the visible range, a narrow dispersed dip in reflectance appears. The dip is associated with the transfer of energy from the incoming plane wave to the surface mode, that propagates along the truncation interface with a wavevector that is given by the following relation:

$$k_{BSW} = k_0 n_{sub} sin(\theta_{BSW}) \tag{1.1}$$

where k_0 is the free space wavevector and θ_{BSW} is the coupling angle.

In the inset of fig. 1.3b, a cut of the map at fixed wavelength ($\lambda = 532nm$, along the green dashed line), shows that the resonance has a Full Width Half Maximum (FWHM) of 0.006 in terms of effective index of the mode, corresponding to 0.53 degrees. The width of the resonance is ultimately associated to the overall losses and, consequently, to the decay length of the mode. This point will be discussed further in detail in Chapter 2. To check the validity of our calculations, we compared the TMM results with a finite element method (FEM) model implemented in a commercial software (COMSOL Multiphysics 4.2a, RF Module). In this model a cross section of the 1DPC is considered (fig. 1.3c) and a modal analysis of the structure has been performed by imposing periodic conditions (continuity) at the left and right boundaries, and scattering condition with null incident electric field at the top and bottom boundaries. Among the different modes sustained by the structure, we found a TE polarized mode (black arrows show the orientation of the electric field) with the maximum of intensity in close proximity with the truncation interface (shown in fig. 1.3c). This mode has an effective index (at $\lambda = 532nm$) of 1.138, which is in very good agreement with the value found with the TMM method. A cross section of the electric field distribution along the structure (1.3d) puts in evidence that the mode has its maximum in close proximity to the truncation interface and that it is exponentially decaying in the outer dielectric medium. Within the multilayer, the envelop of the fringes has an exponentially decaying profile as well, while the radiation reaching the substrate (leakage radiation) shows a propagative behaviour without attenuation.

Due to the evanescent nature of BSWs, it is not possible to directly couple freely propagating light in air to BSW both in excitation and in collection. Since the BSW momentum is larger than the free-space momentum, a strategy to increase the momentum of the incident light is required. A simple strategy, widely used also in plasmonics, is to couple the 1DPC with a prism, as in the Rather Kretschmann or in the Otto configuration. By using a near field probe it is also possible to excite the evanescent modes[28] as well as to collect the evanescent optical fields directly on the flat surface of 1DPC, providing amplitude[29] and eventually phase[30] distribution of light.

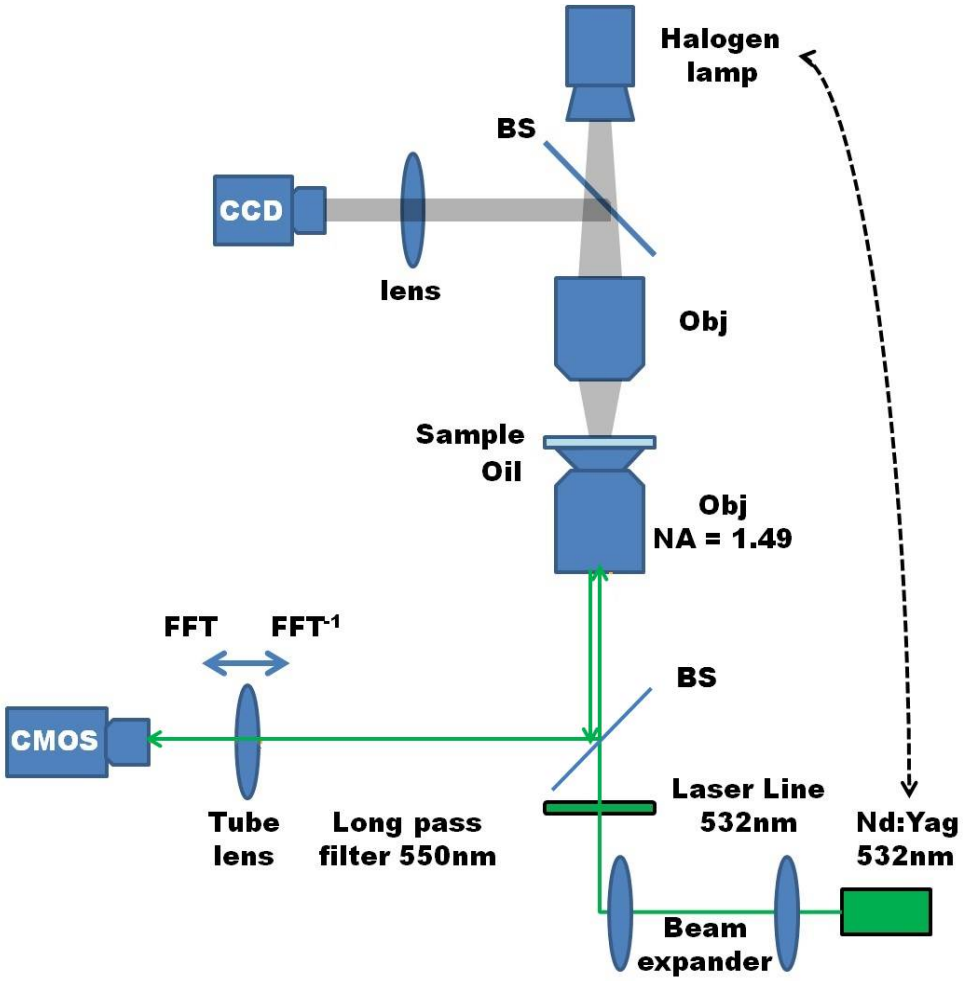

Figure 1.4: Schematic view of the customized Leakage Radiation Microscope emlpoyed in the experiments.

Here, we make use of a customized Leakage Radiation Microscope (LRM) setup (fig. 1.4) employing an oil immersion objective (Nikon APO TIRF 100x) with high Numerical Aperture ($NA = 1.49$). The working distance of the high NA objective is of the order of few hun-

dreds of μm, and this is a constrain as concerns the maximum thickness of the substrate (in our case we used $150\mu m$ thick glass coverslips). The microscope is capable of imaging both the direct plane and the back focal plane (BFP), i.e. the fourier transform of the direct plane. In this way, it is possible to obtain both the spatial and the angular distribution of the optical fields collected with the oil immersion objective.[31] The radiation collected is imaged via a tube lens onto a RGB CMOS camera (Thorlabs DCC1645C). The microscope is capable of collecting/illuminating also from the air side and the sample can be moved freely from the objectives by means of a piezo drive along the three Cartesian directions ($100\mu m$ x $100\mu m$ x $20\mu m$). Depending on the experimental requirements, different configurations of the microscope have been used in the following. Whenever required, a brief description of the setup employed and a small sketch of the experimental conditions will be provided.

In order to experimentally test our multilayer and observe the coupling of far-field radiation with BSWs, we illuminated the sample through the high NA objective oil contacted with the glass substrate with a quasi-collimated white halogen lamp. The white light is spectrally filtered by a laser line filter (MaxLine filter 532, Semrock) transmitting light in the spectral range $\lambda = 532 \pm 1nm$. The use of incoherent light improves the image quality, avoiding the problems of speckles.

The image in figure 1.5a indicates the intensity of light reflected under a reflection angle θ such that $n_{obj} sin\theta = \sqrt{n_{obj}^2 sin^2(\theta_x) + n_{obj}^2 sin^2(\theta_y)}$ where x and y indicate the leakage directions along the $x-$ and $y-$axis, respectively, and n_{obj} is the refractive index of the collecting objective. The leakage directions are related to the corresponding wavevector components as $k_x = k_0 n_{obj} sin(\theta_x)$ and $k_y = k_0 n_{obj} sin(\theta_y)$, respectively, where $k_0 = 2\pi/\lambda$ is the modulus of the wavevector in vacuum. The outer circle has a diameter proportional to the NA of the collecting objective. The obtained BFP image shows a sharp increase of the reflected light when the total internal reflection (TIR) condition is achieved, i.e. on a circle with radius $\sqrt{(k_x/k_0)^2 + (k_y/k_0)^2} = n_{obj}\sqrt{sin^2\theta_x + sin^2\theta_y)} = 1$ (light cone in air). For leaking directions comprised within the light line in air, the 1DPC is transmissive and light is partially reflected according to the band structure of the multilayer. In the TIR regime, the reflected light is imaged

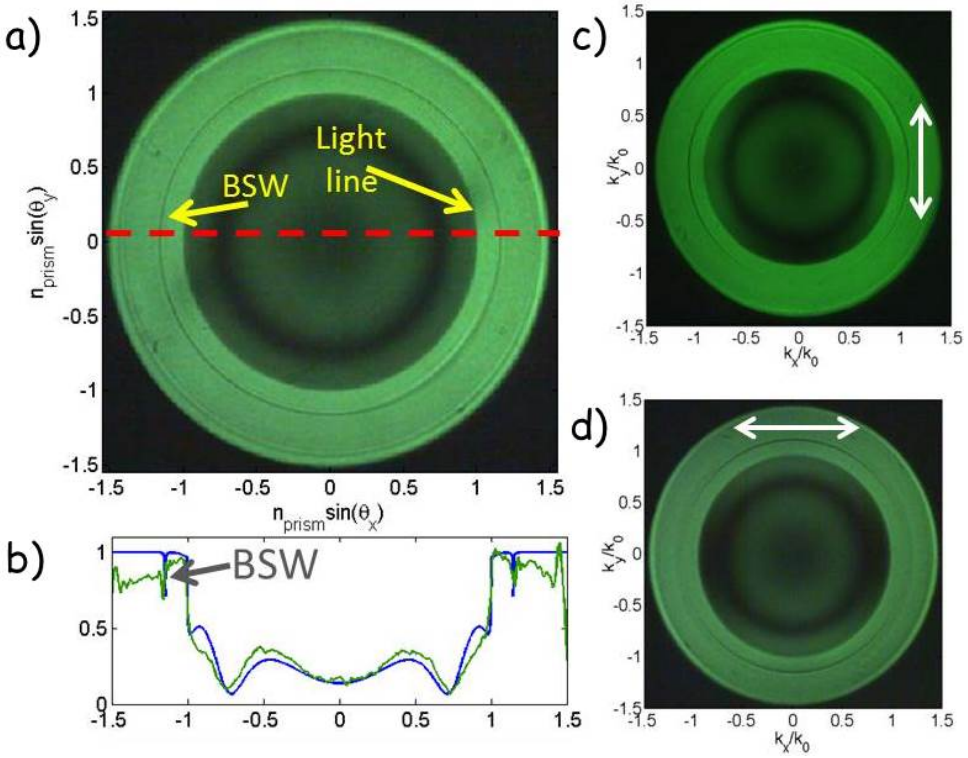

Figure 1.5: (a) BFP image of the NA = 1 . 49 objective illuminating a flat 1DPC with incoherent, unpolarized light (filtered at $\lambda = 532 \pm 1nm$); (b) cross-sectional intensity profile along the red dashed line depicted in (a) (solid green line) and calculated reflectivity profile for an s-polarized plane wave at $\lambda = 532nm$ (solid blue line). (c) and (d) Same as (a) when a polarization analyzer is placed along the collection path.

in an annular region limited by an inner radius defined by the light line and an outer radius defined by the objective NA. In such an annular region, the light is distributed homogeneously. At a radius $\sqrt{(k_x/k_0)^2 + (k_y/k_0)^2)} = 1.15$, a narrow low-reflectivity dip is found. By comparing the cross-sectional distribution of the BFP intensity along the horizontal dashed line in figure 1.5 a with a corresponding angular reflectivity calculated at $\lambda = 532nm$ with the TMM method, it is possible to account for the observed dips to the coupling of BSWs (figure 1.5b). The shallow depth of the dip can be explained by recalling that the incident light is unpolarized, while in this case BSWs are allowed in TE-polarization only. This assumption is confirmed in figures 1.5c,d. When a polarization filter is added on the illumination path, the dark circle turns into two half moons, and only radiation whose electric field is tangential to the dark ring couples to BSW,

while radially polarized light is reflected.

1.3 Surface couplers: linear gratings

Because of their evanescent nature, no direct coupling between BSWs and propagating photons in the outer medium (air in the present case) can occurr. However, a grating can provide additional momentum for incident light to couple to BSWs through, for example, first-order diffraction.[32] In the past, it has been shown that a sub-wavelength grating can back-reflect BSWs, thus producing an energy bandgap.[33] In the present case, a linear grating with spatial period $\Lambda_g = 520nm$ is fabricated onto the 1DPC (fig. 1.6a). The grating has been fabricated by directly patterning the surface of 1DPC with a Focused Ion Beam (FIB).

In order to couple incident radiation to BSWs, the grating period should be tailored according to the in-plane Bragg's law:

$$k_{diff} = k_{inc} \pm G \tag{1.2}$$

where k_{diff} is the momentum of the diffracted beam, $k_{inc} = k_0 sin(\theta_{inc})$ is the component parallel to the surface of the momentum of the incident beam and $G = 2\pi/\Lambda_g$ is the grating momentum. When k_{diff} equals k_{BSW}, given by the BSW disperison relation, coupling can occurr. For the multilayer employed here the dispersion relation shows that the coupling angle for $\lambda = 532nm$ is 49.5 deg. By applying 1.1, results that the effective wavelength of BSW is $\lambda_{BSW} = 2\pi/k_{BSW} = 466nm$. The mismatch between the effective wavelength of radiation coupled to BSW and the grating period can be compensated by using an objective with a NA high enough to ensure that the incident light has a wide spread of k-vectors including the ones that satisfy 1.2. In the present case, the incident angle required to couple radiation impinging on the grating from air is $\theta_{inc} = arcsin((k_{BSW} - G)/k_0) = 6.7$ deg, corresponding to a $NA \simeq 0.11$.

The inner bright (saturated) circle in figure 1.6b corresponds to transmitted light as focused by the NA = 0.95 objective. The $\pm$ 1 diffraction order of the grating can provide momentum matching to BSWs as demonstrated by the two bright arcs lying beyond the light line. In figure 1.6c the position of the two bright arcs along the dashed

red line in the figure corresponds approximately to the BSW reflectivity dips observed on the flat 1DPC (see figure 1.5b). The slight shift of the BSW resonance toward smaller leakage angles is produced by the decrease of the effective refractive index of the top 1DPC layer because of the corrugation.[32] The same effect can be observed by direct imaging the surface of the 1DPC. Since radiation coupled to BSW cannot be collected from the air side, a simple strategy to visualize

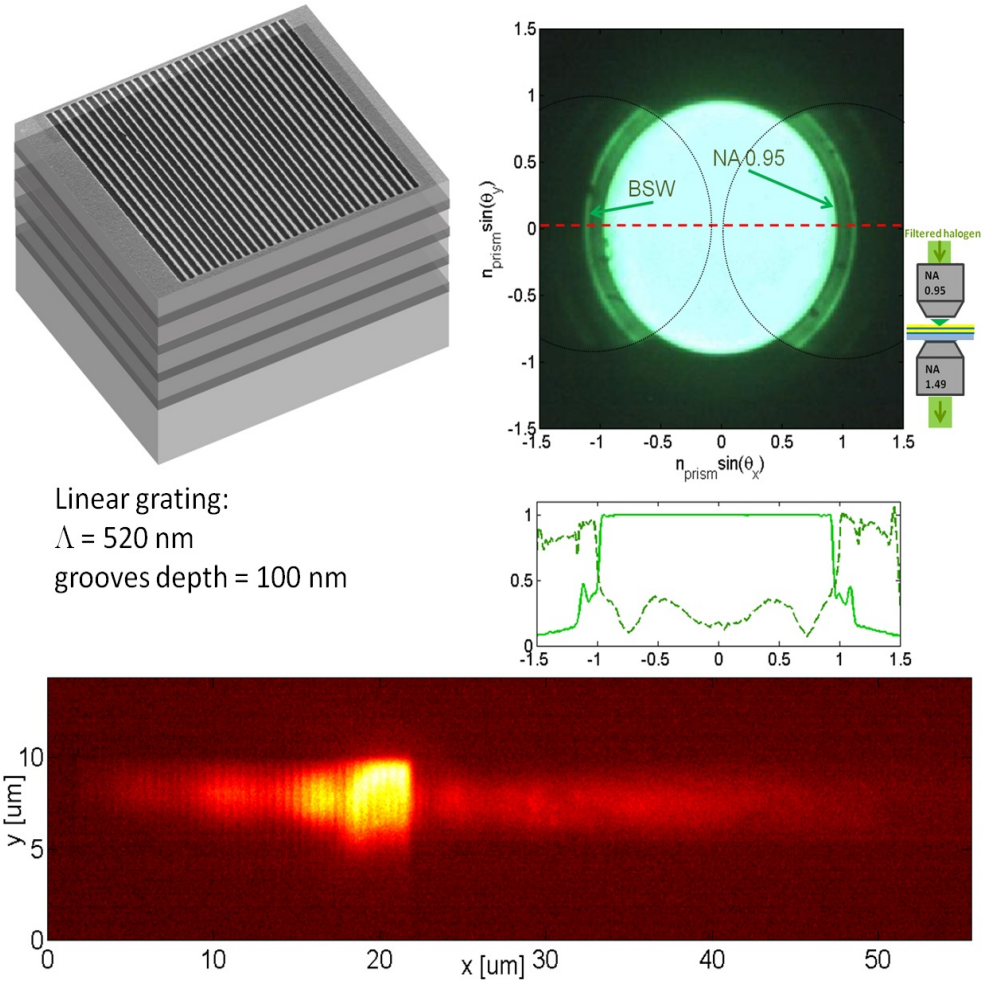

Figure 1.6: (a) Sketch of the one-dimensional photonic crystal with a linear grating patterned on the surface. The top image of the grating is a SEM image of the grating. (b) LRM image of the BFP when the grating is enlighted from the air side with a NA = 0.95 objective. The light comes from an halogen lamp and is filtered with a Laser Line Filter ($\lambda = 532nm$). (c) Intensity profile extracted from (b) along the red dashed line (green solid line). For comparison, also the intensity profile extracted form 1.5a (green dashed line) is reported. (d) Wide field fluorescence image of the BSW launched by the grating on the flat surface.

the near field distribution of light is to use fluorescent probes that, excited by the near field radiation, re-emit light in free space. The image in figure 1.6d is obtained by focusing a laser spot ($\lambda = 532nm$) on a portion of a linear grating. The surface of the 1DPC is covered with an homogeneous layer of a fluorescent dye (Rhodamine B). The fluorescent trace of the BSW, imaged on a CMOS camera, allows to easily visualize the near field distribution of light on the surface of the 1DPC.

1.3.1 Coupling of coherent light: Leakage Radiation Interference Microscopy

By employing a more complicated setup, it is possible to achieve a more complete description of the BSW-coupled radiation. If the leakage radiation microscope described above is integrated with an interferometric setup, information about the phase and amplitude distribution of light coupled to the surface modes can be retrieved in addition to the intensity distribution.[34]

An implementation of the leakage radiation interference microscope (LRIM) is schematically shown in figure 1.7. A detailed description of the working principle of the interferometric technique employed for the amplitude and phase retrieval can be found in.[35] Here, a collimated beam from a frequency doubled Nd:YAG laser source at $\lambda = 532nm$ is splitted into two arms of a Mach-Zehnder interferometer by means of a polarizing beam splitter (PBS). The polarization of the light beams is controlled through a pair of half wavelength plates and Glann-Taylor polarizers. The so-called object beam is sent to an objective (NA = 0.5) used for sample illumination. The effective NA of the illumination objective can be reduced as desired by means of a diaphragm placed in front of the objective entrance pupil. The light emerging from the sample is collected by means of an oil immersion objective (NA = 1.4) and imaged through a tube lens on a charge-coupled device(CCD), where it is superposed with the reference beam. The reference beam undergoes a set of five controlled phase shifts produced by means of a piezo-actuated mirror. An offline image-processing algorithm based on the Schwider-Hariharan method[36,37] takes into account the five interference images recorded by the CCD and retrieves amplitude and phase distributions related to the collected field. The

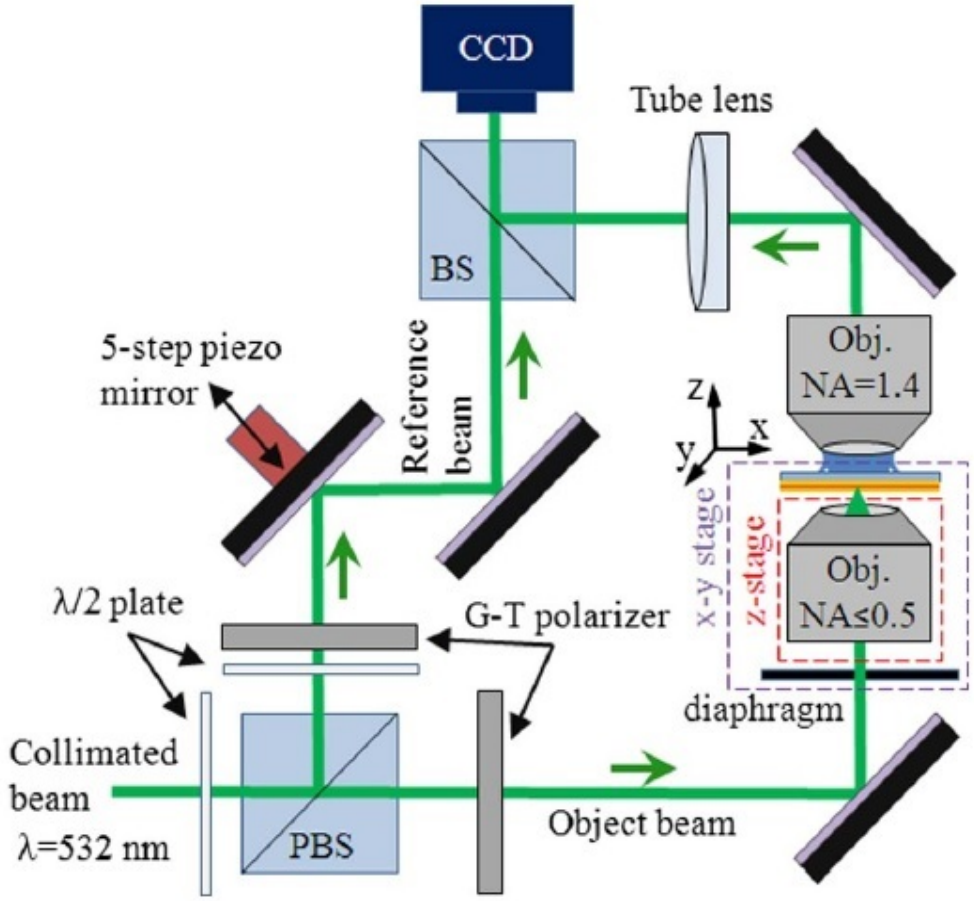

Figure 1.7: Schematic view of the leakage radiation interference microscope, also escribed in.[34]

experimental mounting is such that the illumination objective can be moved longitudinally (along the z axis) with respect to the sample plane.

Furthermore, the assembly of the illumination objective together with the sample holder stage can be laterally moved (along the x and y axes) with respect to the collection objective, as schematically depicted in figure 1.8a.

When a Bertrand lens is inserted in the collection optical path before the tube lens, a back focal plane (BFP) image proportional to the Fourier transformation of the direct plane image[38] is produced on the CCD camera. This arrangement is particularly useful for collecting light belonging to the BSW leakage radiation as separated from the direct illumination and eventually the scattered light contributions. In figure 1.8b the BFP image of the collection oil immersion objective is presented. The external (green) circle defines the maximum NA of

the objective (NA = 1.4), while the inner (blue) circle defines the light line in air (corresponding to NA = 1). The direct incident illumination is visible as a circle with radius NA = 0.15, corresponding to the particular illumination configuration used in this case. When the object beam polarization is set as linearly polarized along the x axis and the grating is brought under the illumination spot with its grating vector

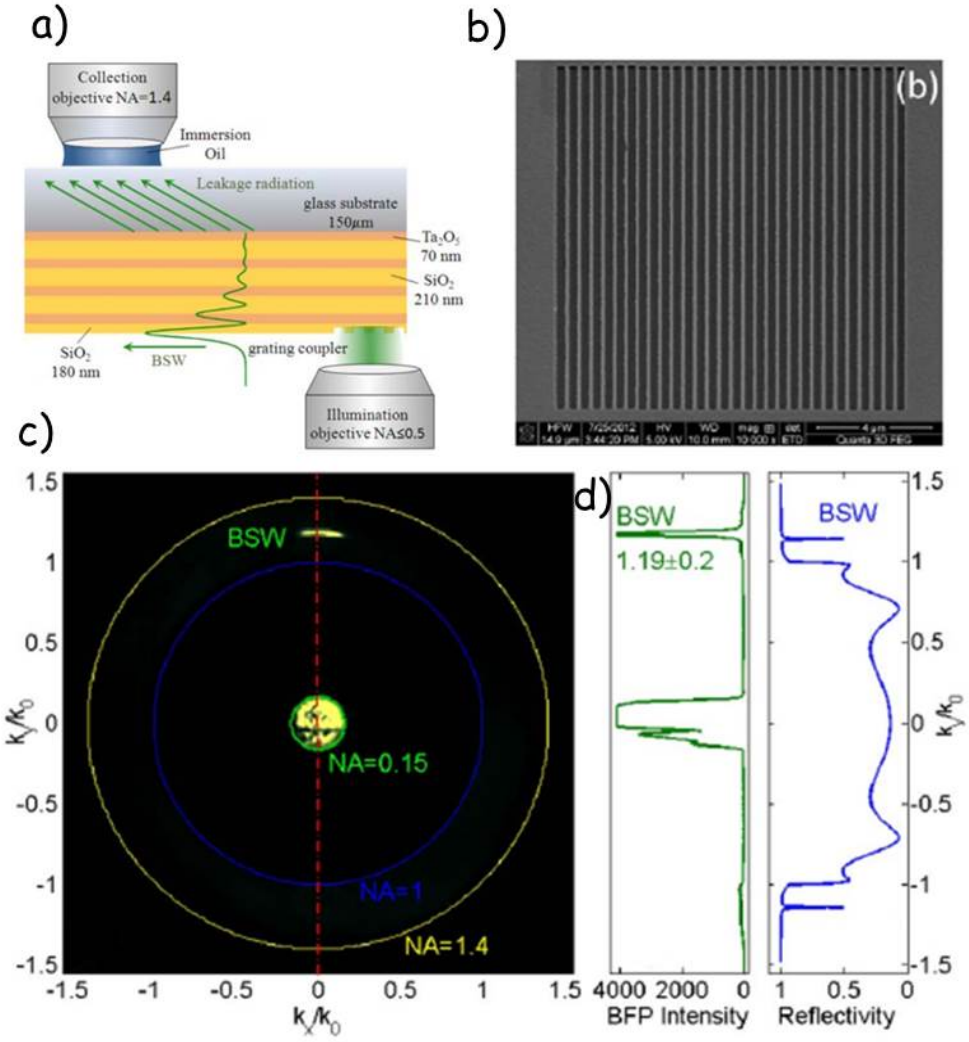

Figure 1.8: (a) Detailed sketch of the photonic structure and the experimental arrangement used for sample illumination and leakage radiation collection. (b) Scanning electron microscope image of the grating coupler for a Bloch surface wave (BSW). (c) BFP image of grating coupled BSW upon illumination with a NA = 0.15 beam. (d) Experimental (green) cross-sectional intensity profile of BFP along the dashed red line in (a) and calculated (blue) angularly resolved TE-polarized reflectance at $\lambda = 532nm$ revealing BSW resonances as indicated.

parallel to the y axis, a bright arc appears beyond the air light line, at a location $k_y/k_0 = 1.19 \pm 0.2$. This is highlighted in figure 1.8c, where the BFP intensity cross section along the red dotted line in figure 1.8b is plotted. The bright arc is polarized along the x direction, and it is associated to a BSW coupled by the grating. As a check, the calculated TE-polarized angular reflectance profile at $\lambda = 532nm$ presented in figure 1.8d reveals the presence of BSW resonance dips at $k_y/k_0 = 1.15$, as previously shown in figure 1.3 on the ideal multilayer layout from design.

By removing the Bertrand lens from the collection path, a direct image of the surface is produced on the CCD camera (fig. 1.9a). The image of the BSW launched by the grating is obtained by collecting the leakage radiation through the oil immersion objective. In order to reduce the directly transmitted light, that in the direct plane image cannot be separated from the lekage radiation, the collection objective is placed almost completely out of the field of view of the illumination objective. Since the 1DPC surface has a very low roughness, we could limit interference effects due to scattering. In these conditions, we performed a full amplitude/phase measurement through the five-step interferometric technique as described above. An exemplary result is presented in figure 1.9. Specifically, figure 1.9a shows an amplitude distribution of the TE-polarized electric field associated to a BSW launched through direct illumination (NA = 0.25) of the grating, positioned at the top border of the image (saturated CCD pixels). The BSW propagates according to the green arrow.

The presence of high-frequency fringes can barely be appreciated on the amplitude distribution, because of the above-mentioned effects. Figure 1.9b exhibits a corresponding BSW phase distribution, wherein the BSW propagation is revealed by a periodic sawtooth phase profile, as reported elsewhere.[23] By combining the amplitude and phase mappings, a complex electromagnetic field distribution can be obtained, whose real part is illustrated in figure 1.9c. If a fast Fourier transformation (FFT) is performed on the complex field recovered along the propagation direction, the spatial Fourier spectrum illustrated in figure 1.9d is obtained. The spatial spectrum is characterized by two peaks symmetrically centered at spatial frequencies $f_y^{BSW} = (2.25 \pm 0.3)\mu m^{-1}$. The peak with positive frequency and higher amplitude is associated to a BSW propagating in the positive

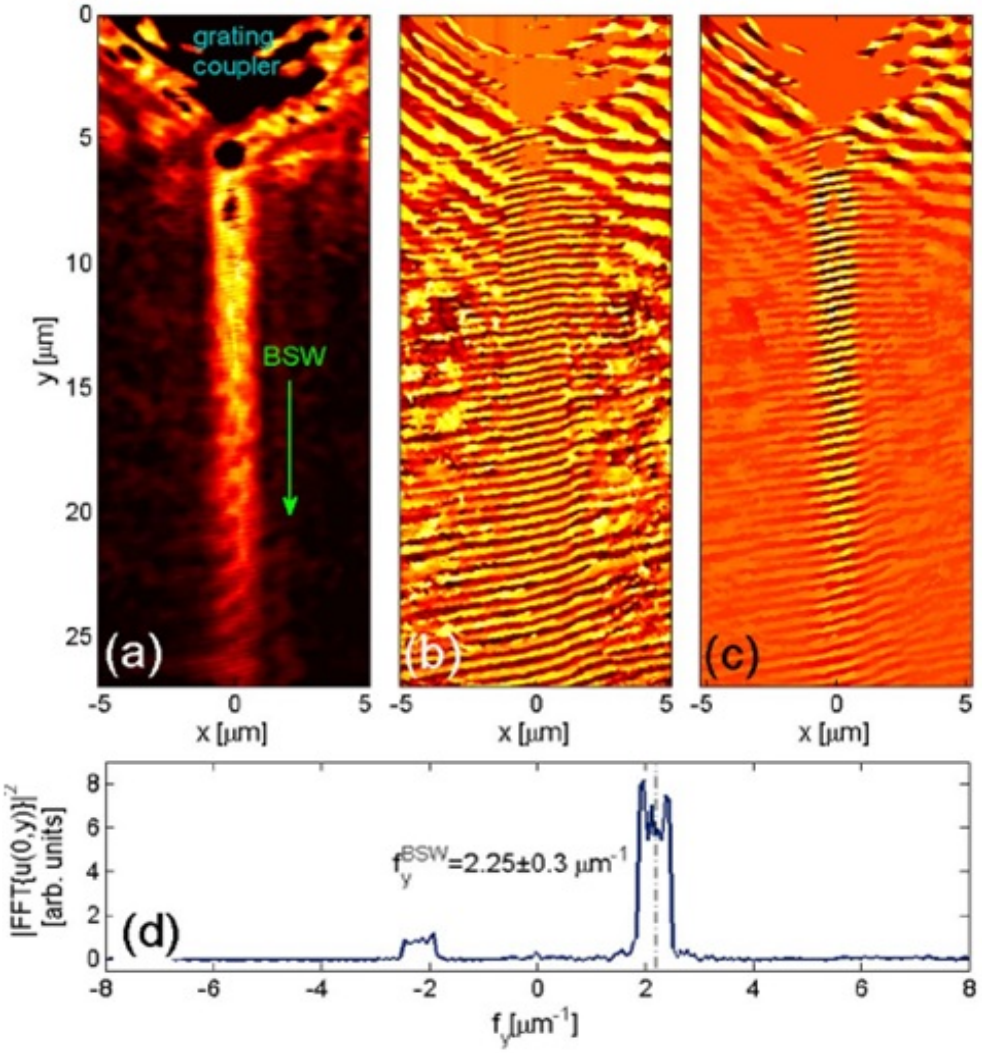

Figure 1.9: (a) Direct plane image of BSW launched from a grating coupler. (b) Corresponding BSW phase distribution retrieved. (c) Real part of the obtained BSW complex field. (d) $\mid FFT \mid^2$ profile of the measured complex field along the propagation direction of BSW.

y direction, while the peak exhibiting a smaller amplitude is associated to a BSW propagating in the negative y direction, collected essentially from the grating region.

The two detected peaks correspond to a spatial modulation of the complex field matching the BSW effective wavelength, as given by $\lambda_{eff}^{BSW} = \mid 1/(f_y^{BSW}) \mid = 444.4 \pm 59.3nm$. This value should be compared with the effective BSW wavelength from the BFP image analysis in fig. 1.8 as $\lambda_{eff}^{BSW} = 442.2 \pm 7.5nm$, revealing a good matching between the two measurements, and to the theoretical value calculated by means of the TMM method (fig. 1.3) that is $\lambda_{eff}^{BSW} = \lambda_0/n_{eff} = 465nm$.

The larger uncertainty in the BSW effective wavelength as estimated from the direct-plane complex field FFT can be explained by a smaller spatial domain wherein the field can be properly detected.

In order to overcome the planar anisotropy of diffraction produced by a linear grating, a circular corrugation can be considered. With an incoherent light illumination (white light from an halogen lamp filtered with a Laser Line Semrock 532 nm) focused through the upper objective (NA = 0.95), the circular grating couples the incident radiation to BSWs isotropically in the $xy-$plane (figure 1.10), provided

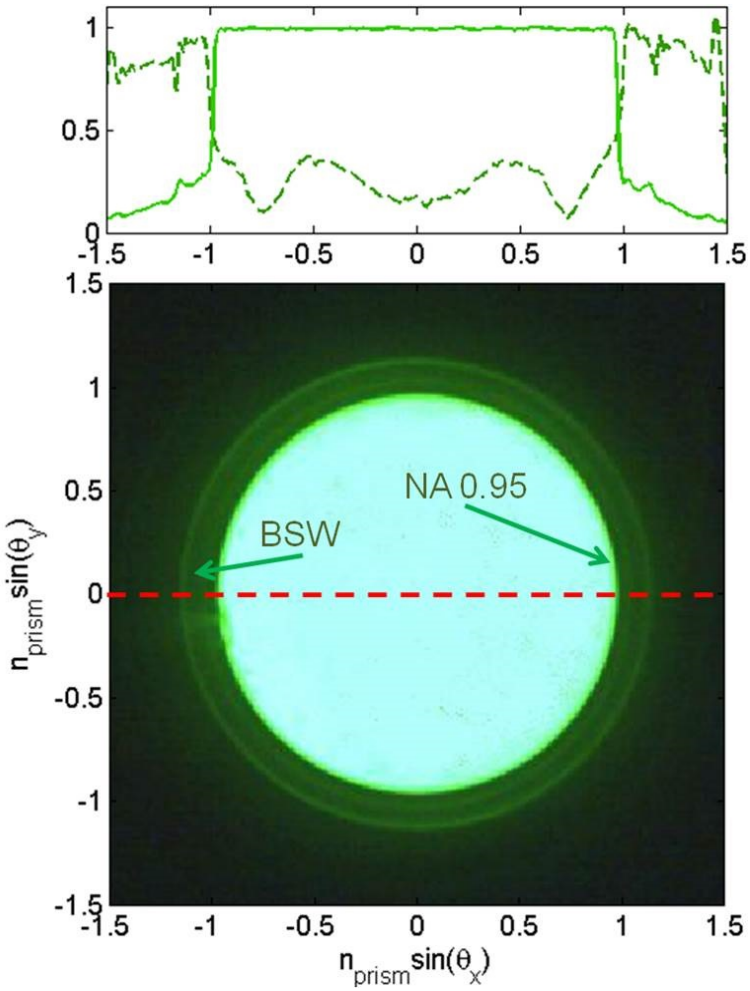

Figure 1.10: BFP image of the $NA = 1.49$ objective collecting light from a circular grating on a 1DPC illuminated with unpolarized, incoherent light (filtered at $\lambda = 532nm$) by means of a top objective $NA = 0.95$. In the inset above, a cross-sectional intensity profile along the red dashed line depicted in the figure below (solid light green line) and measured reflectivity profile from figure 1.5b (dashed dark green line). Grating-coupled BSWs are observed as narrow peaks outside the cone of direct illumination.

that the spot light is large enough to lighten the whole grating. As for the linear grating, the intensity profile along a horizontal cross section (dashed red line in figure 1.10) reveals two BSW leakage peaks corresponding to the BSW reflectivity dips observed on the flat 1DPC in figure 1.5b. Also in this case, the grating provides enough additional momentum to free-space photons propagating in air to couple to surface modes, while the radial symmetry of the structure ensures that coupling occurs for each in-plane direction.

Chapter 2

In-plane manipulation of Bloch Surface Waves

BSWs can be considered as an effective alternative to Surface Plasmon Polaritons(SPPs) as information carriers in applications that can take advantage from an enhanced density of photonic states at the interface between the substrate and the external environment, such as sensing on planar supports or surface photonic circuitry. The inherent advantages of BSWs over SPPs described in the previous chapter, make them a suitable candidate in such applications.

In the last decades, many research groups put in a lot of efforts into the manipulation of SPP, by employing refractive or diffractive surface structures.[39,40] Similarly to SPPs on flat and structured metallic films, BSWs can be manipulated by means of refractive or diffractive structures exploiting the BSW effective index shift due to the dielectric-loading effect. For example, BSW can be laterally confined and guided,[23] reflected,[33] refracted,[41] in-plane diffracted and out-coupled from the multilayer surface.[32,42,43]

In this chapter, I will show how BSWs can be focused and eventually guided in order to locally enhance the electromagnetic field on the surface of a 1DPC by means of two main strategies. In the first paragraph, thin polymeric elements will be employed as surface refractive elements to focus and guide BSWs, while in the second chapter a circular corrugation will be used to couple far field radiation to BSWs that, following the symmetry of the structure, will converge toward a localized area, thus increasing the field in a localized area.

2.1 BSW focusing by ultrathin refractive structures

2.1.1 Dielectric loading effect

It is well known that SPPs are strongly affected by refractive index changes in close proximity to the surface. Such effect has been extensively studied and it is now implemented in commercial sensing devices.. The basic principle of Surface Plasmon Resonance (SPR) based sensors is that a variation of the refractive index in the external dielectric medium (e.g. air or water) results in a variation of the effective index of the mode, i.e. a shift of the SPP dispersion relation.[44] The same effect has been observed when BSWs are considered. Many sensing schemes based on the dielectric loading effect have been proposed in the last years, both to monitor the refractive index of the environment[45] and to monitor binding events occurring at the surface of a 1DPC.[46]

Here I want to show that the resonance shift can be exploited to fabricate 2D refractive elements that would allow for in-plane manipulation of BSWs. In fig. 2.1a a schematic view of the refractive polymeric structures fabricated on the surface of a 1DPC, namely a bidimensional biconvex lens and a ridge waveguide, are presented. In fig. 2.1b, the TE reflectance map shows the BSW dispersion relation when a bare multilayer is considered. In this case the multilayer design is the same described in chapter 1. When a thin layer of additional material is deposited on the multilayer surface, a red shift of the BSW resonance is produced, leading to an increase of the effective index of the surface mode at fixed wavelength.[47] In figure 2.1b the BSW dispersion corresponding to the 1DPC coated with a 30-nm-thick polystyrene (PPST, n = 1.55) layer is also presented as a dashed black line. At $\lambda = 532nm$, BSWs on bare and coated multilayer have a calculated effective index equal to 1.14 and 1.19, respectively (see inset).

Surface relief polymeric structures have been fabricated on the multilayer by laser lithography followed by PPST deposition (30 nm) and subsequent lift-off in acetone. The experimental setup employed in the following experiments is shown in figure 2.2. The back side of the glass substrate hosting the multilayer is oil contacted to a glass

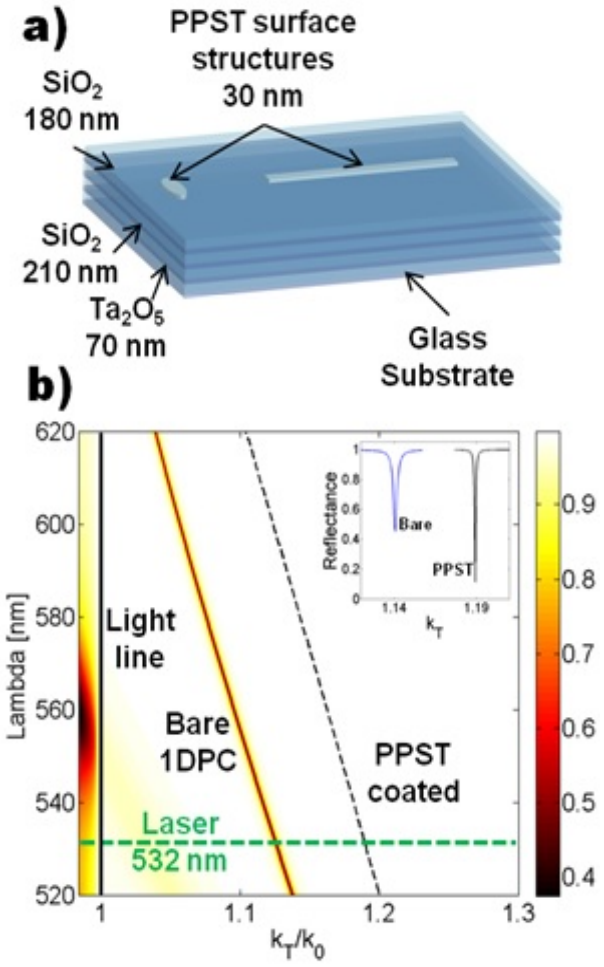

Figure 2.1: (a) 3D sketch of the polymeric refractive structures fabricated on top of the 1DPC. (b) Calculated TE reflectance map function of lambda and the effective index of the mode k_T/k_0. To evaluate the dielectric loading effect, the position of the dip in reflectance for the multilayer coated with 30 nm of PPST is reported (black dashed line). An intensity profile extracted along the green dashed line (at $\lambda = 532nm$) is reported in the inset.

prism, according to the Kretschmann configuration. A doubled frequency Nd:YAG CW laser beam impinges on the 1DPC through the prism. The lateral size and the divergence of the beam can be adjusted by means of a beam expander system and a diaphragm. The angle of incidence θ_{BSW} is such that the transverse wavevector k_T of BSW at $\lambda = 532nm$ can be matched through the relationship $k_T = n_{prism} \sin(\theta_{BSW})$, where n_{prism} is the glass-prism refractive index.

In order to observe the intensity distribution of BSW on the surface of the 1DPC, one can directly collect the evanescent field by means of a near-field probe.[25] Although this method can provide both amplitude

and phase distribution of the field on the surface, it is time consuming and requires a dedicated apparatus. As a feasible alternative, it is possible to make the multilayer surface fluorescent upon excitation at BSW wavelengths. In this case, a fluorescence trace of the underlying excitation field can be obtained, thus revealing the BSW spatial distribution.

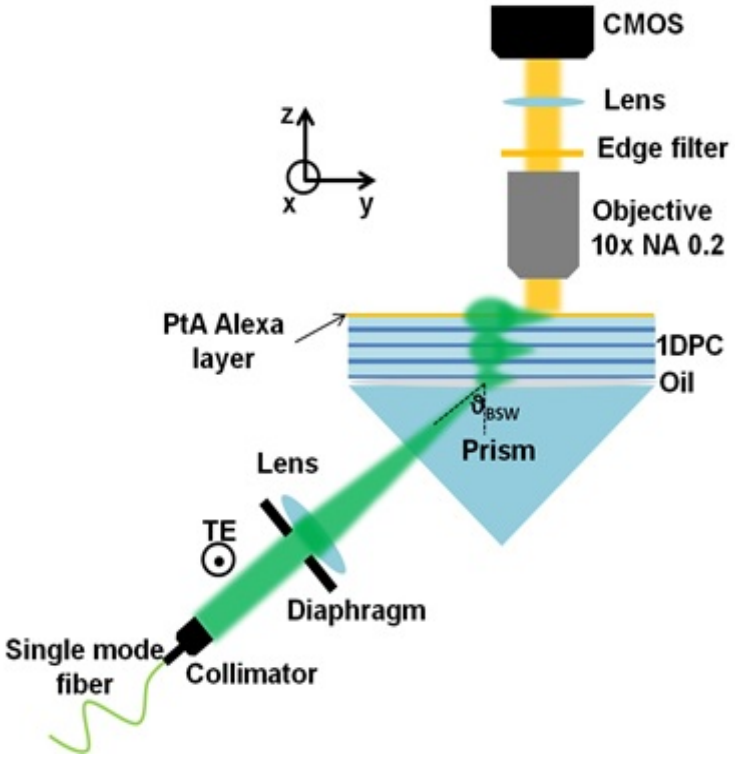

Figure 2.2: Sketch of the experimental setup employed to observe the fluorescent trace of BSW coupled through a prism oil contacted in the Kretschmann configuration. Illumination is provided by a quasi-collimated laser beam.

Here, we incubated protein A conjugated with Alexa Fluor 546 (PtA-Alexa 456) on the multilayer surface for 20 min. and then rinsed with phosphate buffered saline (PBS) buffer, so that an homogeneous and stable fluorescent layer is obtained. The dielectric loading effect played by such a monolayer is negligible here, since the slightly red-shifted BSW resonance still falls within the angular divergence of the weakly focused incident laser beam. In this way, fluorophores act as a probe for the BSW near-field intensity, thus allowing a simple fluorescence imaging from the air side with a CMOS camera. One drawback of this approach is represented by the absorption. introduced by the presence of the fluorophores on the surface that affects the decay length

of BSW, as explained in detail in the following section.

2.1.2 Evaluation of BSW decay length

In order to evaluate the focusing effect and to have a realistic comparison between experimental data and modeling, an evaluation of the decay length is required. Starting from the TMM calculations, a theoretical estimation of the decay length can be obtained by extracting the Full Width Half Maximum (FWHM) of the dip in reflectance, according to the following relation:[48]

$$L_D = \lambda_{BSW}/(\pi\sigma) \tag{2.1}$$

where λ_{BSW} is the effective wavelength, while σ is the FWHM of the resonance. In this case, the width of the resonance is determined by two contributions: the intrinsic losses of the materials employed and the leakage radiation.

The first one depends on the quality of the dielectric layers and on the defects of the surface producing scattered light. An ellipsometric analysis of the dielectric thin films revealed no detectable absorption. Since in TMM calculations an absorption coefficient is required to observe the dip, we set the imaginary part of the refractive indices at a value of $2{\cdot}10^{-4}$, which is basically the lower limit of detection in most of the ellipsometric techniques. Moreover, in previous papers where the role of absorption has been discussed, such value as ben successfully used to reproduce experimental results in analogous 1DPCs.[49]

The effect of leakage radiation is mostly related to the 1DPC design. The amount of radiation that tunnels through the multilayer depends on the reflectivity of the bragg structure for the specific energy-momentum pair given by the BSW dispersion relation. When the elementary cell (i.e. the high-low refractive index layers pair) of the multilayer is fixed, the reflectivity only depends on the numbers of pairs. Increasing the number of pairs frustrates the tunneling of radiation from the BSW to the substrate, reducing the overall losses of the mode and therefore narrowing the resonance (fig. 2.3).

The slight red-shift observed when the number of layers is increased can be explained by considering the field distribution of the mode: when the number of layers increases, the percentage of the energy confined inside the multilayer increases with respect to the percentage

of energy distributed in the external evanescent tale, thus increasing the effective refractive index of the mode. It has to be noticed that a narrower resonance, corresponding to a higher Q-factor, means that the photonic mode is, in some sense, more isolated with respect to the external environment, and it is therefore more difficult to couple far field radiation to the mode itself for example by employing a prism coupled configuration or an oil immersion objective setup. This point will be further discussed in Chapter 3.

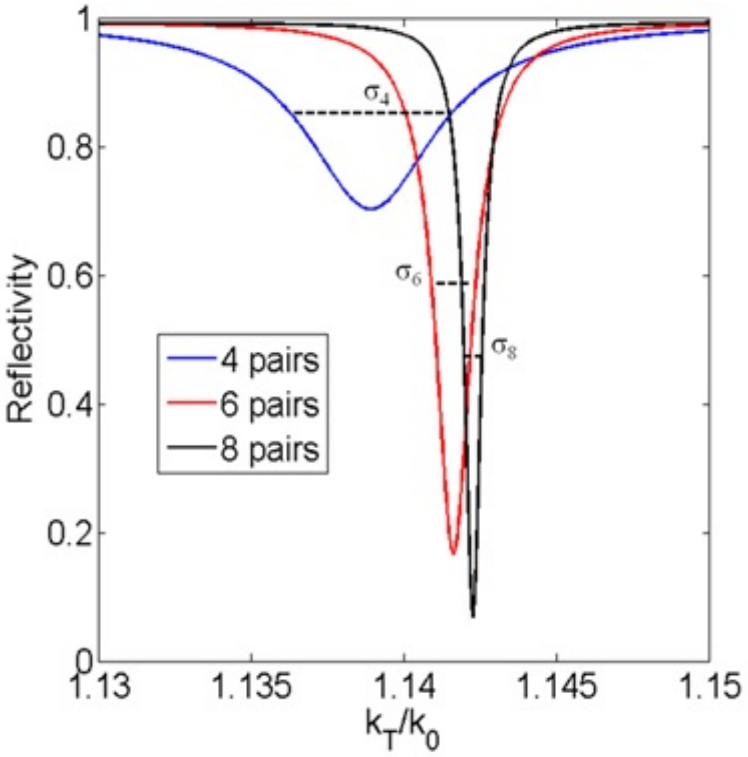

Figure 2.3: Reflectance calculated at $\lambda = 532nm$ for different multilayers with the same elementary cell but different number of layers.

By applying equation 2.1, the theoretical decay length on the bare multilayer employed in the experiment (4 pairs) is $34\mu m$. In order to obtain an experimental estimation of the decay length, we launched a BSW on the flat surface (inset in fig. 2.4) and measured the fluorescence intensity. In figure 2.4, the experimental data (blue line) were fitted with the following relation:

$$I(y) = I_0 e^{(-y/L_D)} \tag{2.2}$$

where I_0 is the measured initial fluorescence intensity and L_D is the fitting parameter corresponding to the BSW decay length. The best fit

(red dashed line) has been obtained for $L_D \approx 28\mu m$. The difference between the experimental data and the theoretical value has been attributed to the fluorescent layer: the fluorophores act as absorbers for laser radiation and, in addition, agglomerates of rhodamine are scatterers on the surface, thus increasing the overall losses.[50]

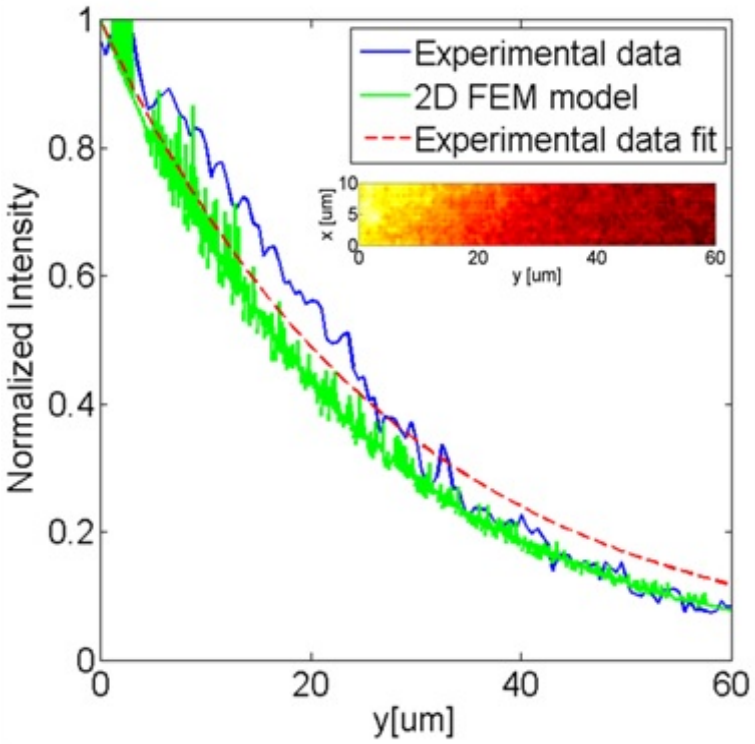

Figure 2.4: Measured (blue) and calculated (green) normalized intensity profile of fluorescence excited by the BSW coupled at $y = 0$. The red dashed line has been obtained by fitting the experimental data with equation 2.2. In the inset, the fluorescent trace of the BSW as imaged on the CMOS camera reported in false colors.

.

In order to obtain a realistic comparison with a 2D FEM model, such decay length has to be reproduced in an effective medium model.[25] The 2D medium mimicking the surface of the 1DPC is therefore modeled with a refractive index in which the real part corresponds to the effective index of the BSW mode, as derived from the TMM calculations, while the imaginary part has been set according to the following relation:

$$k = \lambda_{eff}/(4\pi L_D) = 1.8 \cdot 10^{-3}. \tag{2.3}$$

It has to be pointed out that such absorption coefficient is not

related to the absorption of the materials, but it is just a fictitious parameter allowing a direct comparison between the propagation of BSW on the surface of a structured medium such as the 1DPC and an effective homogeneus medium. The green line in fig. 2.4 corresponds to the intensity of a plane wave ($\lambda = \lambda_{eff}$) propagating into such an homogeneous layer. The good agreement between the model and the experiment confirms the validity of the above described approach.

2.1.3 Experimental results

The effective indices of BSW at $\lambda = 532nm$ calculated by the TMM method together with the absorption coefficients derived in the previous section have been used to model the BSW propagation and focusing in a 2D effective index model built on commercial software (COMSOL 4.2a RF module). The planar lens is a biconvex lens with a radius of curvature of $6\mu m$ and a diameter of $10.4\mu m$. The expected focal plane is located at about $35\mu m$ from the lens. From the 2D effective index model, the BSW is focused according to an intensity distribution as illustrated in figure 2.5a. Experimentally, the BSW focusing effect produced by the 30-nm-thick polymeric lens is observed as shown in figure 2.5b. This fluorescence image is rendered in false colors to help a direct comparison with calculations in fig. 2.5a. The dominant role of losses is such that the intensity enhancement due to BSW focusing cannot be appreciated.

In order to appreciate the good agreement between experiment and calculation, the cross-sectional intensity distribution in the focal region (about $35\mu m$ far from the center of the lens) are considered. The calculated FWHM of the intensity distribution on the focal plane is about $2\mu m$. For comparison purposes, the limited spatial resolution of the collection optics needs to be taken into account. To this aim, we convolved the calculated profile with a Gaussian function (roughly mimicking the point spread function (PSF) of the collection objective) whose variance is given by the Rayleigh resolution limit:

$$\sigma^2 = \lambda/(2NA) \approx 1.43\mu m. \tag{2.4}$$

where $\lambda = 570nm$ is the peak fluorescence emission wavelength and NA = 0.2 is the numerical aperture of the collection objective. Af-

ter convolution we obtained a calculated field-intensity profile having a $FWHM = 4.3\mu m$, which is close to the corresponding measured profile having a $FWHM = 5 \pm 1\mu m$. The accuracy of this estimation is limited by the image pixelization of the CMOS camera. The as-measured and the convolved calculated profiles are in very good agreement, as shown in figure 2.5c. We finally observe that the thin lens on the multilayer surface appears rather dark in the fluorescence image because of the antifouling feature of PPST,[51] whereby fewer PtA-Alexa molecules can be grafted thereon.

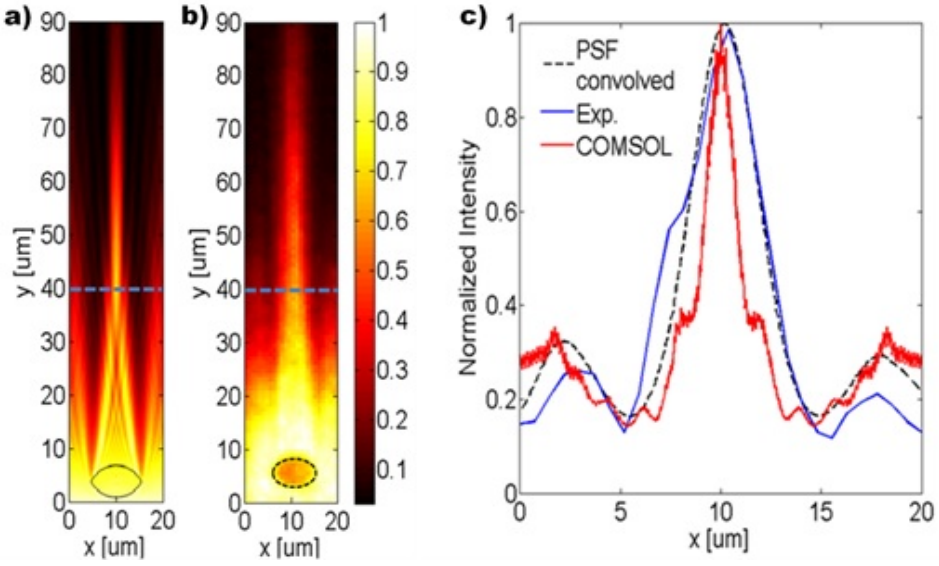

Figure 2.5: (a) Calculated BSW focusing by means of a 30-nm-thick lens having a radius of curvature of 6 μm and diameter 10.4 μm. (b) Fluorescence image of BSW as focused by the polymeric lens (marked with the black dashed line). The blue dashed lines indicate the focal plane. (c) Calculated (solid red line) and measured (solid blue line) transverse intensity profiles in the focal planes. The black dashed line is obtained by convolving the calculated profile with an approximate point spread function (PSF) associated with the collection optics.

Two-dimensional refractive elements can serve as waveguide couplers. We positioned a lens in front of a thin planar ridge whose terminal end is approximately within the focal plane of the lens. The lens is identical to the previous one. The rectangular PPST waveguide is $100\mu m$ long, $5\mu m$ wide, and 30 nm thick and is made of PPST, as is the lens. Computational results show that the BSW, focused by the lens, is actually injected into the ridge and propagates along the waveguide (fig. 2.6a). The experimental observation presented

in figure 2.6b confirms that an effective index variation produced by a 30 nm PPST layer is high enough to guide the BSW in a straight direction.

Similar to fig. 2.5b, the drastic reduction of fluorescence intensity observed on the waveguide is due to a lower concentration of ptA Alexa adsorbed on the PPST structure. If a longitudinal cross-sectional profile of intensity is considered (fig. 2.6c), the sharp changes in the ptA-Alexa concentration adsorbed on the surface can be appreciated at both terminal ends of the ridge, as indicated. Within the waveguide, the intensity distribution (integrated along the x axis in a region between 9 and 11 μm) has an exponentially decaying profile. In order to calculate the decay constant, we fit the experimental profile with eq. 2.2. Best fit, in this case, is obtained for $L_D = 83.3\mu m$, which is roughly four times larger than the propagation length observed outside the guide.

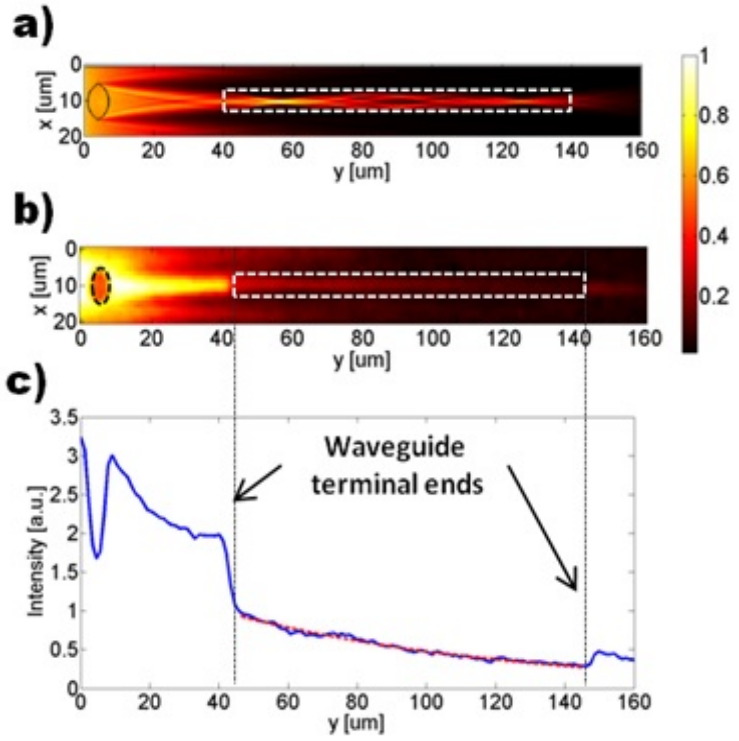

Figure 2.6: (a) Calculated and (b) measured intensity distribution of a BSW injected into a polymeric ridge waveguide (contour, dashed white line) by means of a 2D lens. (c) Experimental intensity profile along the y axis extracted from (b). The vertical dotted lines indicate the waveguide terminal ends. Inside the waveguide the profile is well fitted by an exponentially decaying function (dashed red line).

This value agrees well with the theoretical value of $83.7\mu m$ as expected on a uniform 30-nm-thick PPST layer. The resonance in presence of the PPST coating is indeed much narrower with respect to the resonance on the bare substrate (see inset in fig. 2.1a). In this case, the absorption due to fluorescent probes has minor impact due to antifouling properties of PPST. In the effective medium model, upon a proper scaling down of the absorption coefficient in the waveguide by a factor of four (leading to an absorption coefficient of $4.38 \cdot 10^{-4}$), we find a good matching between calculations and experiment (see fig. 2.6a and b).

2.2 In-plane focusing by concentric corrugations

As an alternative strategy to enhance the electromagnetic field in a localized area by exploiting BSW coupling, diffractive structures can be considered.[42] Differently from the refractive structures presented above, where the coupling of far field radiation and the focusing effect of the fabricated polymeric strctures where independent events, here it is the structure itself that allows for coupling the incoming radiation to the BSW, while the peculiar symmetry of the structure will provide the focusing effect.

In the first chapter I've shown how a linear grating with proper period designed according to the Bragg's law can be used to efficiently launch BSW. In this section I wil show that an annular grating can be used to enhance the electromagnetic field in the center of symmetry of the structure. The experimental setup employed to perform the following experiments is the one schematically shown in figure 1.7, with an additional feature: a beam blocker placed in the center of the BFP of the collection objective (fig. 2.7) blocks the directly transmitted light. By this way, the image formed in the CCD camera is mainly produced by the collected leakage radiation, allowing to image the spatial distribution of radiation coupled to BSW on the surface.

The sample structure is sketched in fig. 2.8. Very briefly, the surface of the 1DPC is patterned with an array of concentric rings surrounding an inner flat spacer. The circular grating is etched on the multilayer top layer in such a way that a ring pattern is arranged with

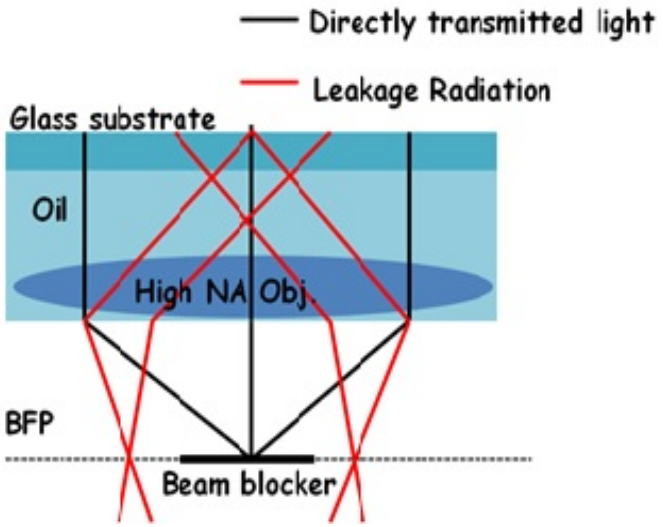

Figure 2.7: Working principle of the Fourier filtering employed to block the directly transmitted light and to have an image only formed by BSW leakage radiation.

a spatial period $\Lambda_g = 480nm$, and the total thickness of the grating is about 100 nm. The inner spacer diameter can be 5 μm or 8 μm. The grating vector is radially oriented with respect to the circular grating center, and has a module $G = 2\pi/\Lambda_G = 12.08\mu m^{-1}$, that is very close to the BSW wavevector in the wavelength range between 532 nm and 590 nm. When an external radiation of a specific wavelength λ is impinging on the circular grating from air, it undergoes diffraction according to the Bragg's law. The first-order (+1) diffracted radiation has a wavevector component k_T^{+1} parallel to the multilayer surface as given by $k_T^{+1} = k_T^0 + G$, where k_T^0 is the wavevector component of the incident radiation parallel to the multilayer surface. When k_T^{+1} matches the BSW wavevector, energy coupling between the incident radiation and the surface mode can occur. For an incidence radiation with wavelength $\lambda = 532nm$ (as used here), the BSW cannot be coupled at a perfectly normal incidence, but an incidence angle of about 2.3 degrees is required.

In the case of a circular grating as the one reported here, the grating has a curvature radius and an in-plane focusing effect can be expected for the grating-coupled BSW, in analogy to surface plasmons.[52,53] This effect has been observed on our structure by locally illuminating a portion of a circular grating and observing the leakage radiation associated to BSW as collected with the interference leakage

radiation microscope shown in fig. 1.7.

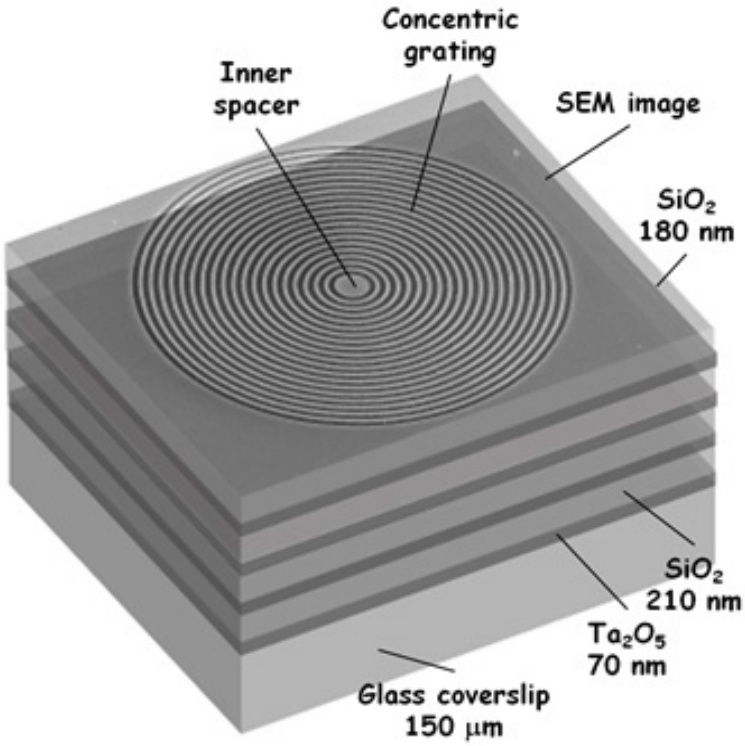

Figure 2.8: Sketch of the concentric ring diffractive structure employed to couple far-field radiation to BSW and localize it in the center of the ring array. The concentrig grating is patterned on the surface of the 1DPC by EBL. The top layer is a SEM image.

Starting from the illuminated area, a BSW is coupled and then focused in a central region of the inner spacer surrounded by the circular grating. A superposition of a white image of the structure with the intensity distribution of light, amplitude and phase maps of the focused BSW are shown in figure 2.9.

More interestingly, when the circular grating is homogeneously and fully illuminated with the laser beam, the coupling to BSW can occur according to the local spatial orientation of the grating. A circular BSW converging toward the center can be then produced. In order to provide momentum matching between BSW and the incident radiation through the grating, the angular spread of the laser beam can be slightly adjuste along the illumination path. Experimental amplitude and phase maps of focused BSW are presented in fig. 2.10a,b. If the laser is linearly polarized, BSW can be coupled only from locations of the rings wherein a polarization matching condition is satisfied.

Specifically, the TE-polarization of BSW allow efficient coupling

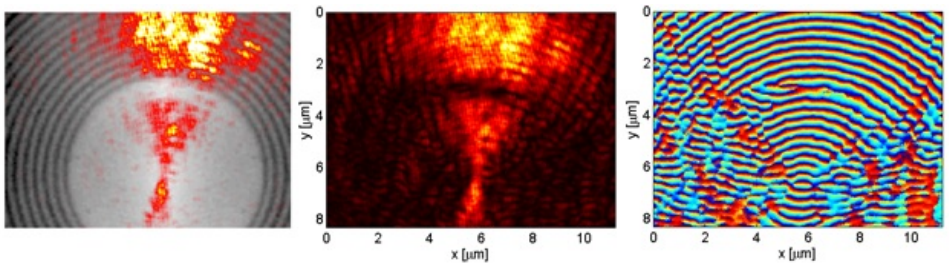

Figure 2.9: In sequence: white light image of the patterned surface superposed to the intensity distribution obtained by collecting only the leakage radiation.Amplitude and phase distributions of the optical fields collected at the surface with the same field of view of the first image.

only from those regions having grating vector perpendicular to the laser polarization. In the present case, for a y-polarized incident beam, the leakage radiation associated to the focused BSW has a two-lobe symmetric distribution oriented along the x-axis (fig. 2.10a). When the laser polarization is rotated, the observed pattern is rotated accordingly.

The BSW focusing effect produces a subwavelength central lobe in the spacer center, with an estimated Full Width Half Height of about 200 nm (fig. 2.10c). We observe that the amplitude profile shows a fringe pattern with a spatial frequency doubled as compared to the wavefront frequency appearing in figure 2.10d. This is due to an interference effect by two counter-propagating BSWs. The phase cross-section along the horizontal line sketched in figure 2.10b shows a sawtooh profile indicating the two counter-propagating BSWs converging at the grating center where a phase singularity can be appreciated (fig. 2.10d). The existence of these two counter-propagating BSWs can be better appreciated by considering the Fourier spectrum amplitude calculated from the complex field (obtained from measured amplitude and phase) along the horizontal line (fig. 2.10e). The Fourier spectrum amplitude exhibits two main contributions peaked at spatial frequencies $f_x = 62.02\mu m^{-1}$, corresponding to the calculated BSW spatial frequency obtained from the BSW dispersion shown.

The benefits from BSW focusing can be appreciated in cases wherein a selective enhanced fluorescence excitation is desired in the spacer center only. Fluorescence measurements are performed after incubation of AlexaFluor 546-labelled protein A on the sample. In this way,

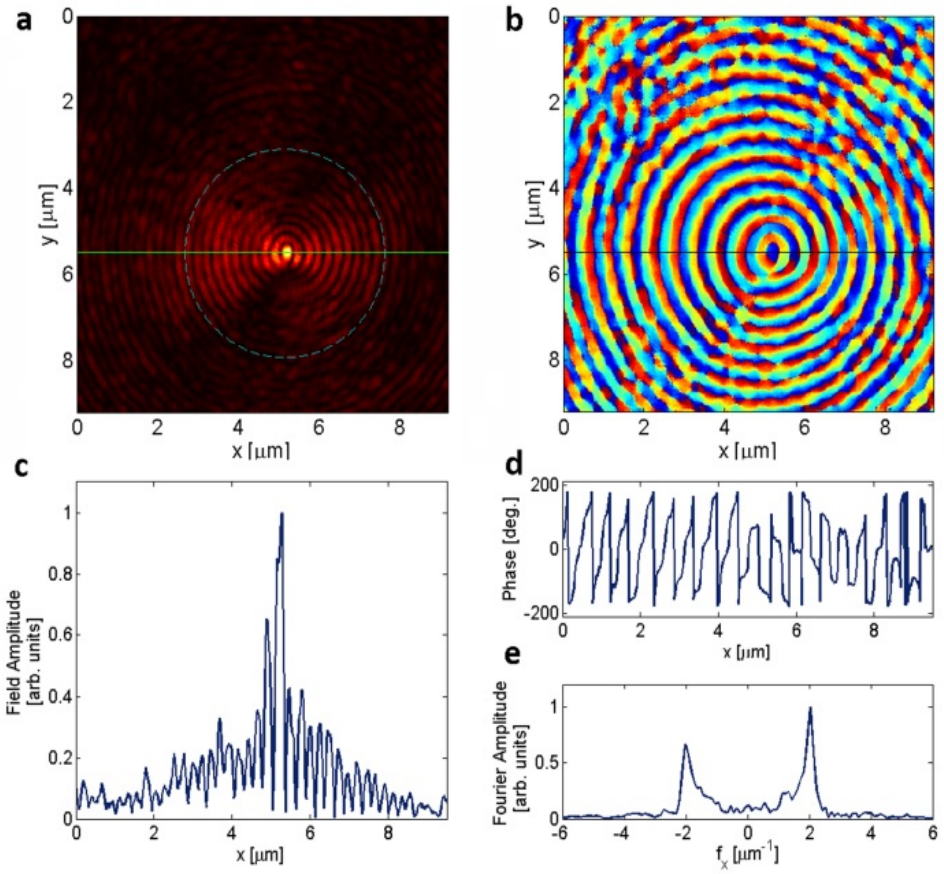

Figure 2.10: (a), amplitude and (b), phase distribution of the leakage radiation associated to a converging laser BSW. Coupling is performed by illuminating a circular grating ($D = 5\mu m, L = 520nm$) on a "regular" multilayer with a linearly polarized (y-direction) laser ($\lambda = 532nm$). The dashed circle indicates the boundary on the inner spacer. (c), cross-sectional field amplitude profile along the horizontal line shown in (a). (d), cross-sectional field phase profile and (e) its corresponding Fourier spectrum amplitude along the horizontal line shown in (b).

a rather photostable fluorescent layer can be homogeneously provided over a large surface area. Figure 2.11 shows direct plane fluorescence images of a ring structure homogeneously illuminated by a collimated laser.

The setup used for these measurements is the fluorescence microscope described in Chapter 1, figure 1.4. The illumination area is extending well beyond the lateral size of the circular grating. Moreover, it is worth to underline that fluorescence collection is performed here by a NA = 0.2 objective working in air, in such a way that the BSWcoupled fluorescence leaking into the substrate is prevented to

contribute to the image formation. When the incident laser is circularly polarized, a fluorescence image as shown in figure 2.11a is collected. We observe some fluorescence emitted from the whole grating surrounding a bright spot located in the spacer center. Although the organic emitter is homogeneously distributed on the whole multilayer surface, at the outside of the ring structure the background fluorescence is rather low. By taking a (normalized) intensity profile along the horizontal line drawn in figure 2.11a, the intensity contrast across the structure can be better appreciated. The bright central spot shows a fluorescence intensity that is roughly 10 times higher than the fluorescence coming from the outside of the ring (fig. 2.11b). This increase in fluorescence is produced by the BSW coupling and focusing from the laser illumination. Since the spacer region is flat

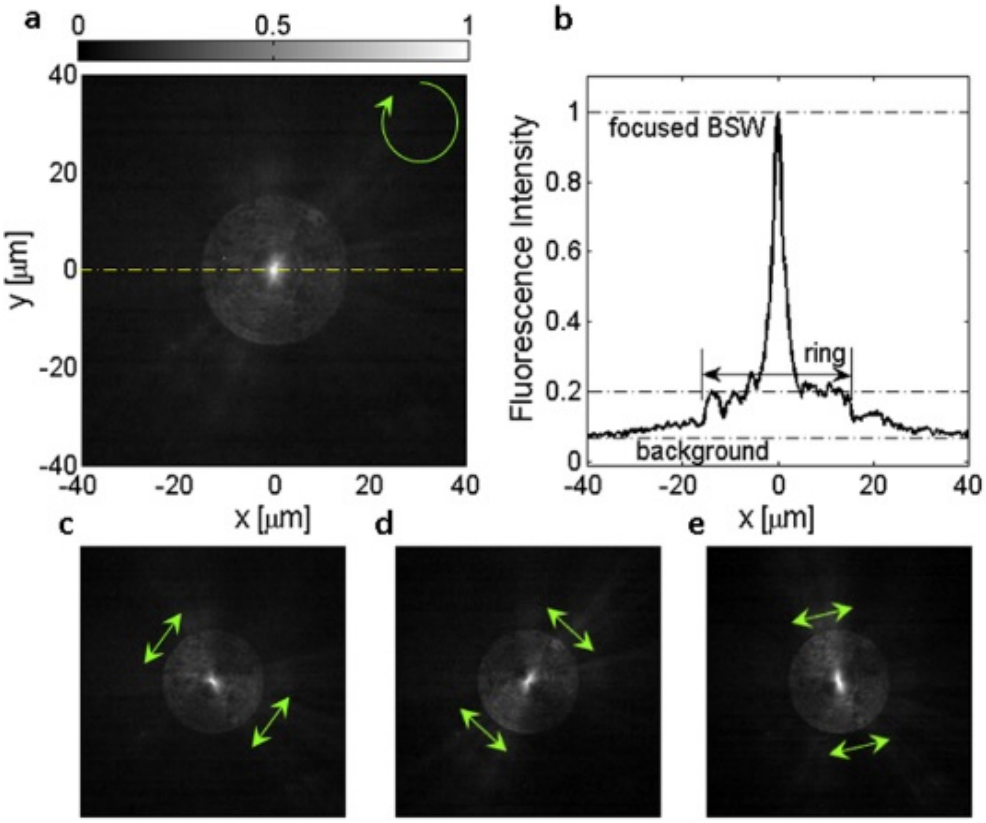

Figure 2.11: (a), fluorescence image of a laser BSW coupled and focused by a circular grating ($D = 8\mu m$, $L = 520nm$) on "low leakage" multilayer. Illumination is a collimated, circularly polarized laser beam. (b), cross-sectional fluorescence intensity along the dashed line in (a). (c), (d), (e), same as in (a) with an incident laser beam linearly polarized as sketched by the arrows in the figures. All images are collected by means of the setup sketched in 1.4.

and rather wide, any physical accumulation of the emitting molecules on the surface can be excluded. In case the incident laser radiation is linearly polarized, the fluorescence pattern shows a two-lobed shape, whose orientation rotates depending on the orientation of the laser polarization (fig. 2.11c-e).

By comparing results with the interferometric analysis of figure 2.10, we can conclude that the fluorescence distribution presented above mainly represents the fluorescence trace of the BSW coupled from the laser. In this chapter I've shown that radiation coupled to BSW can be manipulated on the surface of a 1DPC by means of refractive or diffractive structures. In the next chapters, I will show that the same structures can be employed to extract radiation coupled to BSW, eventually emitted by localized sources, and redirect it into a highly directional collimated beam.

Chapter 3

Bloch Surface Waves Coupled Fluorescence

3.1 Coupling of emitters with photonic structures

Since the pioneer work of Purcell,[17] it is well known that the emitting properties of a light source can be strongly modified by the photonic environment. According to the *Fermi's 'golden rule'* applied to the decay properties of an emitter, both the emission rate and the direction of emission are affected by the Local Density of electromagnetic States (LDOS).[54] In analogy with the density of electronic states (DOS), the LDOS counts for the available electromagnetic modes in which photons can be radiated from a specific location. For example, in the case of an ideal point-like source in free-space, the available modes are the infinite propagating plane waves, that are the eigenmodes of the vacuum. The emission in this case results in a spherical isotropic radiation pattern.

When the refractive index in close proximity to the emitter spatially varies on the length scale of the order of the wavelength, as in the case of photonic crystals, the decay properties of the emitter are modified according to the photonic band structure.[55] Because of Bragg's diffraction causing constructive and destructive interference along certain directions, the radiation pattern can be strongly angularly dependent.[56] In the case of a three-dimensional photonic crystal exhibiting a complete band gap for a given range of frequencies, the

radiative decay can be almost completely inhibited.[16]

Although the high directionality achieved by employing photonic crystals has found application in different fields such as biosensing[57] or quantum information,[58] it suffers from some inherent limitations. First of all, the electric field distribution associated with the photonic modes is usually mainly distributed inside an high refractive index material,[59] meaning that in order to have an efficient transfer of energy from the emitter to the guided mode, the emitter itself has to be buried inside the photonic structure, which can be a limiting factor especially in sensing applications. Another main disadvantage regarding photonic structure is that the spatial dimensions required are of the order of the wavelength because of the diffraction limit. Such limitation has been overcome by employing resonant metallic nanostructures exhibiting Surface Plasmons. In particular, the exploitation of Localized Surface Plasmon Resonances (LSPRs) on metallic nanoparticles has led to the possibility of localizing an extremely intense electromagnetic field in a deep subwavelength volume, giving rise to the concept of optical nanoantenna.[60]

Despite the disruptive impact of nanoantennas in nano-photonics and in many applications related to it, there are still some issues limiting the performances of LSPR-based devices. The main drawback concerning the exploitation of SPs is the intrinsic lossy behavior of metals at optical frequencies, due to the scattering of free-electrons oscillating in the metal under the driving force of the electromagnetic field. Ohmic losses result in absorption of useful signal as well as in a broadening of the resonance, corresponding to a lower quality factor of the resonance and, therefore, to a lower directionality if compared to photonic crystal performances.

A well-known effect occurring when an emitter lies in close proximity with a metallic surface is the so called Surface Plasmon Coupled Emission (SPCE),[61] occurring because of the strong modification of the LDOS induced by a resonant metallic structure. In the case of an emitter lying on the surface of a flat metallic thin film supporting SPPs in the wavelength range of emission, a significant portion of the light emitted couples to the SPPs. The emission pattern is therefore modified according to the dispersion relation of the SPPs and, if the metallic film is grown on a glass substrate for example, photons leak into the substrate at an angle which is larger than the critical angle

for the substrate and proportional to the SPP wavevector.

As already mentioned in the first chapter, in a phenomenological picture BSW can be seen as the photonic counterpart of SPP, since they are characterized by an enhanced density of electromagnetic states close to the truncation interface of the multilayer and an exponentially decaying profile both in the external dielectric medium and inside the multilayer, since BSW lye beyond the light line and inside the forbidden band of the multilayer. As a consequence of an enhancement of the LDOS occurring at the interface of properly designed 1DPC, an effect similar to SPCE occurs when BSW are considered.[62] In this chapter, I will show that BSW-Coupled Fluorescence (BSW-CF) can be exploited to obtain a highly directional fluorescent emission combining the advantages of using a surface mode instead of a typical buried photonic mode, with the intrinsic absence of ohmic losses typical of dielectric materials.

3.2 Bloch Surface Wave Coupled Fluorescence on flat One Dimensional Photonic Crystals

The enhanced density of electromagnetic states at the truncation interface of the multilayer modifies the emitting properties of a light emitter thereon located.[51] The elementary cell of the design proposed here is composed by four pairs of an high index layer of Ta_2O_5 ($n_h = 2.08$ at 600 nm) and a low index layer of SiO_2 ($n_l = 1.45$ at 600 nm). The thickness are respectively 95 nm and 137 nm, while the last layer of SiO_2 is only 127 nm thick. In figure 3.1a the reflectance map of the new design (6 pairs) is shown. The new design (sketched in the inset) has been chosen because, compared to the previous one, it has a BSW exhibiting a higher electric field enhancement at the surface and penetrates much deeper in the external dielectric medium (see figure 3.1b), and is therefore more sensitive to surface modifications.

In order to evaluate the near-field coupling we modeled the radiation of an electromagnetic field in a 2D FEM model (figure 3.2a) implemented in COMSOL 4.2a RF module.

The modeling domain is a vertical cross-section of the multilayer

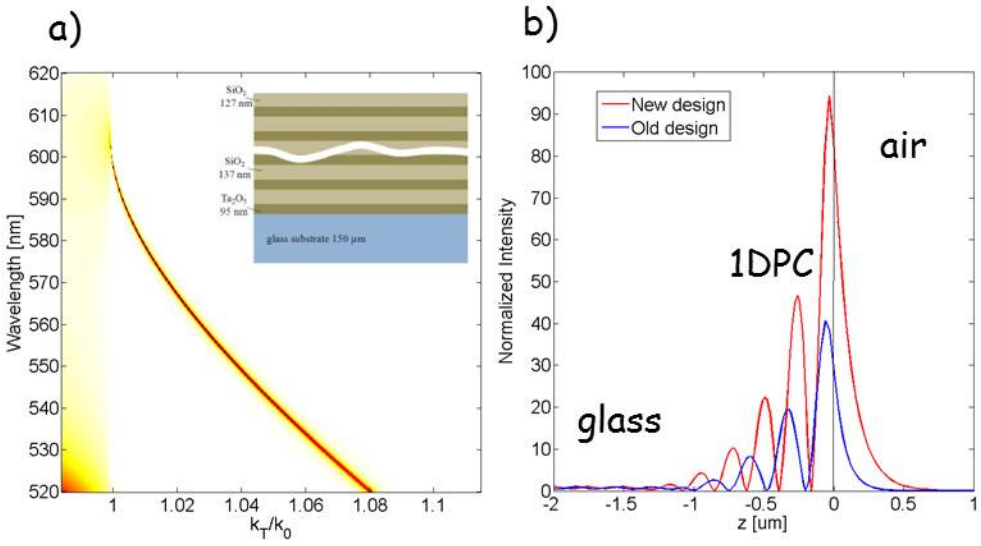

Figure 3.1: (a) Calculated TE reflectance map function of the incident wavelength and the transvrerse wavevector component normalized with respect to the free-space wavevector referred to the multilayer design sketched in the inset. (b) Calculated electric field distribution of the BSW along the multilayer cross-section. The black line indicates the truncation interface position. The intensity has been normalized with respect to the propagating radiation in the glass. The red line is associated to the BSW sustained by the design in (a), while the blue one is associated to the BSW discussed in the previous chapters.

and the emitter is placed 5 nm above the surface. The entire domain is surrounded by Perfectly Matched Layers (not shown in figure) so that boundary reflections are avoided and the domain resembles an open domain.

In order to have an effective coupling, a polarization matching between the radiated field and the BSW mode is required. The BSW is TE polarized, meaning that there are 2 possible orientations of the electric field, both matching the polarization of the BSW. We chosed to have the electric field out of the plane of the cross section, in order to have the Poynting vector in-plane. To do this, the emitter has been modeled as a line of oscillating current orthogonal to the sheet and emitting radiation at a wavelength of 580 nm in the exemplary image shown.

The modeling result shows that there is a cone of light radiated in air and transmitted through the multilayer into the glass, but when the Poynting vector direction approaches the direction parallel to the

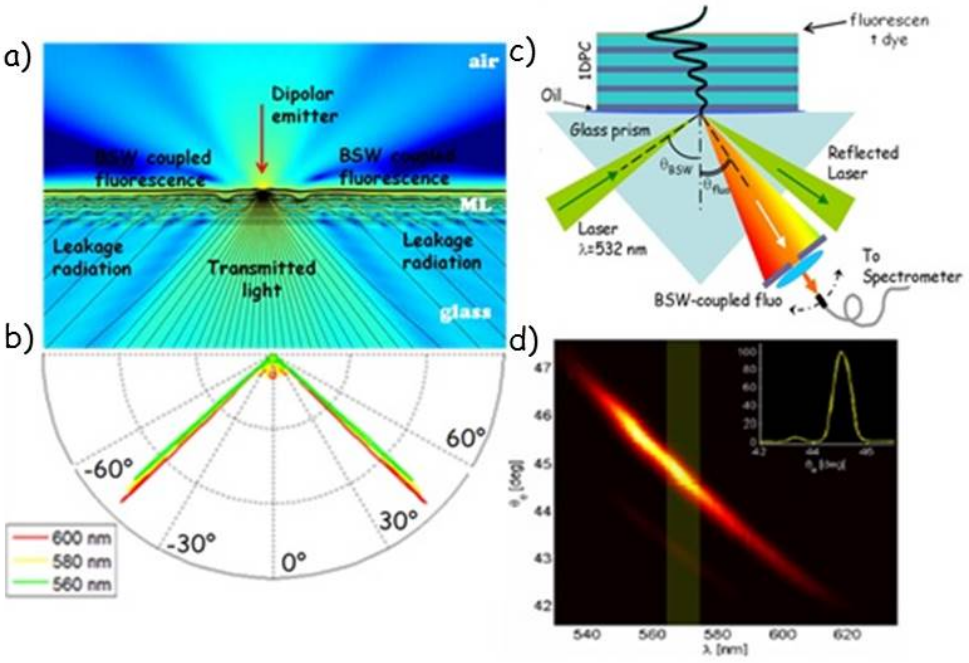

Figure 3.2: (a) Calculated near-field distribution of the electric field radiated by an emitter modeled with an out-of-plane line of current. The resutling field in the FEM model is TE polarized. (b) Calculated far-field radiation pattern corresponding to the near-field distribution in (a) for different radiated wavelengths. The radiation pattern shows the dispersive behaviour of the BSW-coupled fluorescence and the highly directional emission. (c) Sketch of the experimental setup employed to evaluate the beaming effect due to the coupling of emitters with Bloch Surface Waves. (d) Experimental fluorescence intensity map function of (λ, θ). The dispersion relation of the BSW is reproduced by the BSW-CF collected. In the inset, a vertical cut at fixed wavelength along the yellow band is reported, showing the angular divergence of the beam collected.

surface, the major part of the light is squeezed into the BSW and propagates along the truncation interface. Such squeezing is well described by the black continuous lines indicating the power flow. As long as the BSW-CF propagates at the multilayer interface, part of the energy tunnels through the multilayer and leaks into the substrate. According to the momentum conservation law, the leakage radiation propagates into the substrate at a specific angle determined by the BSW dispersion relation according to the following relation:

$$k_{BSW} = k_0 n_{sub} \sin(\theta_{BSW}) \tag{3.1}$$

where k_{BSW} is the BSW wavevector, k_0 is the free-space wavevector,

n_{sub} is the substrate refractive index (in our case $n_{sub} = 1.5$) and θ_{BSW} is the leaking angle.

Since BSW are characterized by a well-defined dispersion relation, different wavelengths will couple to BSW with a different wavevector, and will be therefore out-coupled at different angles. A tool provided by COMSOL allows to compute the far-field radiation pattern corresponding to a specific near field distribution based on the surface equivalent theorem. Different oscillating frequencies have been set for the line of current, and the corresponding far-field radiation pattern has been computed for each of them.

In the polar plot in figure 3.2b, three exemplary patterns at three different wavelengths are presented, and it is observable a change in the output angle. More specifically, longer wavelengths correspond to smaller wavevector and therefore to smaller output angles.

By employing a reverse Kretschmann configuration it is possible to recover the BSW dispersion relation in fluorescence. In figure 3.2c is reported a sketch of the experimental setup. Fluorescence out-coupled via the prism coupling is collected with a very low numerical aperture system, namely the inlet of a fiber connected to a spectrometer. Such setup provides reasonably high spectral and angular resolutions. The fluorescent probe is an homogeneous layer of Protein A conjugated with Alexa Fluor 546 (PtA Alexa). The homogeneity has been obtained by covering the surface with a droplet of a solution containing PtA Alexa ($1\mu g/ml$) and incubating it for 20 min. The sample was then rinsed with PBS to remove the excess of PtA Alexa and reduce the presence of clots on the surface. The bright band observed in the measured map in fig. 3.2d corresponds to the BSW-CF and shows a clear dispersive behavior. In the inset an intensity profile extracted along the yellow band shows that a specific wavelength is radiated in a well defined angular range.

As already mentioned in the first chapter, leakage radiation can be efficiently collected by employing an high numerical aperture oil immersion objective. In order to collect fluorescence leakage radiation, the experimental setup shown in fig. 1.4 has been modified as depicted in fig. 3.3a. Briefly, fluorescence on the surface of the 1DPC is excited with a collimated laser beam (Nd:Yag, $\lambda = 532nm$) and imaged on the RGB CMOS camera after filtering out the excitation light with an edge filter (Semrock 532 nm RazorEdge). The adjustable tube lens in front

of the CMOS camera allows to image both the direct plane, i.e. the spatial distribution of light collected in the focal plane of the objective and the Back Focal Plane, that is the Fourier Transform of the direct plane and provides information about the angular distribution of the field collected.[63] Figurefig:3.3b shows an example of Back Focal Plane imaged when fluorescence is excited on the flat surface of a 1DPC. The outer and inner dashed white circles indicate respectively the NA of the objective and the light line. The bright ring of fluorescence observed beyond the light line corresponds to the projection of cone of emission resulting from the leakage of the BSW-CF, schematically depicted in fig. 3.3a. The RGB image allows to qualitatively evaluate the BSW dispersion.

The fluorescence ring is characterized by an external green area that turns into red light approaching the light line. A cross-section of R and G channels along the yellow dashed line (sensitivity of the RGB camera can be found in[?]) allows to better evaluate the dispersive behavior of BSW-CF emission and compare the experimental results to the theoretical predicted output angles. The normalized transverse wavevector ($k_T/k_0 = n_{eff}$) associated to the green part of the spectrum has a maximum at 1.09 corresponding to an output angle of 46.6°, while the maximum associated to the red part occurs at $n_{eff} = 1.05$, corresponding to 44.4°. Such values are compared to output angles calculated for $\lambda_G = 540nm$ and $\lambda_R = 600nm$, that are respectively 46.5° and 44.5° and are in good agreement with the experimental results.

In order to have an efficient coupling with BSW, fluorescence has to be radiated by dipoles oriented parallel to the surface As a consequence, BSW-CF will exhibit a well defined polarization that will be azimuthally oriented (see white arrows) in the specific case of TE polarized BSW (conversely, SPCE occurring on a flat metallic film is radially polarized, reflecting the TM nature of SPPs[64]).

3.2.1 Leakage radiation suppression

In the first chapter I've discussed the effect of increasing the number of pairs composing the 1DPC on the overall losses and, therefore, on the decay length of BSWs. Since ohmic losses are negligible in the visible range, the main radiative channel draining energy away

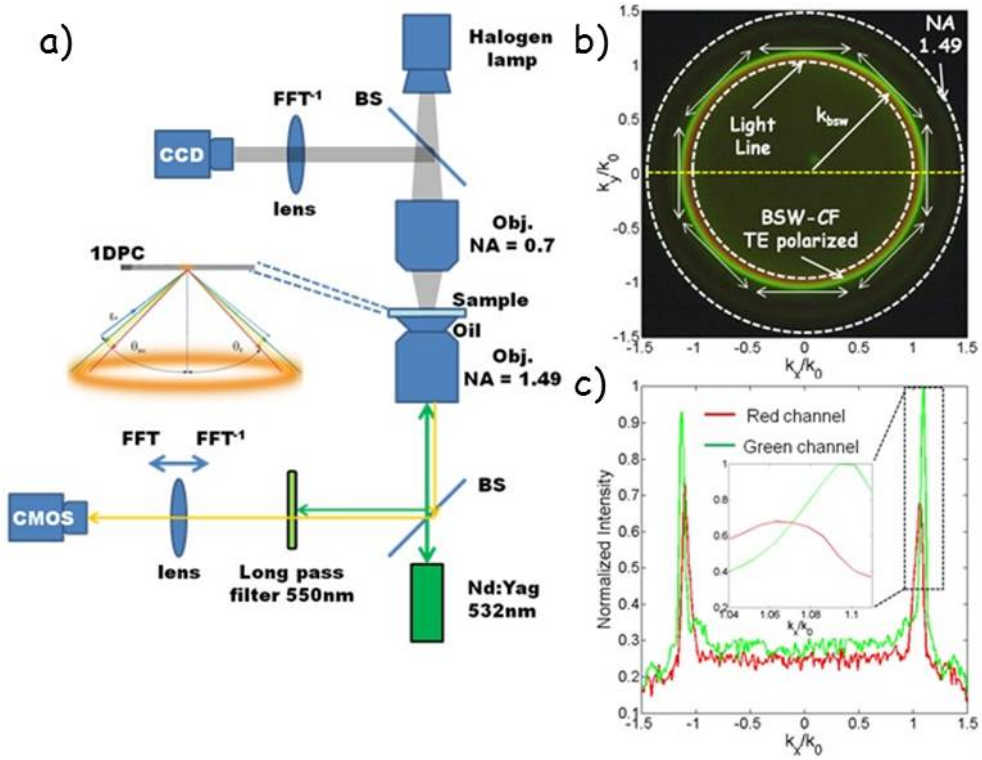

Figure 3.3: (a) Schematic view of the experimental setup used to evaluate the Bloch Surface Wave Coupled Emission, consisting in a customized fluorescence leakage radiation microscope. (b) Example of real color fluorescence Back Focal Plane image collected when fluorescence is excited on the flat surface of a 1DPC. The external white dashed ring indicates the maximium angle collectable by the high NA oil immersion objective, while the internal one signs the air/glass light line. The bright dispersed ring beyond the light line corresponds to the BSW-CF collected, that exhibits a well-deined polarization specified by the white arrows. An intensity cross-section is reported in (c), where the normalized intesities collected by the R and G channels of the CMOS camera are reported. In the inset, a detail about the angular position of the two peaks is reported.

from the surface mode is the leakage through the multilayer into the substrate.

Leakage of radiation into the substrate can be interpreted as a tunneling event due to the finiteness of the multilayer. By increasing the number of pairs composing the multilayer the tunneling event can be frustrated and leakage radiation can be suppressed. The coupling of the surface mode with the propagating substrate modes is therefore reduced, reducing not only the radiative decay of the BSW mode but also the effectiveness of transfer of energy either with a prism or with

an oil immersion objective is reduced.

When fluorescence radiated on the surface of the multilayer is considered, the coupling of the radiated energy with the BSW naturally occurs. In fig.3.4a is shown a numerical comparison between the radiation patterns of point-like emitters lying on the surface of two 1DPCs composed by different numbers of the same elementary cell (respectively 4 pairs and 10 pairs of layers).

Although the amount of directly transmitted light through the multilayer and in air is the same, the two peaks in the substrate corresponding to the leakage radiation are suppressed when the, meaning that the major part of fluorescence coupled to BSW has not been radiated in far field and it is still guided on the surface of the 1DPC at the boundaries of the modeling domain which is about $100\mu m$.

In order to experimentally prove the numerical calculations, we employed the fluorescence leakage radiatio microscope described above. In fig. 3.4 b and c two fluorescence images of the back focal plane are presented, corresponding to fluorescence excited on the flat surface of a 1DPC with four pairs of layers (b) and ten pairs (c). The first image is dominated by the bright ring beyond the light line described above. The second one appears brighter because a higher excitation intensity has been used to put in evidence the structure of the Back Focal Plane. It is confirmed by the much higher intensity of the directly transmitted light within the light line. At the angular position where the BSW-CF is expected there is a shortage of light, indicating that BSW-CF does not leak anymore into the substrate and it is therefore no more collectable in far field.

To have a better comparison, the intensity profiles extracted from (b) and (c), normalized with respect to the directly transmitted light, are compared. The angular position of the BSW is characterized by a peak of fluorescence in the *4 pairs* design, while at the same position a dip in fluorescence is observable when the *ten pairs* design is considered. Therefore, in the low leakage design, BSW-CF is forced to remain confined at the surface and the main factor reducing the propagation length are the surface defects and ohmic losses of the layers, and are in the end determined by the performances of the fabrication process.

In the next chapters, we I will discuss the use of surface structures to manipulate BSW-CF. The possibility to control the leakage

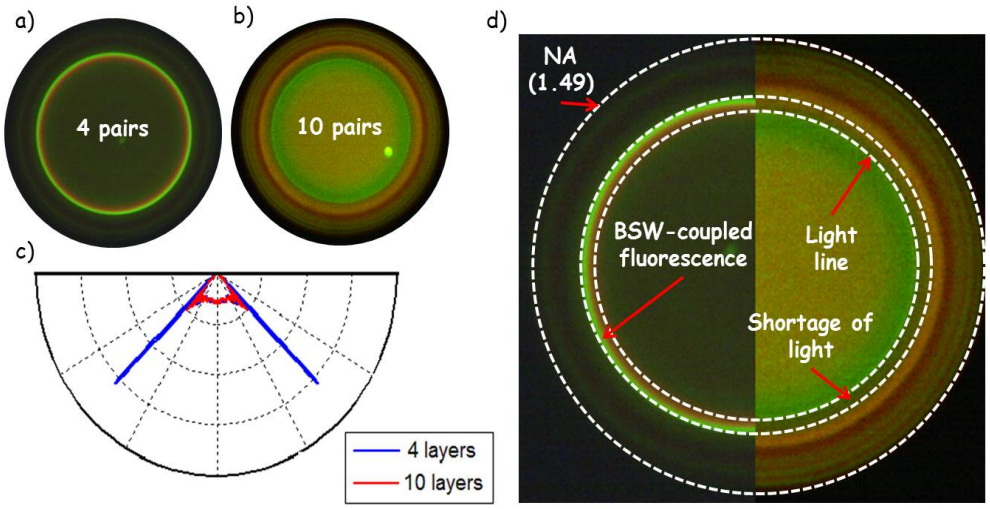

Figure 3.4: Experimental fluorescence measure showing the BFP collected when fluorescence is excited on the flat area of a four pairs (a) and ten pairs (b) 1DPC. (c) Calculated far-field radiation pattern in glass when an emitter is placed close to the surface of two 1PDCs. The blue line corresponds to the case of a 1DPC with 4 paris, while the red one refers to the case of a 10 pairs 1DPC. The pattern is calculated starting from a near-field distribution (not shown here) computed with a FEM model. (d) Merge of (a) and (b) the help the comparison of the two BFP. On the left side, the four pairs design clearly shows a bright fluorescence right just beyond the light line, that changes into a shortage of light on the right side (ten pairs design).

radiation and eventually suppress it gives an interesting advantage in this framework: the interaction of fluorescence coupled to the surface modes with distributed surface structures can be indeed enhanced if the radiative decay channels are reduced.

Chapter 4

Directional extraction of fluorescence: linear surface gratings

In the first chapter I've shown that a relief grating patterned on the surface of a one dimensional photonic crystal can provide the momentum necessary to couple far-field radiation to BSW.

Here, I want to show that the reverse effect can be exploited to efficiently beam out radiation coupled to the evanescent modes in a well-defined direction. Such effect has been widely reported when SPCE on a periodically corrugated metallic film is considered.[65,66] Although an effective beaming effect assisted by Surface Plasmons (SPs) has been reported by several groups, the performances of such systems are often limited by the typical decay lengths of SPs that, in the visible range, do not exceed few tens of microns.[21] Moreover the directionality of emission is intrinsically limited by the broadness of SPs resonances, mainly due to ohmic losses. For the above mentioned reasons, we expect that longer decay length as well as a narrower resonances provided by the photonic crystal platform would allow for a more efficient directional extraction of fluorescence.

SPCE as well as BSW-CF provide an efficient tool to beam the emitted radiation in a well-defined direction, not differently to what happens when an emitter is placed in a dielectric waveguide. The main issue in practical applications is that leakage radiation associated with the resonant mode at a given wavelength has a wavevector larger than the wavevector of free-space radiation, so that it cannot propagate in air unless a prism-coupled configuration or an oil immersion objective is considered. The use of relief gratings patterned on the surface of the

1DPC should allow to diffract energy coupled to BSW into free-space radiation propagating in a direction defined by the Bragg's law.

The ability of controlling the directivity of spontaneous emission is an objective of outstanding relevance in a variety of fields dealing with fluorescent emitters, such as bio-sensing when labelled markers are employed[56] or quantum information applications based on transmission of single photons emitted by single photon sources, such as Nitrogen Vacancy centers in diamonds.[67] The enhanced directionality of spontaneous emission would allow to enhance the collection efficiency of fluorescence by employing low numerical aperture systems that can operate also from the dielectric medium side (and not necessarily from the substrate as in the case of oil-immersion objectives).

4.1 Linear surface grating on one dimensional photonic crystal:FEM model

In the following, we consider a linear grating patterned on the surface of a 1DPC. The elementary cell characterizing the 1DPC is the one described in chapter 3. Once the dispersion relation is known, the Bragg's law can be used to determine, to a first approximation, the grating period needed to normally diffract BSW-coupled fluorescence. It is a first approximation since it does not take into account that, either if the grating is fabricated by etching the last layer or by depositing additive dielectric material on the surface, it modifies the dispersion relation according to the dielectric loading effect described in the second chapter.

In order to optimize the grating parameters (i.e. the period and the depth), the FEM model described in the 3^{rd} chapter has been modified by adding a grating around the emitter (fig. 4.1a). The grating was optimized to normally diffract radiation at 570 nm, which is the peak emission wavelength of PtA Alexa 546, the fluorescent probe used in the experimental observations. Since we found that the maximum of efficiency of the grating is obtained with a depth of about 100 nm (calculations not shown), we considered a relief grating of SiO_2 100 nm thick surrounding the emitter. The near field distribution (fig. 4.1b) shows that fluorescence radiated couples with the surface modes and propagates along the truncation interface. The presence of the

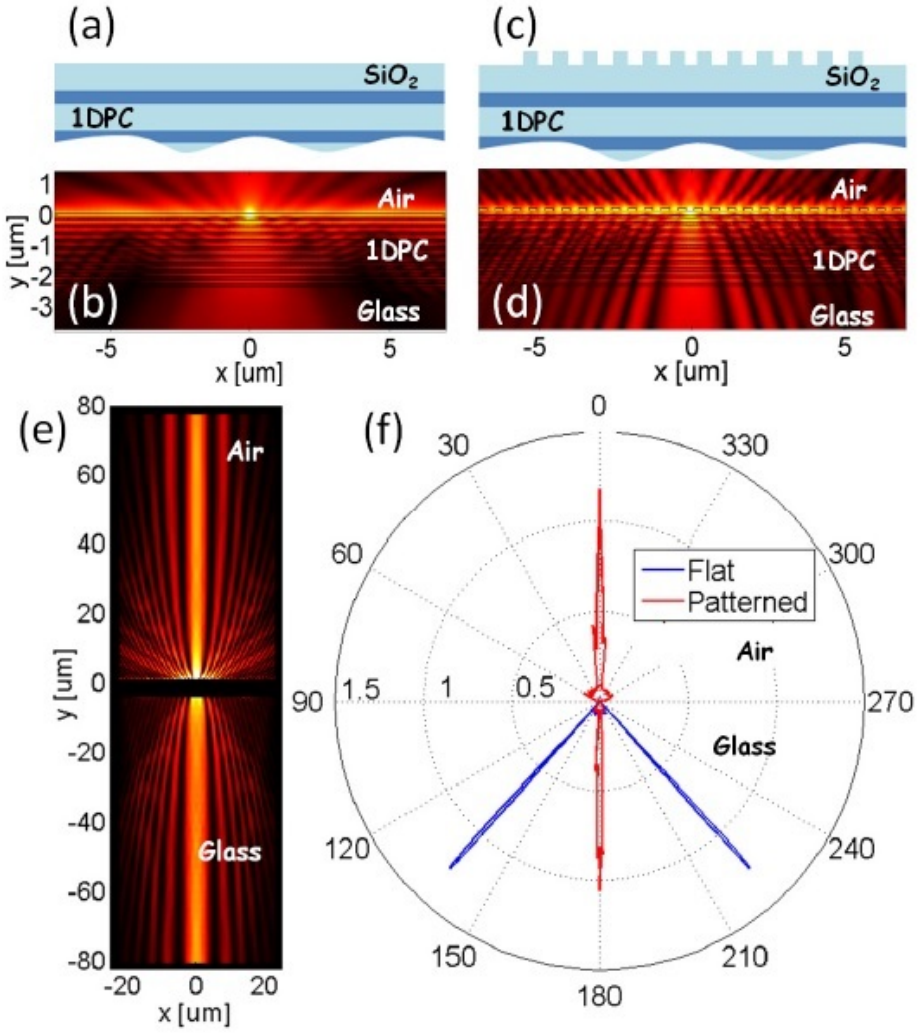

Figure 4.1: Cross sectional sketch of flat (a) and patterned (c) multilayer; calculated near-field intensity distribution of light radiated by an emitter close to the surface of a flat (b) and patterned (d) multilayer; (e) expanded view of the intensity distribution of BSW-coupled diffracted fluorescence; (f) angular pattern of emitted light in the case of flat and corrugated 1DPCs, highlighting the BSWassisted beaming effect.

ridges along the path produces a series of scattering events producing a diffraction pattern. By enlarging the simulation domain (fig. 4.1c), it is visible the formation, far from the surface, of a normal beam due to the coherent superposition of the scattered light. By computing the far-field pattern (fig. 4.1d), a pronounced normal beam is generated both in air and in the substrate, while the two lateral beams associated to leakage radiation of BSW-CF on a flat surface (here reported for easy comparison) are no more visible. The far-field radiation pattern

shown in the figure refers to the cumulative radiation patter obtained by integrating over the emission wavelength range of 550-600 nm and it predicts a divergence of the overall beam of $\approx 5°$ in air.

4.2 Experimental results

In order to observe the angular distribution of fluorescence, the leakage radiation microscope described in the 3rd chapter is used. The diffractive structure considered is the one schematically shown in figure 4.2a, and it has been patterned both on a 1DPC with 4 pairs of layers.

Fig. 4.2b shows the fluorescence image of the BFP collected on the 4 pairs layers design. Superposed to the bright circle associated with the leakage of BSW-coupled fluorescence, the BFP fluorescence image reveals two additional (polychromatic) bright arcs, mutually intersecting in the center. A similar result has been found for SPCE on periodically corrugated metallic films. In fact, when the grating vector equals the wavevector of the surface mode wherein the emission is coupled, a normal diffraction may occur normally to the sample surface. In this case, since BSW-coupled fluorescence is leaking isotropically with respect to the xy-plane and the grating is oriented along the x-direction, diffraction only affects the k_x direction of propagation, through the corresponding wavevector components:

$$k_x = 2\pi/\lambda n_{obj} sin(\theta_x) \tag{4.1}$$

for each wavelength λ.

In order to put in evidence the polarization dependence of the BSW coupling, a polarization filter has been added along the collection path (figure 4.2). The image reveals the TE nature of BSWs and confirms that the diffracted light maintains the polarization state, confirming that it is the BSW-CF that is diffracted.

By looking more particularly at the R and G channel intensity profiles presented in figure 4.2d along the $k_y = 0$ (dashed) line in 4.2c, the appearance of a central peak is observed. If we restrict our analysis to the R channel, whose sensitivity is maximized in the spectral range 580 - 620 nm (the same considered in the far-field pattern calculations) we can apply the Bragg's equation for a $\Lambda_g = 520nm$ grating. For a

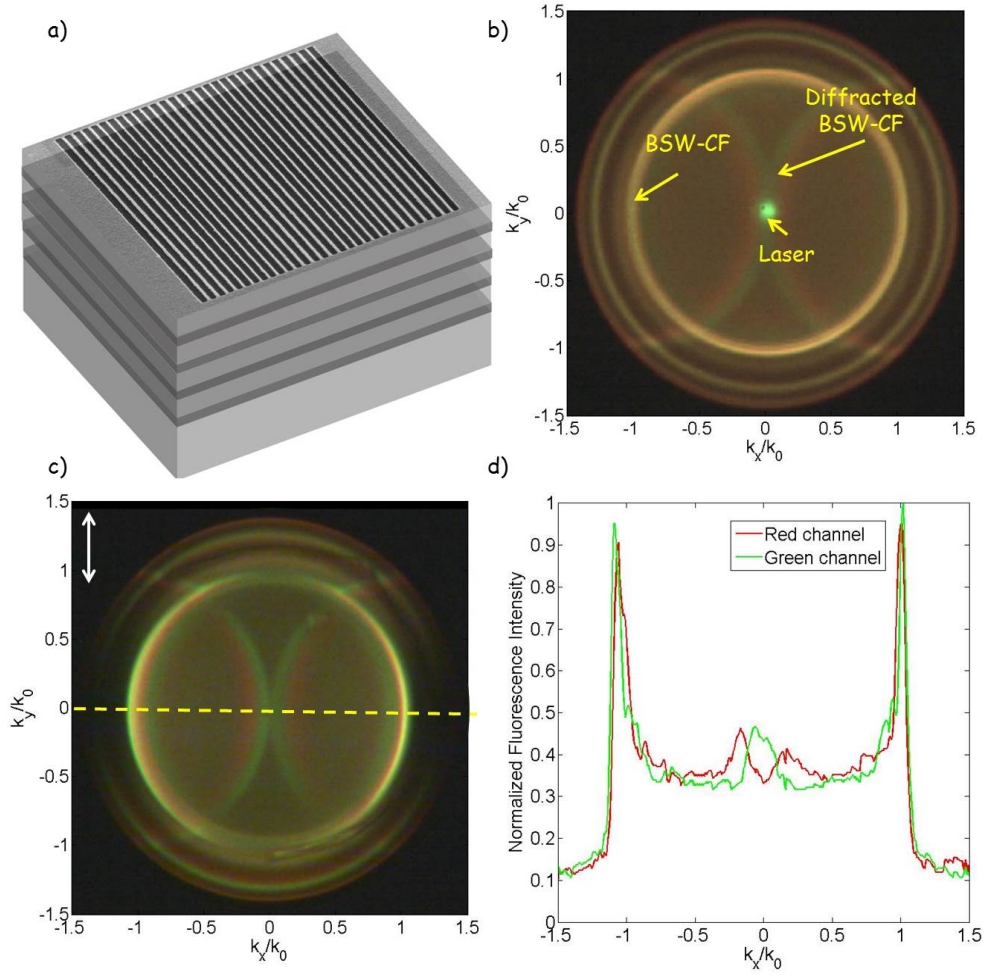

Figure 4.2: (a) Schematic view of the linear grating patterned on top of the 1DPC. The top image is a SEM image. (b) Fluorescence BFP image obtained when by colllecting fluorescence coming from the patterned area. The two diffracted branches superimposing in the center confirm the BSW-coupled fluorescence diffraction. The bright green spot in the center is the residual laser radiation. The image is formed on an RGB CMOS camera and is therefore a real color image. (c) Same of (b) collected with a polarization filter (oriented according to the white arrow) along the collection path that put in evidence the TE polarization of both the BSW-coupled fluorescence and the diffracted BSW-CF. (d) Intensity profile extracted along the red dashed line in (b). The green channel is affected by the laser residual radiation, while the R channel puts in evidence the normal beam due to the grating effect.

given wavelength λ , we find that $k_x^{-1} = k_x^{BSW} - 2\pi/\Lambda_g$ results in an overall angular range $\theta_x \approx 6°$ associated with the -1 diffraction order of BSW-coupled fluorescence. The chromatic dispersion of the diffracted branches reflects the dispersion of BSWs. The experimental

findings well match theoretical predictions obtained with the simple two-dimensional finite element numerical model described above.

It has to be noticed that the two branches crossing in the center are the replicas of the bright ring corresponding to BSW-CF leakage radiation shifted in the x direction of a quantity equal to G.[68]

4.2.1 Enhancement quantification on a linearly corrugated area

So far, I've qualitatively shown that BSW-CF can be normally diffracted by means of surface relief gratings. In the attempt to take advantage of this effect in an application, a quantification of the enhancement obtained for a given numerical aperture of the collection system is required.

To this aim, the experimental setup has been modified according to the scheme presented in figure 4.3a. A 532 nm laser beam (Nd:Yag 10 mW) is expanded by means of a 0.1 NA objective and a movable lens with focal length 10 mm. The divergence of the beam can be adjusted by moving the lens. Since the grating is fabricated to normally diffract fluorescence, a small divergence of the laser beam is required in order to couple the incident radiation with the BSW and ensure a resonant excitation of fluorescence. The beam passes through a polarization filter and then impinges on the sample. The fluorescence excited on the surface of the 1DPC is collected by a low numerical aperture objective (Nikon 10x NA = 0.2) and passes through a second polarization filter. In this way the contrast between the BSW-CF diffracted by the grating and the fluorescence directly emitted in air is enhanced, since the first one mantains the BSW polarization, differently from the latter one.

The collected radiation passes through two edge filters (FEL 550, Thorlabs) in order to cut off the excitation light and fluorescence is imaged on a ccd camera (Apogent Ascent a694) via a lens so that a real image of the surface is produced.

In this experiment we patterned a square of $250\mu m$ x $250\mu m$ on the surface of a low leakage 1DPC with a linear grating. On top of the surface a solution of PtA Alexa 546 diluted in water ($1\mu m/ml$) was incubated for 20 min. The sample was then rinsed in PBS Tween 0.05

The fluorescence image in figure 4.3b clearly shows that when the

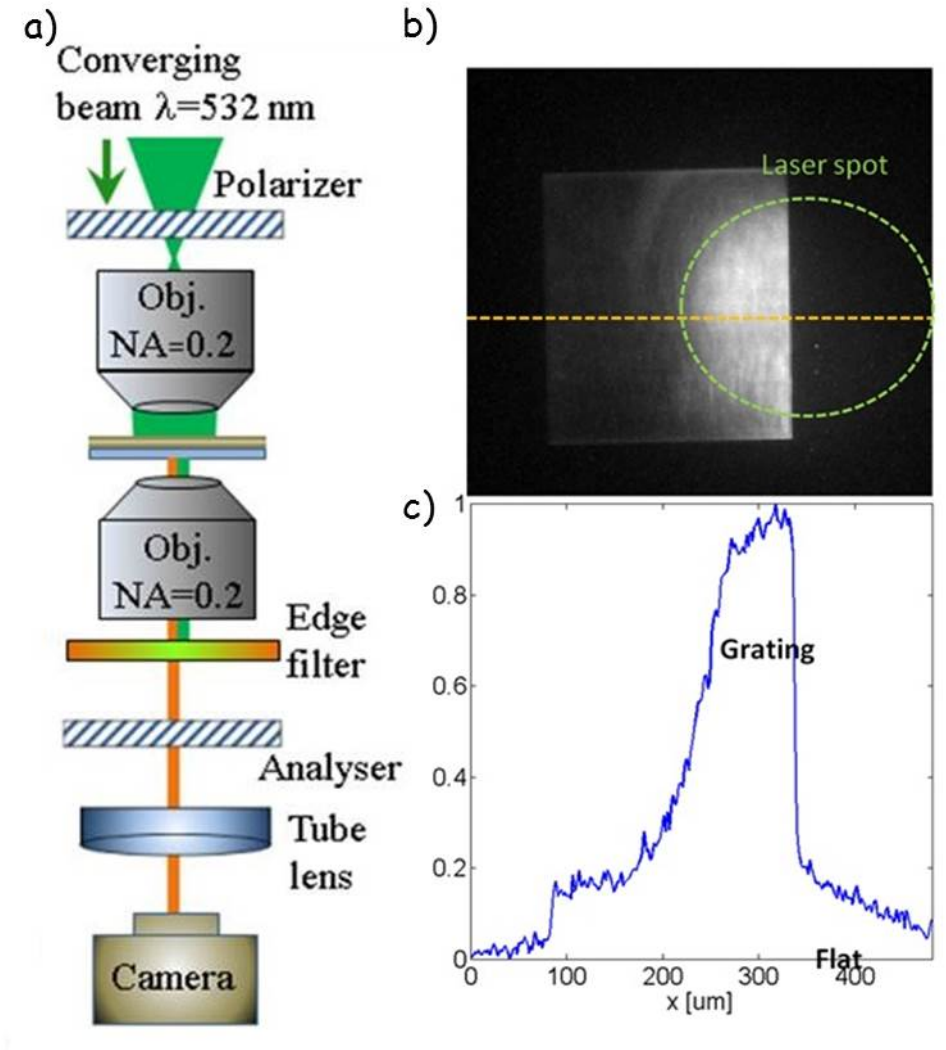

Figure 4.3: (a) Schematic view of the experimental setup employed to characterize the effect of the gratings. A laser beam polarized is weakly focused by a low numerical aperture objective (NA = 0.2). The fluorescence is collected by an analogous objective (NA = 0.2). A polarization analyzer and a spectral filter are added along the collection arm, while a lens allows to image the surface of the 1DPC on a CCD camera. (b) Wide field fluorescence image showing the enhancement due to the grating. The laser spot is partially overlapped to the grating (dashed green circle), while fluorophores are homogeneously distributed on the surface. The linear horizontal cut in (c) taken along the yellow dashed line allows a quantitative comparison between the flat area and the patterned one.

laser beam (dashed yellow circle) excites fluorescence both on the patterned area and on the flat surface, the signal coming from the corrugated surface is much higher than the signal coming from outside the grating. By looking at the image, one can argue that the higher

fluorescence intensity can be simply due to an increased density of fluorophores in the corrugated region, since it can be harder to remove the overlayers of protein from the trenches. To disprove such hypothesis, we experimentally observed that, by rotating the polarization analyzer in the collection arm by 90Â°, the grating disappears and the surface acquires an homogeneous intensity. These results will be discussed in detail in the next chapter, where circularly symmetric gratings are discussed.

The intensity profile extracted along the white dashed line (fig. 4.3c) helps with the quantification of the enhancement: it indeed shows that an enhancement factor of roughly 10 on the fluorescent counts is achieved by patterning the surface. It has to be remarked that such enhancement comes from the combination of both the resonant excitation of fluorescence and the redirection of fluorescence radiated itself. Moreover, due to the high directivity given by the grating, such enhancement factor depends on the numerical aperture of the collection system. In fact, we expect that increasing the numerical aperture of the collecting system will reduce the contrast between BSW-CF diffracted and fluorescence directly radiated in air.

4.3 Linearly corrugated pads for a biosensing application

In microarray diagnostic biochips, a set of bioreceptors are immobilized on the surface in spatially separated spots, aimed at the selective biorecognition of specific ligands.[69,70] Among the optical readout schemes, fluorescence has become the dominant detection/sensing technology in medical diagnostics and biotechnology.[71,72] The microarray approach provides a simultaneous analysis of thousands of parameters within a single experiment, resulting in rapid response time analysis. Compared to colorimetric techniques, fluorescence detection allows significant advantages such as large selectivity and high sensitivity, down to the single molecule level.[73] The detection of low concentrations of target molecules relies on the possibility of enhancing the intensity emission from the fluorescent labels. Several successful approaches have been proposed to this end, including the use of nanostructured surfaces for hosting the spotted bioreceptors.[74]

In an attempt to provide a compact miniaturized chip for an enhanced fluorescence biosensing, we propose here the nanopatterned photonic crystal structure discussed above.

In order to provide a practical implementation of the BSW-assisted fluorescence detection, the photonic structure has been patterned over a large area ($250\mu m x 250\mu m$), and 24 replicas divided in 4 groups of the same pattened pad have been fabricated on the same sample (see figure 4.4.

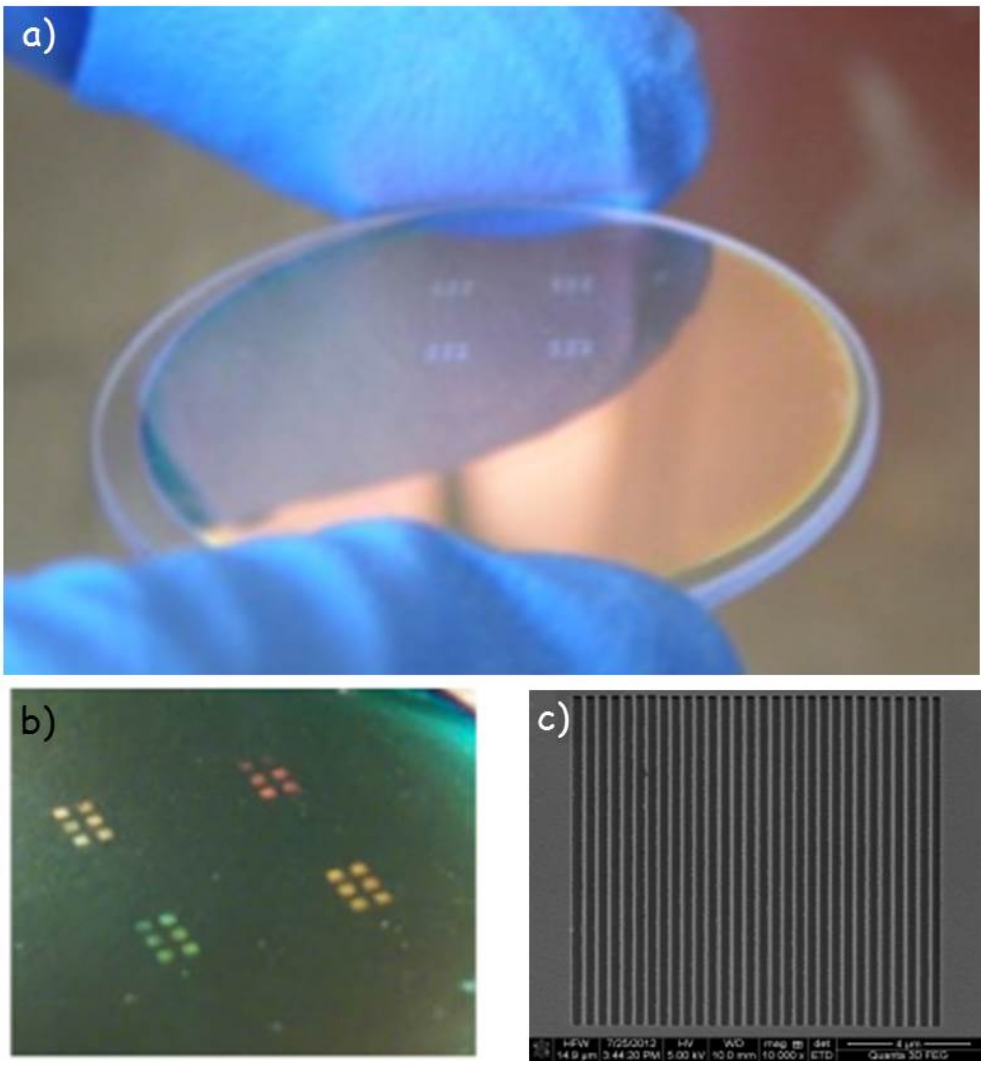

Figure 4.4: (a) Picture of the 1DPC sample with 4 grating groups. (b) zoom on the 4 groups of six linear gratings of diffractive gratings. (c) SEM image of one single grating pad.

A fluorescent-labelled protein A (PtAAlexa Fluor 546) is employed as a target molecule. The protein binding on the 1DPC surface is promoted by a functionalization procedure based on silanization

with 3-aminopropyltriethoxylsilane (APTES)followed by glutaraldehyde binding.

After the surface functionalization, protein solutions at different concentrations are incubated corresponding to the four different grating groups. As a result, proteins are covalently grafted both on the linear gratings and outside them, on the flat 1DPC surface. After incubation, samples are deeply rinsed in PBS-Tween 20 (0,05%) and in deionised water, to remove not specific signal derived from proteins not covalently grafted on the surface. Finally, a nitrogen stream is used for drying.

The detection is performed by means of the fluorescence microscope described in figure 4.2a.

With the fluorescence-labelled PtA grafted on the photonic surface of the optofluidic chip, it is possible to produce a fluorescence image of each single grating by adjusting the magnification of the setup. In alternative, an imaging setup may be provided, allowing a wider field-of-view containing multiple gratings that can be collectively illuminated. In the present case, the laser illuminated area is approximately as wide as the grating, i.e. $250\mu m$.

A titration curve can be built (figure 4.5), by using different concentrations of Protein A-Alexa Fluor solutions ($0.01-0.1-1-2.5-5-10\mu g/mL$) in Phosphate-Buffered Saline (PBS "Dulbecco") prepared by serial dilution. Four different concentrations are incubated in each single run, by exploiting the four different gratings groups, each one provided with a dedicated microfluidic chamber. Fluorescence intensities are collected from the gratings (red line) and from the flat regions (blue line). For each protein concentration, the quantification of the fluorescence intensity has been performed by calculating an average of intensity (see images in the insets) over the illuminated areas either on gratings or on flat regions.

The error bars take into account the intensity variation within each spot and over the 6 gratings of identical concentration. In a double logarithmic plot, both curves show a linear trend for concentrations below $25\mu g/mL$. The one-order of magnitude enhancement is maintained over a large interval of concentrations. However, at lower concentrations, the fluorescence background produced by the photonic substrate and the glutaraldehyde prevents the direct detection of PtA.

Once the Limit of Detection (LOD) associated to the fluorescence

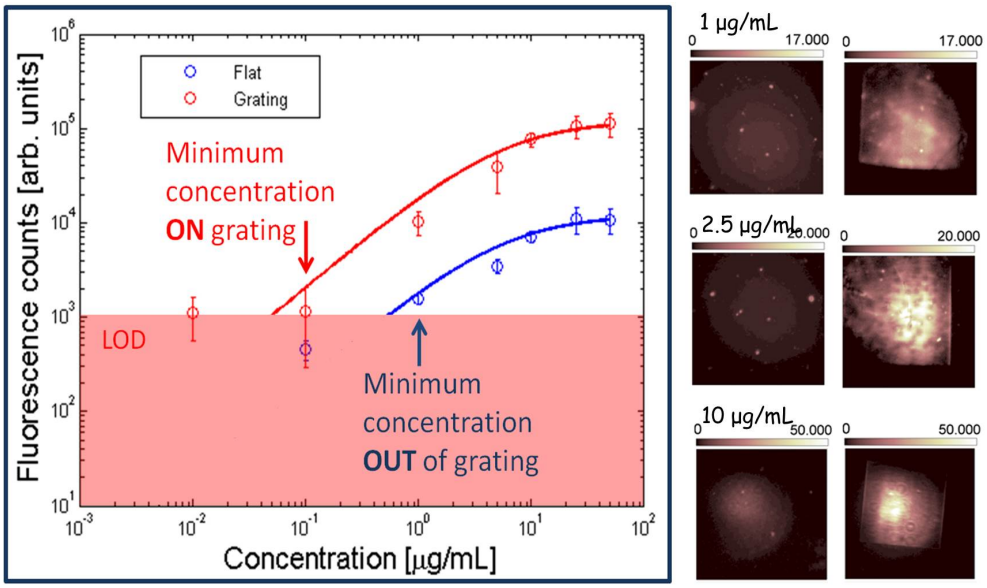

Figure 4.5: Titration curve measured on the patterned (red) and flat (blue) surface of the 1DPC for different concentrations of ptA Alexa. In the insets, exemplary fluorescence images of the flat and patterned areas at different conecentrations.

background is determined and fixed (as indicated in figure 4.4), we find that the lowest detectable concentration of PtA on gratings is one order of magnitude lower than the minimum concentration detectable out of gratings, on the flat 1DPC surface.

Chapter 5

Concentric ring antennae

In this chapter, I will focus on the directional extraction of fluorescence from localized sources. In the previous section, it has been shown that a patterned area can efficiently enhance the fluorescent signal coming from sources dispersed on that area. Such system works efficiently only for fluorescence radiated in a specific direction in the plane of the 1DPC surface, while for the direction orthogonal to the grating vector no diffraction occurs. When a small area containing randomly oriented fluorophores is considered, we can approximate it to a single point emitting in all directions, meaning that BSW-CF will radially propagate from the source in the surface plane. By taking inspiration from the plasmonic world, we found that a bidimensionally collimated beam con be obtained when a scattering center, such as a subwavelength hole, is surrounded by a concentric ring grating.[40] Furthermore, in recent works it has been demonstrated that also spontaneous emission coming from a subwavelength volume can be efficiently beamed out in a bidimensionally collimated cone when emission is coupled to Surface Plasmons that are then diffracted by a circularly symmetric grating.[65,75,76] We therefore decided to apply the same approach to extract BSW-CF coming from localized sources.

5.1 Symmetric annular grating

The structure analyzed in the following, is the same discussed in the second chapter, where it was demonstrated to be an efficient tool to convert freely propagating radiation into a localized subwavelength spot on the surface. The structure that we are going to analyze is

the one schematically shown in fig. 5.1. Given the stack sequence described in the chapter 3, here we consider the "low leakage" layout, consisting of 22 layers, since we now want to emphasize the diffractive properties of the surface structure, as explained in the previous chapter. The circular grating is etched on the multilayer top layer in such a way that a ring pattern is arranged with a spatial period $\Lambda_g = 520nm$ around a flat inner spacer. The total thickness of the grating is about 100 nm. The grating vector is radially oriented with respect to the circular grating center, and has a module $G = 2\pi/\Lambda_g = 12.08\mu m^{-1}$ that is very close to the BSW wavevector in the wavelength range between 532 nm and 590 nm wavelength.

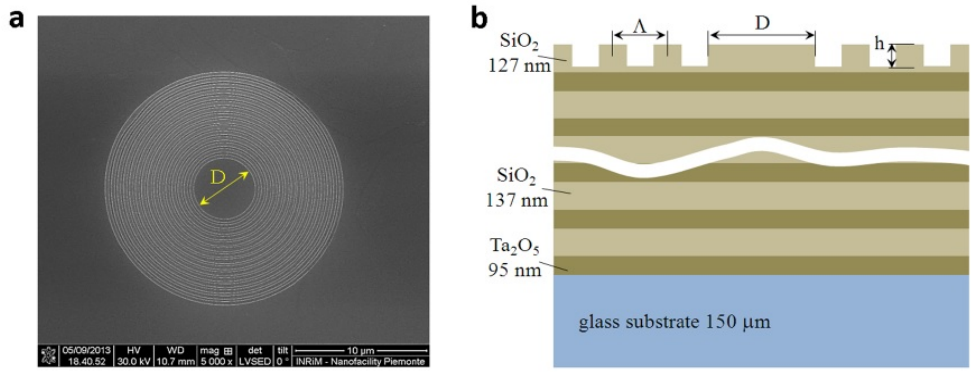

Figure 5.1: (a) SEM image of the concentric ring structure patterned on the surface of a 1DPC. The structure is etched in the last SiO_2 layer. (b) Schematic cross-sectional view of the diffractive structure engraved in the last layer of the photonic crystal.

The experimental setup employed in the following section is similar to the one described in the second chapter, and is reported in fig. 5.2 for clarity purpose. It allows for imaging the sample surface both on the air side and on the glass side with an oil immersion objective. Both wide field fluorescence microscopy and leakage radiation microscopy are therefore allowed.

5.1.1 Experimental results

In this section, we are interested in showing how fluorescence coming from localized sources can be efficiently beamed out by means of the diffractive structure described above. After covering the surface with an homogenous fluorescent layer of PtA Alexa (see previous chapter for the procedure), fluorescence is excited by a diffraction limited

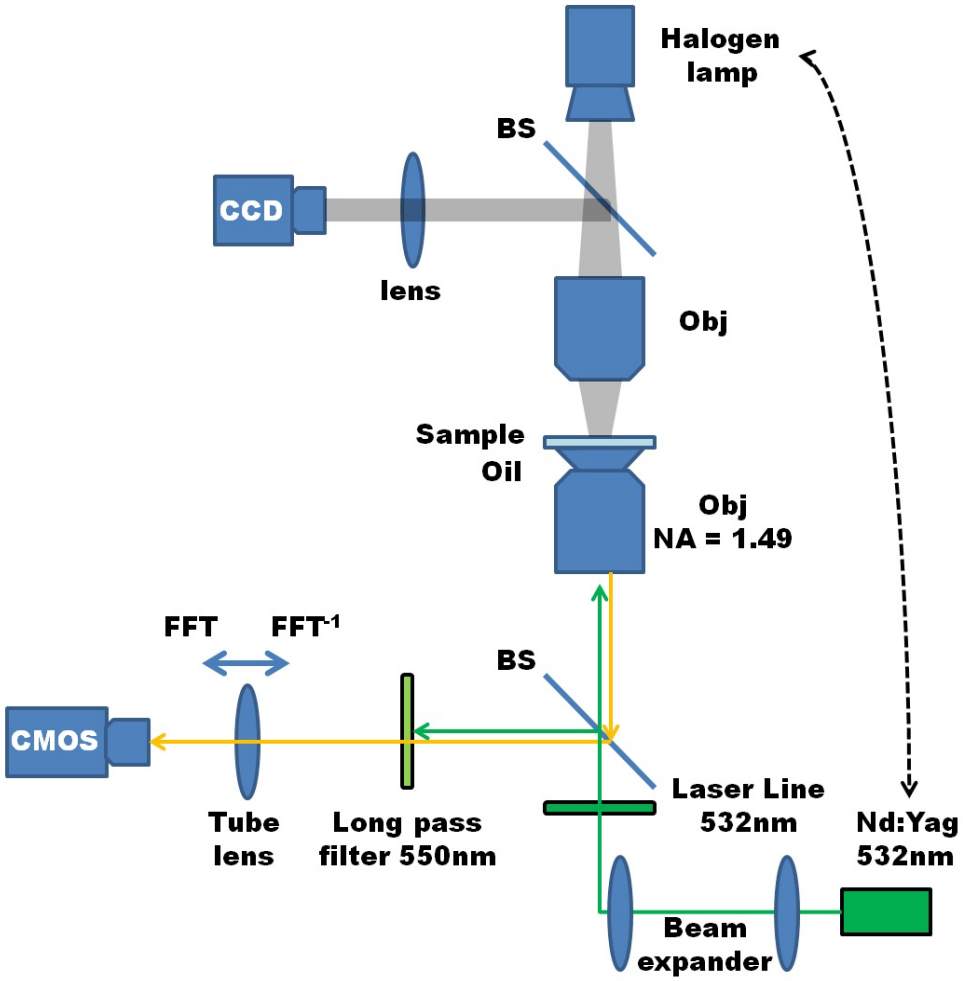

Figure 5.2: Customized fluorescence leakage radiation microscope with BFP imaging capabilities.

spot entirely contained inside the flat area (figure 5.3a). In this way we ensure that laser light does not couple with BSW and fluorescence is only excited inside the flat spacer.

Figure 5.3b shows a wide field fluorescence image of the sample surface collected with a 0.95 NA objective (Nikon 100x 0.95). The fluorescence image reveals a central bright spot from where fluorescence directly radiates in air. More interestingly, fluorescence is also detected in the area surrounding the region of direct excitation, with an intensity that is radially decreasing as we move away from the grating center. Such a distributed fluorescence is outcoupled in the substrate thanks to a mechanism of diffraction of BSW-coupled radiation.

We observe here evidence of the delocalization of collected fluorescence far away from the original location of the excited emitters. This effect has also been found for surface plasmons over a smaller length

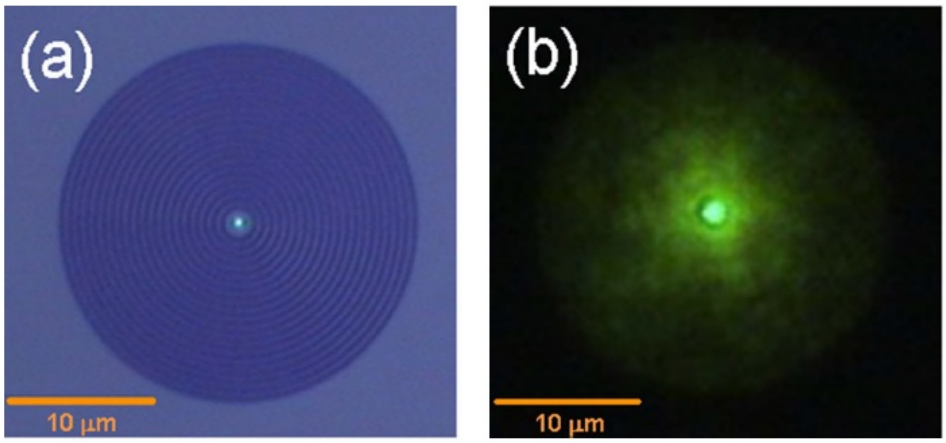

Figure 5.3: (a) Reflection bright-field image of a circular grating made through a top objective (NA = 0.95) and laser focusing in the central spacer; (b) direct plane image of fluorescence collected by the NA = 1.49 objective

scale, and critically considered in SPP-mediated imaging.[77,78]

Generally, surface modes can represent an efficient 'drain channel' for radiation leaking into the substrate. The use of the presented diffraction gratings can recover a significant portion of this surface mode-coupled fluorescence by outcoupling it normally to the 1DPC surface. As a result, an increase in the overall amount of collected fluorescence is obtained, as compared to the case wherein only the area of direct illumination is considered.

By looking at the BFP of the oil immersion objective, the beaming effect can be further understood. Fig. 5.4 allows for a direct comparison of the angular distribution of fluorescence excited on the flat surface (a) and inside a spacer surrounded by the concentric ring antenna (b). In figure 5.4a the observed bright rings correspond to fluorescence coupled to TE and TM modes of the multilayer and leaking into the glass substrate, as already discussed in chapter 3. Depending on the number of layers, the leakage radiation associated to the BSW-CF can be undetectable (as in fig. 5.4c.

When fluorescence is locally excited in the flat center of a grating spacer ($D = 2\mu m$, $\Lambda_g = 520nm$), a bright spot appears at $k_x/k_0 = 0, k_y/k_0 = 0$ in the corresponding BFP image. The bright spot is associated to fluorescence leaving the sample almost normally to the surface, with an estimated full divergence of less than 15 degrees.

Thanks to a mechanism analogous to some plasmonic systems,[79,80]

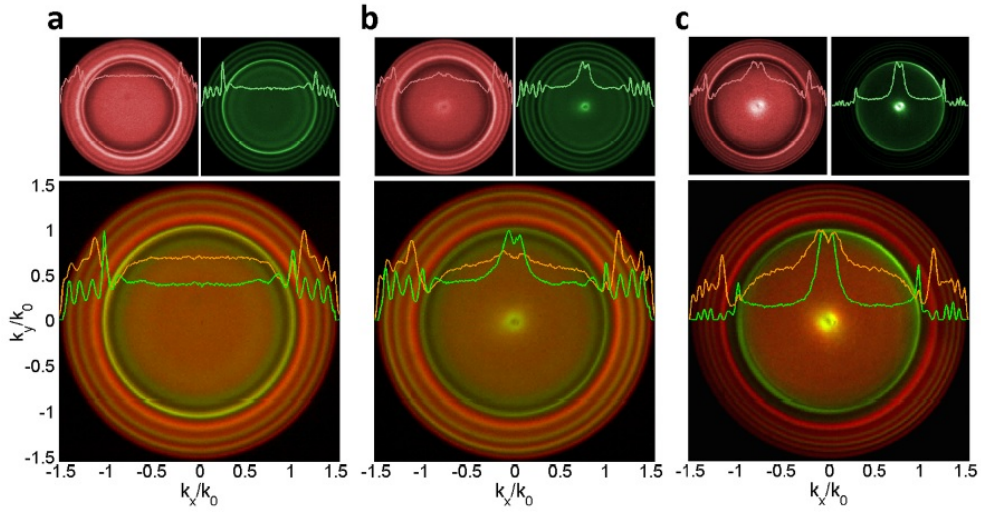

Figure 5.4: Back Focal Plane images for BSW-coupled fluorescence. (a) Fluorescence BFP images collected from a planar *regular* multilayer. (b) Fluorescence BFP collected from a circular grating ($D = 5\mu m, \Lambda_g = 520nm$) fabricated on *regular* multilayer. (c) Fluorescence BFP collected from a circular grating ($D = 5\mu m, \Lambda_g = 520nm$) fabricated on *low leakage* multilayer. Illumination is a laser beam focused onto the center of the inner spacer. For each colour image, the corresponding R-channel (red) and G-channel (green) images are separately shown in a row on top of the figure.

a portion of the energy emitted by the excited sources (characterized by randomly distributed dipolar momenta) is transferred to BSWs which in turn radially propagate away from the illuminated area. BSWs are then diffracted out of the multilayer by means of the circular grating, producing the observed beaming effect. In this respect, BSWs are mediating the transfer of energy from the localized sources to the free-space. The beaming effect can be largely improved if the circular grating is fabricated as an additive pattern on top of the last SiO_2 layer of the stack. By properly playing with the dielectric loading mechanism (producing a redshift of the BSW dispersion curve[81]) and the circular grating period, we managed to fabricate an additive polymeric grating that significantly increases the amount of beamed fluorescence in a given spectral range (figure 5.5).

As discussed, the beaming effect arises from diffraction of BSW-coupled fluorescence propagating radially from the grating center, where multiple sources are excited. No such an effect can be observed if the circular symmetry is broken (i.e. the excitation laser spot is off-center). In order to interpret the observed beaming in the BFP

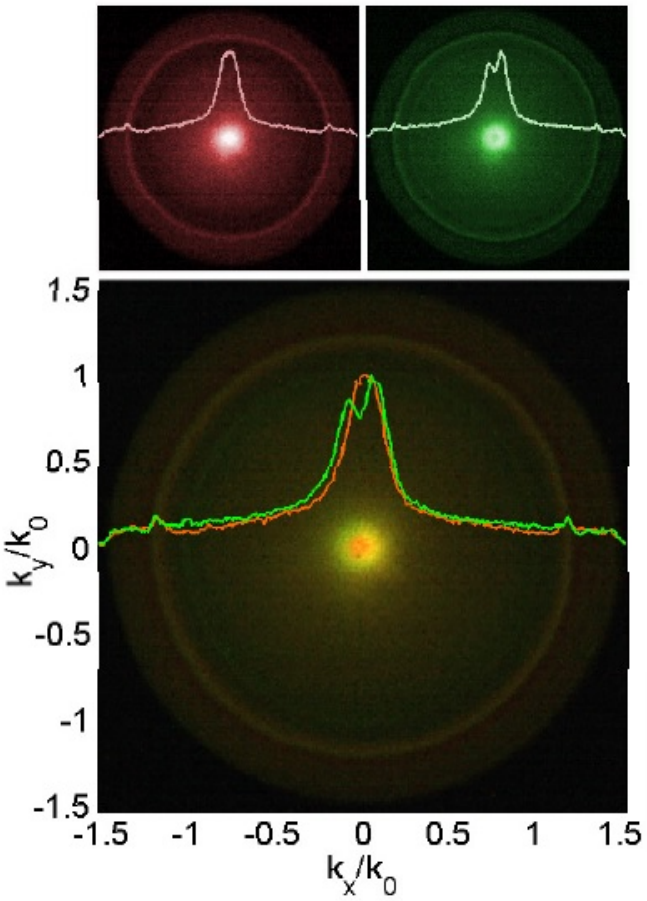

Figure 5.5: Back Focal Plane image showing the fluorescence collected upon local illumination of the flat inner spacer of the polymeric grating. The dielectric loading mechanism due to the deposition of the thin polymeric layer produces a redshift for the BSW dispersion such that a wider wavelength range of the dye emission spectrum can be BSW-coupled and then beamed. As a result, a more intense fluorescence beaming can be obtained over a larger spectral range.

images, the following geometrical model is proposed. The circular grating can be considered as composed by multiple wedges of locally linear gratings, radially oriented.

In a polar reference system centered in the spacer center, each wedge corresponds to a specific azimuthal angle. Assuming most of the radiated power as coupled to BSW, we can apply the Bragg's law to each wedge, taking the fluorescent BSW as the incident radiation. On the Fourier plane, fluorescence diffracted on the first order (+1) is distributed as a circular branch obtained by shifting the BSW-coupled fluorescence ring by an amount equal to the local grating vector mod-

ule[82] . The direction of such a displacement is radial, and oriented according to the azimuthal angle of the specific wedge considered. As a result, multiple first-order (+1) diffraction branches appear within the portion of the Fourier plane limited by the maximum NA of collection (NA = 1.49 in the present case). The superposition of all diffraction branches leads to the appearance of a circular caustic in the Fourier plane, i.e. a geometrical locus wherein the diffracted power from each wedge accumulates.

The size of the circular caustic depends on the grating vector $G = 2\pi/\Lambda_g$. When G equals the fluorescent BSW wavevector (for a given wavelength), the caustic collapses into a single accumulation point, thus leading to a normally diffracted beaming with almost zero divergence. This model is very well supported by experimental observations. Several gratings with different periods Λ_g have been fabricated and employed for BSW-assisted beaming. Results are shown in figure 5.6, together with the corresponding caustics calculated analytically on the Fourier plane.

When looking at the direct image of the 1DPC surface, we observe that the fluorescence beaming effect involves a diffraction mechanism occurring on the whole surface of the grating. BSW-coupled fluorescence can propagate radially from the sources excited in the inner spacer by the focused laser. Thanks to the low losses, BSW can propagates for long distances, and undergo diffraction by the grating figure 5.8a. The collection optics used here has a low NA to prevent the contribution of substrate-leaking BSW-coupled fluorescence to the image. The measured intensity profile along a horizontal cross section shows a central maximum surrounded by a pair of symmetric, decreasing lobes.

The directionality of the fluorescence extracted is confirmed by the image in figure 5.7. Here, the same concentric gratings discussed in figure 5.6 are excited with a collimated laser beam and fluorescence is collected with a low numerical aperture (NA = 0.2) from the air side. As can be seen, the grating with smaller period ($\Lambda_g = 440nm$, indicated with a white arrow) is not visible, since fluorescence is outcoupled at an angle larger than the numerical aperture of the collection objective.

While the lobes are due to a BSW-assisted diffraction effect only, the intensity from the central peak is also due to fluorescence that is di-

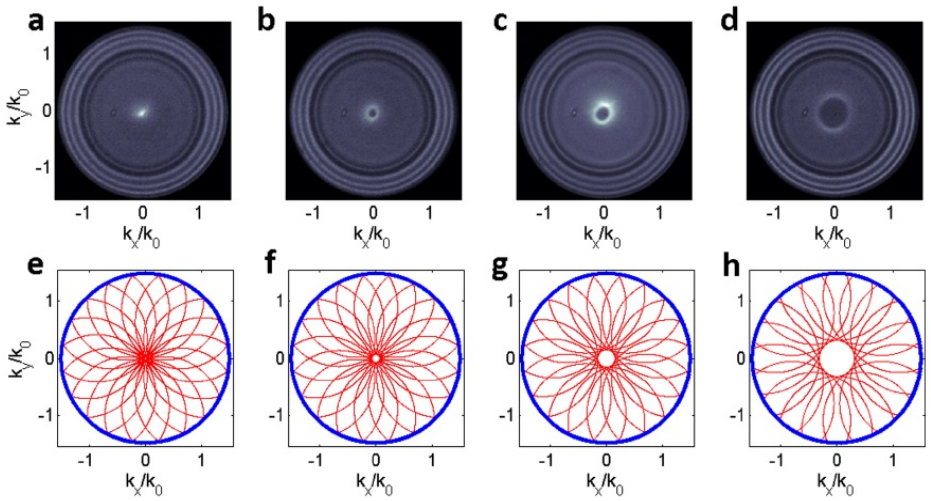

Figure 5.6: Different BFP images of circular gratings on *regular* multilayers are compared to corresponding schematic BFP patterns calculated by a simple geometrical model. All measured BFPs are obtained by locally exciting multiple fluorescent emitters in the center of several circular gratings ($D = 5\mu m$) with different periods Λ_g. The corresponding calculated patterns are obtained by applying the Bragg law to the BSW-coupled fluorescence ring as diffracted by multiple wedges of the circular grating. For each wedge, a circular branch associated to the first order diffracted BSW is drawn. The superposition of all those diffraction branches produces a caustic circle whereon all the diffracted intensities sum up. The diameter of the caustic circle depends on the grating period Λ_g and indicates the angular shape of the diffracted fluorescence out of the multilayer surface. When the caustic circle collapses into a single point, the BSW-coupled fluorescence is almost completely beamed normally to the sample surface, with low divergence. (a), (e), grating period $\Lambda_g = 560nm$. (b), (f), grating period $\Lambda_g = 520nm$. (c), (g), grating period $\Lambda_g = 500nm$. (d), (h), grating period $\Lambda_g = 440nm$.

rectly emitted in the free-space without any coupling to 1DPC modes figure 5.8b). In particular, the lobe intensity drops quickly at the outer boundary of the circular grating, where no any further diffraction occurs. During the propagation across the grating, the BSW-coupled fluorescence undergoes losses mainly due to leakage and diffraction, and the observed fluorescence intensity becomes weaker and weaker as the grating outer boundaries are approached. The plurality of sources excited by the focused laser have randomly oriented dipolar momentum, therefore the coupling to BSW can occur over all radial directions. However, the BSW are TE-polarized and this polarization state can

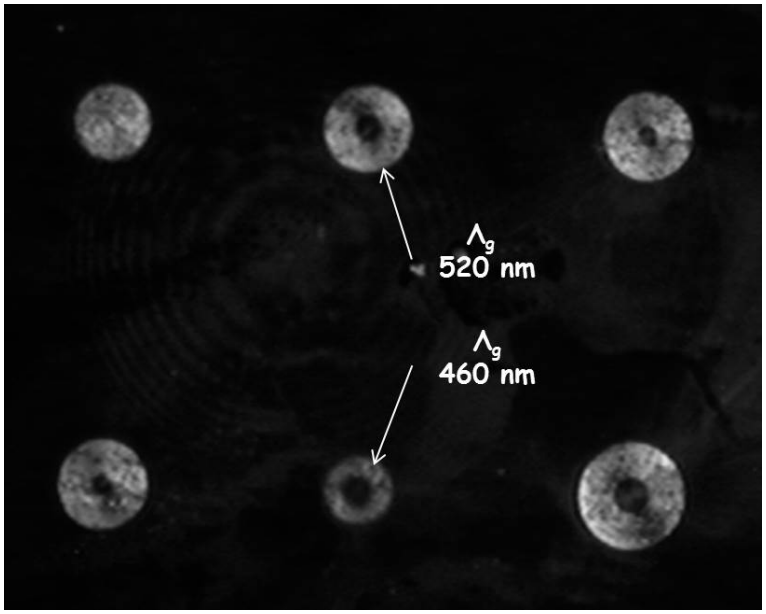

Figure 5.7: Wide field fluorescence image of the surface of the 1DPC patterned with six circular gratings having different periods the same periods discussed in figure 5.6. The white arrows indicate two gratings with periods $\Lambda_g = 520 and 460 nm$ resectiveluy. The different fluorescence intensity is due to the different output angle of beamed fluorescence. The second one has indeed an output angle out of the NA of the collection objective.

be directly observed in the beamed fluorescence as well. Specifically, the diffracted fluorescence possesses an inhomogeneous polarization distribution depending on the azimuthal position of the local grating region it comes from. By inserting a polarization analyser along the collection path, the image in figure 5.8a is polarization filtered according to the analyser angular position, as shown in fig. 5.8c-e. This result confirms the BSW-assisted characteristics of the beamed fluorescence. It should be recalled now that most of the fluorescence intensity observed in figure 5.8 is directed almost normally to the 1DPC surface, leading to a BSW-assisted radiation extraction mechanism somehow complementary to the BSW focusing shown in chapter 2.

5.1.2 Experimental quantification of the extraction enhancement factor

Results shown above suggest that the collection of fluorescence at low NA would be significantly improved thanks to the BSW-assisted beaming effect. In this section we attempt a quantitative estimation

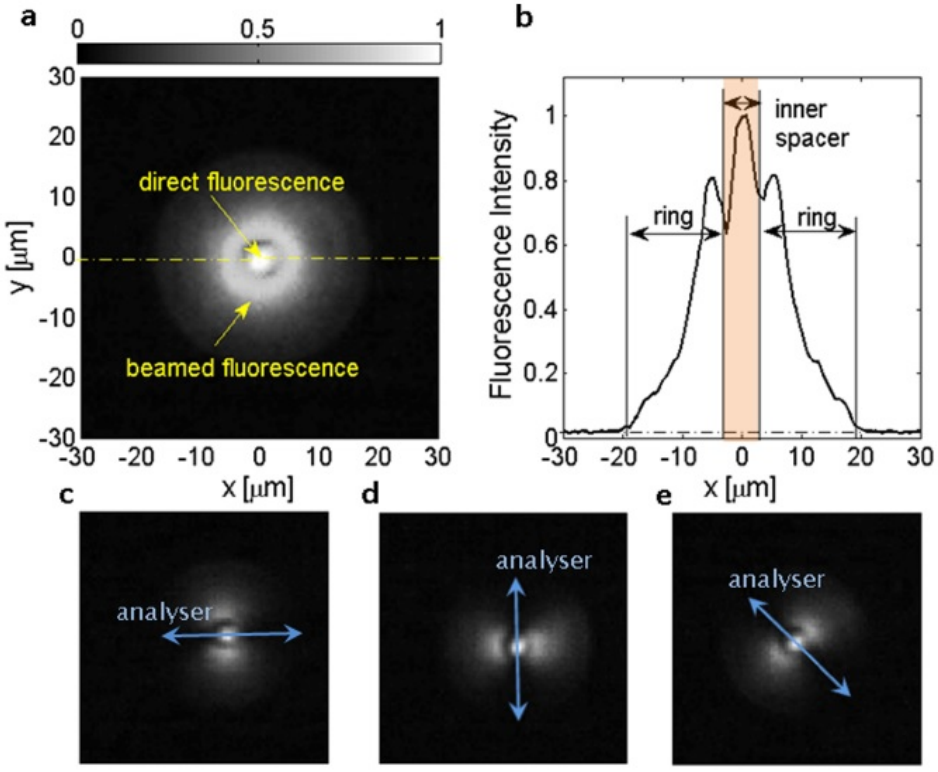

Figure 5.8: (a), direct image of fluorescence excited by a laser beam focused onto the flat inner spacer of a circular grating ($D = 5\mu m, \Lambda_g = 520nm$) fabricated on *low leakage* multilayer. (b), cross-sectional fluorescence intensity along the horizontal dashed line in (a). (c), (d), (e), same as in (a) with the addition of a polarization analyser in collection, whose orientation is sketched by the arrows in the figures.

of the fluorescence collection improvement.

In order to quantify the enhancement in fluorescence collection, we setup an original scanning microscope as illustrated in figure 5.9. This setup is aimed at performing a spectral analysis of light emitted from the sample surface with both spatial, angular and spectral resolution. The sample is scanned through a focused laser beam ($\lambda = 532nm$) emerging from an oil immersion objective (NA = 1.49). The leakage radiation is collected by means of the same objective and then passed through an edge filter (RazorEdgeH Longpass 532) to filter out the laser radiation. A tube lens produces a magnified BFP image of the collection objective onto a remote plane, wherein a multimode fiber end is located. The fiber end is supported by a two-dimensional translational stage, and can be accurately moved onto the BFP image plane. The fiber collects fluorescence from specific portions on

the BFP image and delivers the collected radiation to a spectrometer (Acton SpectraPro 300, Princeton Instruments).

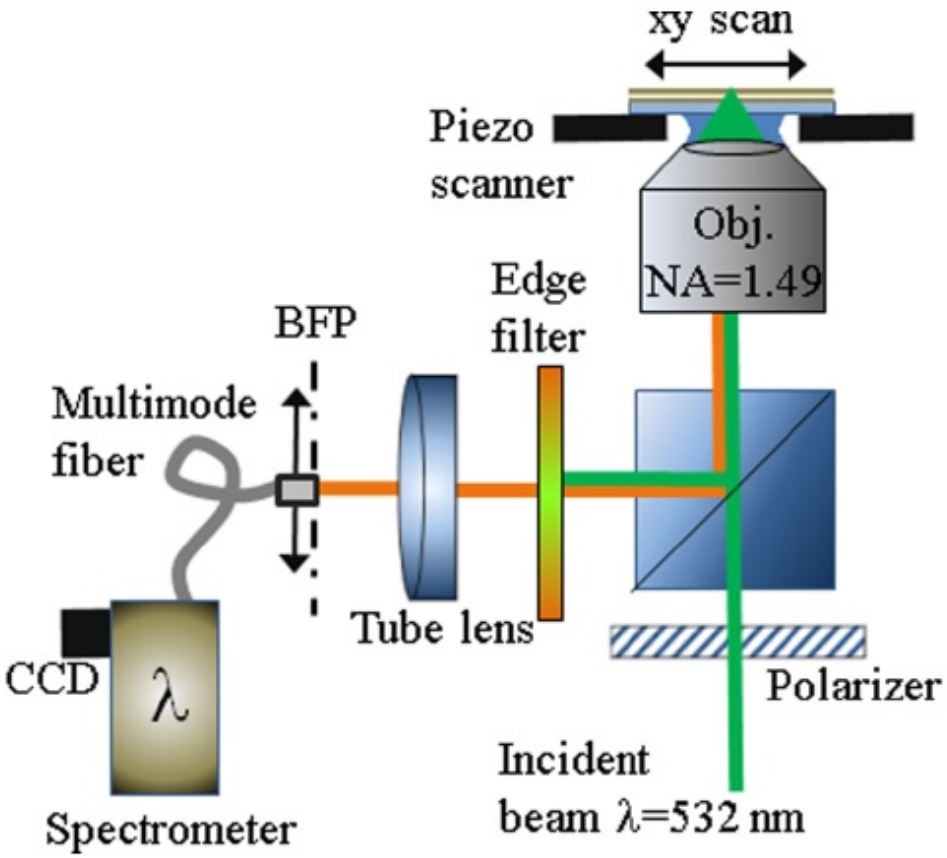

Figure 5.9: Schematic view of the BFP scanning fluorescence microscope.The sample is scanned through a focused laser beam that locally excites fluorescence. Illumination is done by means of an oil immersion objective (NA = 1.49). The radiation leaking into the substrate is collected by the same objective and spectrally filtered for having only fluorescence reaching the detector. A tube lens produces a magnified BFP image over a remote plane where a collection fiber (core diameter $50\mu m$) can be accurately positioned. The fiber is moveable along two directions, in such a way that light can be fiber collected from selected regions of the BFP image. Collected light is sent to a spectrometer equipped with a CCD camera. As an example, when the fiber is placed in the very center of the BFP image, only light propagating normally with respect to the sample surface ($k_x = 0, k_y = 0$) is collected and spectrally analysed. Since the illumination is focused, it is therefore possible to obtain spatially resolved spectral information about the fluorescence leaving the sample along specific directions of propagation.

Since the angular resolution achievable with such a system is inversely proportional to the lateral dimension of the collection fiber core, we found a tradeoff between fiber diameter, BFP magnification factor and signal-to-noise ratio of fluorescence spectra as measured by the spectrometer CCD. In a suitable configuration, the fiber diameter is completely contained within a region of NA < 0.1 on the BFP image plane. During the scan, fluorescence is locally excited by the focused laser spot. For each scan position, the fluorescence spectrum can be recorded, according to the specific propagation direction as determined by positioning the collection fiber onto the BFP image. The presented measurement consists of an array of 150 x 150 pixels, with an integration time of 5 ms for each pixel. The laser illumination is kept at low power to avoid rapid photobleaching of the emission during the scan. In the next, we present experimental results wherein the collection fiber collects fluorescence from a circular region centered at $k_x/k_0 = k_y/k_0 = 0$ on the BFP and corresponding to a NA < 0.1.

The false-color image in figure 5.10a is related to the collected fluorescence from a scan area containing the circular grating. Intensity values are integrated over a wavelength range from $\lambda = 570nm$ to $\lambda = 595nm$, after background subtraction. A significant increase of fluorescence is observed corresponding to the grating inner spacer, while the grating itself shows a faint fluorescence as compared to the background. This means that the BSW-assisted beaming effect improves the collection of fluorescence at NA < 0.1 only when the focused laser illuminates the spacer center, contrary to the case wherein the laser is focused elsewhere.

In figure 5.10b, the emission spectrum from the inner spacer (integration over the black square in figure 5.10a) is compared to the emission spectrum from a region outside the structure (integration over the green square on top right corner in figure 5.10a). In order to quantify a collection enhancement factor due to the beaming effect, several spectral ranges are considered, as sketched in the figure 5.10b. For each spectral range, the ratio $I_{spacer}/I_{outside}$ is calculated, wherein I_{spacer} and $I_{outside}$ refer to the fluorescence intensities integrated over the corresponding spectral range and over spatial regions defined by the black box and the green box in figure 5.10a, respectively. A set of values for the ratio $I_{spacer}/I_{outside}$ is obtained by making the green box sequentially sampling the whole image, with the exclusion of the

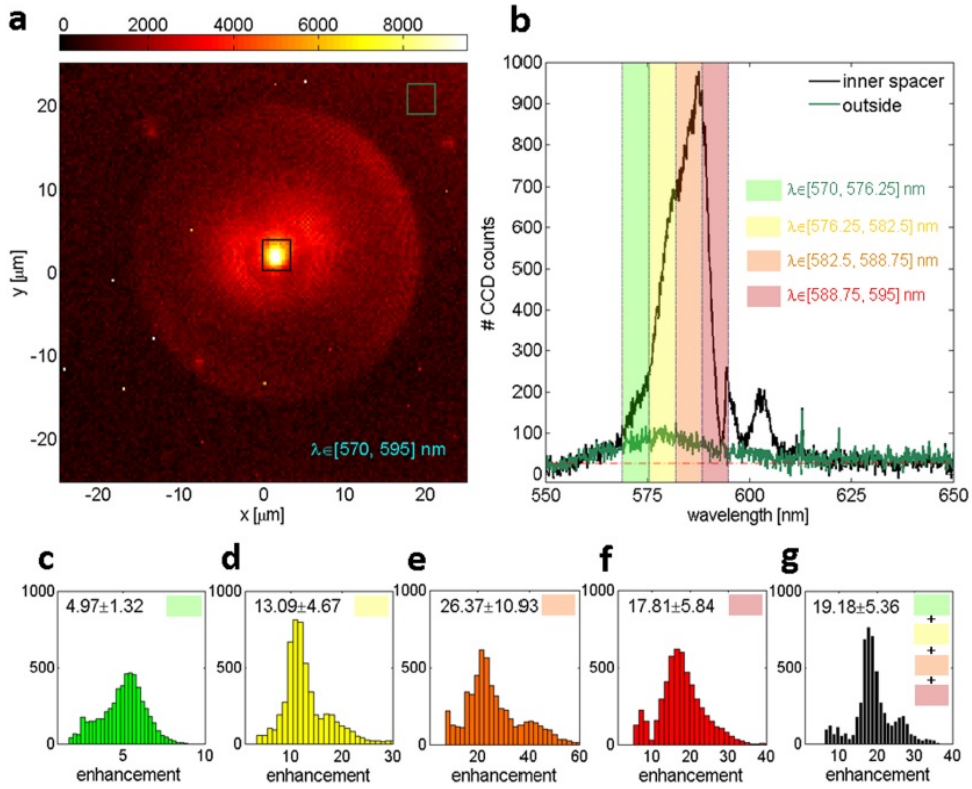

Figure 5.10: (a) False-color image of the circular grating as obtained by means of the BFP scanning system. Intensity values are integrated over a spectral range from $\lambda = 570nm$ to $\lambda = 595nm$. (b) Fluorescence spectra corresponding to the grating inner spacer and outside the grating. Coloured bars indicate spectral intervals used for further analysis. (c-g) statistical distributions of the enhancement factor calculated over the corresponding spectral ranges. Average and standard deviation are indicated for each spectral range.

grating area.

Finally, the collected data set for each spectral range are represented as histograms, as shown in figure 5.10c-g. Each histogram provides information about the statistical distribution of the enhancement factor, clearly wavelength-dependent. For example, the highest enhancement factor is estimated as 26.37 ± 10.93 and it is observed for wavelengths between $\lambda = 582.5nm$ and $\lambda = 588.75nm$ (5.10e). If the total wavelength range from $\lambda = 570nm$ to $\lambda = 595nm$ is considered, the enhancement factor is estimated as 19.18 ± 5.36 (figure 5.10g).

5.2 Off-axis beaming from localized sources

In many applications such as optical sensing or lighting wherein ensembles of emitters randomly oriented radiate light almost isotropically, it may be desirable to take advantage of a suitably designed emission directivity.

In the previous section we demonstrated the use BSW to beam radiative energy from localized sources to free-space radiation. Here we introduce an anisotropic pattern on a 1DPC surface to beam fluorescence out of the structure at an arbitrary direction. In a recent paper, Zhan et al. used a plasmonic spiral antenna for obtaining an off-normal beaming of the fluorescence excited out of the center of symmetry of the structure [ref 22 ACS]. In the present case, we managed to obtain and fabricate a quasi-concentric, locally periodic circular grating diffracting BSW-coupled fluorescence thanks to the design approach based on caustics curves in the Fourier plane described above.

Such a circular grating is anisotropic, as it shows a spatial periodicity varying with an azimuthal dependency. In recently published works, an off-axis beam has been obtained by diffracting surface plasmons locally coupled through the use of nanoslits with a pair of linear gratings having different periods.[65,83]

5.2.1 One dimensionally collimated off-axis beam: FEM model

In order to check the validity of this approach on a BSW-based system, we modified the two-dimensional computational FEM model defined in the third chapter by adding a pair of additive linear gratings located on the two sides on the emitter. Gratings can be made of any low-absorbing dielectric material, including polymers. The emitter is introduced in the form of a line of current (figure 5.11a). The line of current is oriented along the y-axis and emits a TE-polarized radiation that can couple to BSWs. The emitted spectrum ranges from 550 to 600 nm in wavelength.

The period of the gratings is chosen in such a way that diffracted BSWs in the glass substrate superpose at an angle $\theta_{beam} = 10°$ with respect to the normal surface. In a first approximation, this effect can be described by applying the diffraction Bragg's law (at the first-order)

for the two gratings, as described by the following equations:

$$G_1 = k_{BSW} - k_0 n_s \sin(\theta_{beam}) \tag{5.1}$$

$$G_2 = k_{BSW} + k_0 n_s \sin(\theta_{beam}) \tag{5.2}$$

where $G_{1,2} = 2\pi/\Lambda_g^{1,2}$ are the grating vectors for the two gratings with periods Λ_g^1 and Λ_g^2 , respectively, k_{BSW} is the BSW wavevector component parallel to the 1DPC surface, n_s is the refractive index of the glass substrate, and $k_0 = 2\pi/\lambda$ is the wavenumber of the radiation emitted in vacuum at a given wavelength λ. As an example, by setting $\theta_{beam} = 10°$, the periods Λ_g^1 and Λ_g^2 can be calculated from equations 5.1 and 5.2 for a specific wavelength. However, the presence of a grating itself produces a slight increase of k_{BSW} as compared to the case of a bare 1DPC surface, depending on the grating height (because of the dielectric-loading red-shift discussed in the secodn chapter), and an iterative optimization should be performed in order to find the most suitable grating parameters by taking into account the effective k_{BSW}.

We optimized the beaming effect for $\lambda = 570nm$, resulting in grating periods $\Lambda_g^1 = 670nm$ and $\Lambda_g^2 = 415nm$. Provided that such a model works in a single direction only, it is indeed possible to observe a BSW-mediated diffraction similar to the plasmonic case. Figure 5.11b shows the calculated near- field intensity distribution of the electromagnetic field emitted by the source. It is worth underlining how the coupling of the electromagnetic field to BSW can be easily appreciated close to the emitter. The BSW-coupled radiation propagates along the surface and gets diffracted by the two gratings. On a wider spatial scale (figure 5.11c), the combined diffraction by the grating pair results in two tilted beams propagating in air and in glass, respectively, with the last one having a suitable propagation angle. When the far- field intensity angular pattern is considered, a clear beaming of the power radiated by the source can be observed, with very low divergence $\Delta\theta_{beam} \approx 1.1°$ in glass and $\Delta\theta_{beam} \approx 1.7°$ in air (figure 5.11d). The two beams propagating in air and in glass bring 33% and 12% of the total power emitted by the source, respectively. In particular, considering only the emission within the glass substrate, the BSW-assisted beam corresponds to 67% of the emitted power.

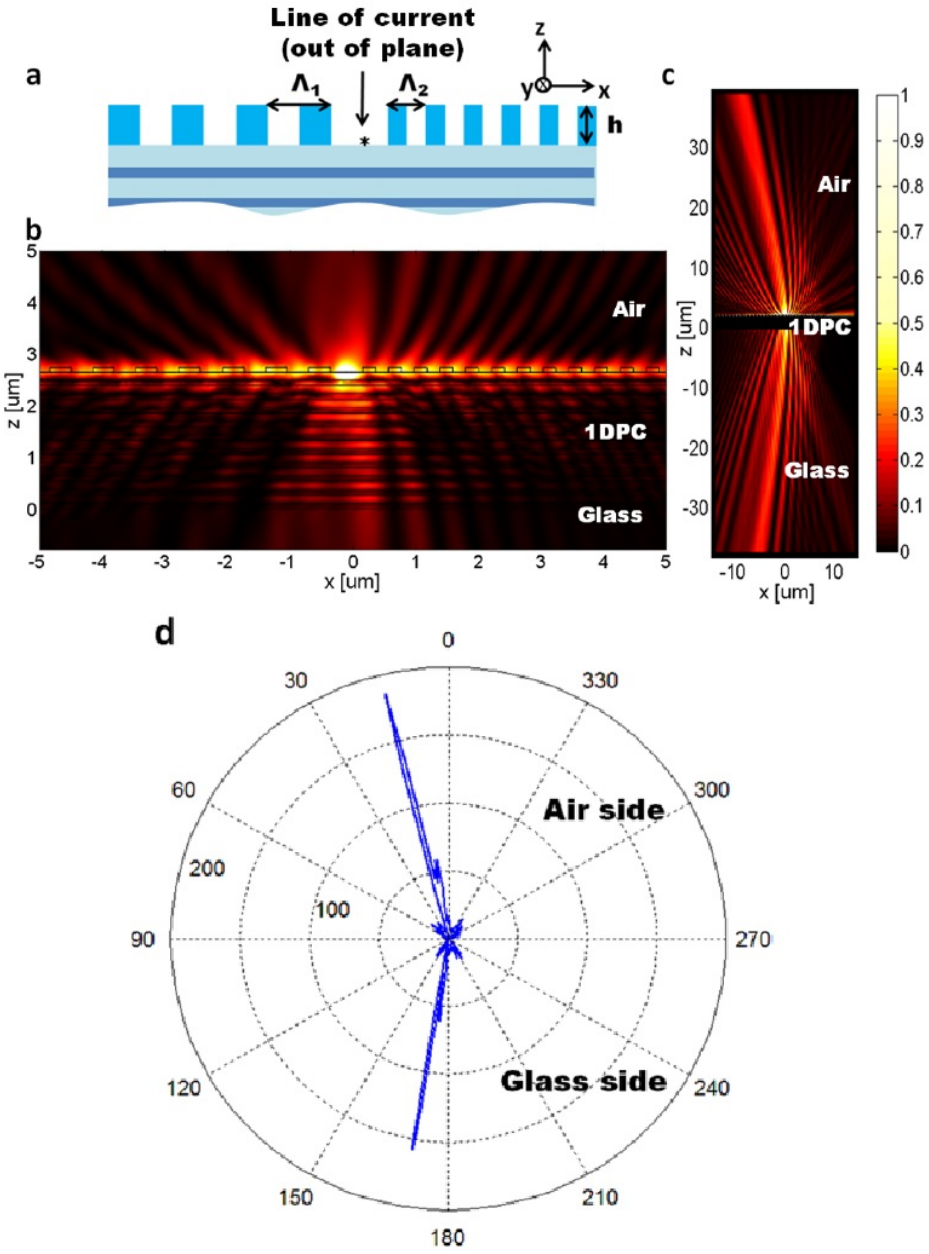

Figure 5.11: (a) Schematic view of the surface grating with a pair of linear gratings having height h = 80 nm and spatial period $\Lambda_g^1 = 670nm$ and $\Lambda_g^2 = 415nm$, respectively. An emitting source as a line of current is located on a flat area sandwiched between the two gratings, oriented normally to the cross-section plane, along the y direction. (b) Calculated intensity distribution of the electromagnetic field ($\lambda = 570nm$) emitted by the source. (c) The same as in (b) over a wider spatial range. (d) Calculated far-field radiation pattern.

5.2.2 Bidimensionally collimated off-axis beam: Experimental results

When extending the working principle above-described to a three-dimensional scenario, a circularly symmetric diffractive structure can

be considered. In the section above, we experimentally demonstrated that BSW-coupled fluorescence can be efficiently beamed by means of surface corrugations periodically arranged around the feeding source. However, the tilting of the BSW-assisted beam requires some loss of symmetry in the diffractive structure.[84]

Here we propose an anisotropic circular grating with a spatially varying periodicity. More specifically, we consider a diffractive circular structure with a grating period that is varying azimuthally. Such a grating can be obtained from a local application of the Bragg's law to a corresponding diffraction pattern defined over the Fourier plane.

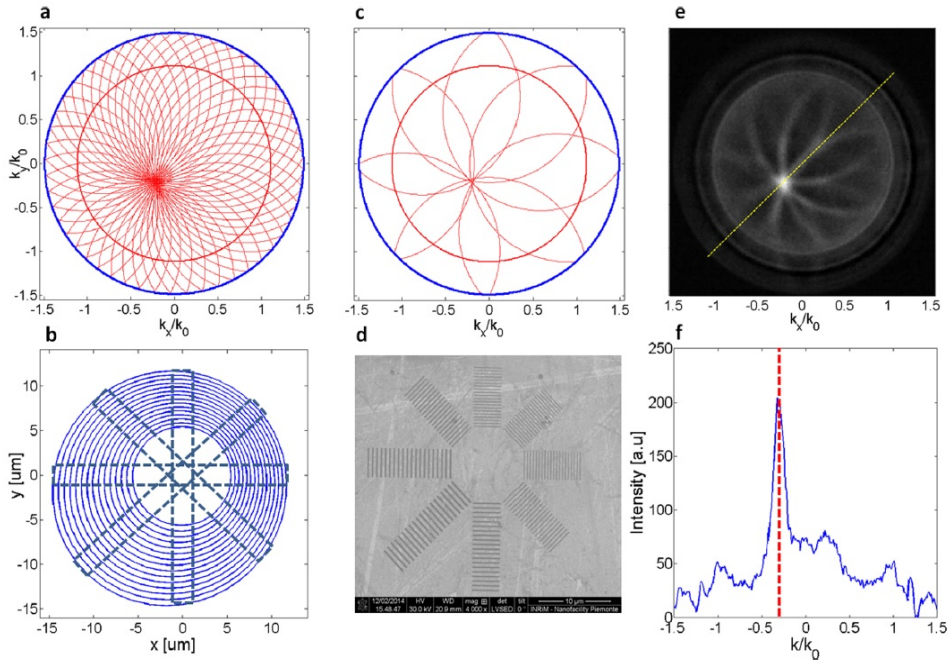

Figure 5.12: (a) Calculated diffraction pattern in the Fourier plane produced by a circular grating described by $\vec{G}(\phi) = G_0(1-0.28sin(\phi+\pi/4))\cdot\vec{u_r}$, where $G_0 = k_{BSW}$ and ϕ is considered counterclockwise from the x-axis.The outer blue circle indicates the maximum NA of observation, while the inner red, thick circle is the BSW ring at $\lambda = 570nm$. (b) Ideal anisotropic circular grating associated with the pattern in (a). The dashed boxes indicate the region of discretization for the real structure. (c) BSW diffraction pattern in the Fourier plane produced by a subset of eight linear gratings extracted from (b). (d) SEM image of a real grating obtained from the discretization in (b). (c) Measured back focal plane showing diffracted BSW-assisted fluorescence. (f) Fluorescence intensity profile cross-section along the yellow dashed line in (e).

In a Fourier plane defined by the axis k_x/k_0 and k_y/k_0 , where

k_x and k_y are the x- and y-components of the transverse wavevector parallel to the 1DPC surface, we consider a circular region within the light line in glass, i.e., $\sqrt{(k_x/k_0)^2 + (k_y/k_0)^2} \leq 1.49$ (outer blue line in figure 5.12a. This portion of the Fourier plane represents the angular range of collection in an eventual microscope-based system and can be directly imaged in a leakage radiation setup with back focal plane imaging capabilities (see the experimental setup in fig. 3.3).

At a specific wavelength, the BSW on the planar 1DPC can be represented on the Fourier plane as a ring having radius:[32]

$$\sqrt{(k_x/k_0)^2 + (k_y/k_0)^2} = k_{BSW}(\lambda)/k_0 \tag{5.3}$$

When a grating is added onto the 1DPC surface, the BSW gets diffracted accordingly. In the Fourier plane, a replica of the BSW ring is produced as shifted from its central position $k_x/k_0 = k_y/k_0 = 0$ by a length proportional to the grating vector.[85]

The direction of such a displacement is parallel to the grating vector. In the case of a circular grating with a spatial period varying with the azimuthal angle ϕ, a resulting grating $G(\phi) \cdot \vec{u_r}$ is obtained, where $\vec{u_r}$ is the unitary radial vector in the Fourier plane. Therefore, a plurality of diffracted BSW rings will be obtained by radially shifting the BSW ring by a length $G(\phi)$ as multiple azimuthal directions from $\phi = 0$ to $\phi = 2\pi$ are considered.

The function $G(\phi)$ can be designed in such a way that most of the diffracted BSW rings superpose each other over a small region in the Fourier plane, eventually not centered at $k_x/k_0 = k_y/k_0 = 0$, thus leading to a beaming effect. In the following, we apply this mechanism to a specific case, whose results are summarized in figure 5.12. As for linear gratings, however, the effective k_{BSW} of a BSW subjected to diffraction is slightly increased as compared to the BSW on a bare 1DPC because of a dielectric loading effect caused by the additional layer including the grating.

We consider a $\lambda = 570nm$ BSW propagating on a 1DPC coated with a polymeric additional layer 40 nm thick. The corresponding BSW wavevector is calculated as $k_{BSW}/k_0 \approx 1.115$, and it is represented by the thick red circle in figure 5.12a. The thickness of the polymeric layer used for estimating k_{BSW}/k_0 is chosen to be one-half the thickness of the final grating that will be fabricated on the 1DPC

(because the grating has a fill factor of 0.5).

An anisotropic circular grating defined by

$$\vec{G}(\phi) = G_0(1 - 0.28\sin(\phi + \pi/4)) \cdot \vec{u}_r \tag{5.4}$$

diffracts BSW in such a way that most of the diffracted first-orders superpose in a small region at $k_{beam}/k_0 = 0.3$, where k_{beam} is the transverse wavevector component of the out-coupled radiation beamed. The beaming angle corresponds to an angular tilt of about 11.5° with respect to the surface normal, in the glass substrate. The grating structure producing the diffraction pattern in figure 5.12a can be obtained by sequentially applying the Bragg's law on a set of local linear gratings radially oriented, each of them associated with a specific azimuthal angle ϕ.

The result is shown in figure 5.12b, wherein the corrugations surround a wide flat central area with a diameter of $10\mu m$. The grating structure depicted in figure 5.12b may be difficult to fabricate. Therefore, we reduced the complexity by discretizing the circular structure along four specific directions, namely, horizontal, vertical, and two diagonals tilted at 45° (as indicated by the dashed boxes in figure 5.12b). In addition, the corresponding diffraction branches are further optimized in such a way that they are intersecting onto a single point in the Fourier space (figure 5.12c). As a result, eight gratings oriented along the four directions defined above are obtained.

Fabrication is performed by electron beam lithography (EBL), using a negative tone resist with a thickness of about 100 nm. The final structure is shown in the scanning electron microscope (SEM) image in figure 5.12d.

In order to investigate the coupling of localized emitters with the photonic structure, an homogenous layer of PtA Alexa 546 has been spun over the 1DPC surface, in the same way described above. The leakage radiation microscope sketched in figure 3.3 has been employed to experimentally observe the beaming effect.

The experimental result is shown in figure 5.12e and can be directly compared to figure 5.12c as expected from our model calculation. We indeed observe that all the diffracted branches superpose in the bright point out of the center of the BFP, meaning that an effective beaming effect has been obtained off-normal. An intensity profile (figure

5.12f) plotted along the yellow dashed line in figure 5.12d exhibits a main peak centered at $k_{beam}/k_0 = 0.3$, corresponding to the suitable output angle of about 11.5° in glass. The width of the beam is larger than expected because of the broadband emission of the fluorescent dye. In fact, the grating has been optimized for $\lambda = 570nm$, while AlexaFluor 546 has an emission spectrum ranging from 550 to 620 nm in wavelength.

However, despite the broad spectrum of fluorescence involved, the beaming effect still shows a rather low angular divergence, estimated as $\Delta\theta_{beam} \approx 8°$ (full width at half-maximum of the BFP peak) from the BFP image.

Conclusions

In this thesis, I've shown that one dimensional photonic crystals can act as a suitable platform for 2D optics, and that Bloch Surface Waves can act as energy mediators between far field radiation and localized near-field radiation. Far field radiation can be coupled to BSW in different ways, by coupling the 1DPC with a prism or by using surface couplers.

The low absorption of dielectric materials allows for designing structures able to sustain surface waves that can propagate for several hundreds of microns in the visible range. Along the path, BSW can be eventually manipulated by means of ultrathin dielectric structures directly patterned on the surface of the 1DPC by standard lithographic techniques. Alternatively, freely propagating radiation can be converted into BSW by exploiting surface couplers that can eventually be focused in a subwavelength volume when a concentric ring grating is considered.

In the second part of the thesis, the influence of the photonic resonant structure on spontaneous emission has been considered. Due to the highly enhanced density of photonic states occurring at the truncation interface of the one dimensional photonic crystal, spontaneous emission is strongly modified. The resonant mode acts indeed as a preferential drain channel for electromagnetic energy, that is therefore radiated with the specific wave-vector given by the BSW dispersion relation. Along the propagation at the truncation interface, part of the energy leaks into the substrate preserving the transverse wave-vector component. The radiation pattern in far-field results in a highly collimated and dispersed beam.

Once the radiation is coupled with the BSW, it can be manipulated

by means of surface structures, similarly to what happens with Surface Plasmon Coupled Emission.

An interesting chance is to convert the BSW-coupled fluorescence into a highly collimated beam that can be out-coupled along any desired direction by employing surface diffractive gratings and simply applying the Bragg's law. In particular, the case wherein a localized source is surrounded by a bull's eye antenna allows to maximize the directional extraction. The overall effect in far-field is that the spontaneous emission of a point-like source is converted from an almost isotropic pattern into a highly bi-dimensionally collimated beam.

The photonic structure discussed in this work can be an interesting resonant substrate for 2D light manipulation since offers some advantages with respect to typical photonic crystal structures and to metallic films. Moreover, due to the strong influence over the spontaneous emission occurring close to the surface, it is a suitable platform for applications such as few molecules fluorescence sensing, efficient single photon extraction or, eventually, surface enhanced raman scattering, since it can be easily integrated with plasmonic nanoantennas.

Appendix A

List Of Publications

[1] S. Ricciardi, F. Frascella, A. Angelini, A. Lamberti, P. Munzert, L. Boarino, R. Rizzo, A. Tommasi, and E. Descrovi, emphSurface wave-coupled emission made easy for fluorescence biosensing on chip, Sens. and Act. B, Accepted.

[2] A. Lamberti, A. Virga, A. Angelini, A. Ricci, E. Descrovi, M. Cocuzza, F. Giorgis, Metal-elastomer nanostructures for tunable SERS and easy microfluidic integration, RSC Adv. 5(6), 4404-4410, 2015.

[3] A. Lamberti, A. Angelini, S. Ricciardi, F. Frascella, A flow-through holed PDMS membrane as a reusable microarray spotter for biomedical assays, Lab on a Chip, Adv. Article (2015).

[4] A. Angelini, A. Lamberti, S. Ricciardi, F. Frascella, P. Munzert, N. De Leo, E. Descrovi, In-plane 2D focusing of surface waves by ultrathin refractive structures, Optics Letters, 39(22), 6391-94 (2014).

[5] M. Roussey, E. Descrovi, M. Hayrinen, A. Angelini, M. Kuittinen, S. Honkanen, One dimensional photonic crystal with cilindrical geometry, Optics Express 22, 27236-41 (2014).

[6] A. Angelini, P. Munzert, E. Enrico, N. De Leo, L. Scaltrito, L. Boarino, F. Giorgis, E. Descrovi, Surface Wave assisted beaming of light radiation from localized sources, ACS Photonics, 1 (7), 612-17 (2014).

[7] A. Angelini, E. Barakat, P. Munzert, L. Boarino, N. De Leo, E. Enrico, F. Giorgis, H. P. Herzig, C. F. Pirri, E. Descrovi, Focusing and extraction of light mediated by Bloch Surface Waves, Sci. Rep., 4, 5428 (2014).

[8] E. Descrovi, D. Morrone, A. Angelini, F. Frascella, S. Riccia-

rdi, P. Rivolo, N. De Leo, L. Boarino, P. Munzert, F. Michelotti, F. Giorgis, Fluorescence imaging assisted by surface modes on dielectric multilayers, EPJ D, 68, (2014).

[9] A. Angelini, E. Enrico, N. De Leo, P. Munzert, L. Boarino, F. Michelotti, F. Giorgis, and E. Descrovi, Fluorescence diffraction assisted by Bloch Surface Waves on a one dimensional photonic crystal, New J. Phys. 15, 073002 (2013).

[10] E. Descrovi, E. Barakat, A. Angelini, P. Munzert, N. De Leo, L. Boarino, F. Giorgis, and H. P. Herzig, Leakage radiation interference microscopy, Optics Letters, 38(17), 3374-76 (2013).

[11] A. Virga, P. Rivolo, F. Frascella, A. Angelini, E. Descrovi, F. Geobaldo, F. Giorgis, Silver nanoparticles on porous silicon: approaching single molecule detection in resonant SERS regime, J. Phys. Chem. C, 117(39), 20139-45 (2013).

Bibliography

[1] Lord Rayleigh, *On the remarkable phenomenon of crystalline reflexion described by prof. Stokes*, Phil. Mag. S. 5, 26, (1888).

[2] P. Vukusic and R. Sambles, *Photonic structures in biology*, Nature 424, 852-855, (2003).

[3] A. R. Parker and H. E. Townley, *Biomimetics of photonic nanostructures.* Nat. Nanotech. 2, 347-353, (2007).

[4] J. D. Joannopoulos, S. G. Jhonson, J. N. Winn, R. D. Meade, *Photonic Crystals. Molding the flow of light.*, 2^{nd} ed., Princeton Press, Princeton, NJ, (2008).

[5] T. Baba, *Slow light in photonic crystals*, Nature Photonics 2, 465-473, (2008).

[6] T. F. Krauss, *Slow light in photonic crystal waveguides*, J. Phys. D: Appl. Phys. 40, 2666-2670, (2007).

[7] O. Painter, R. K. Lee, A. Scherer, A. Yariv, J. D. O'Brien, P. D. Dapkus, I. Kim, *Two-Dimensional Photonic Band-Gap Defect Mode Laser*, Science 284 (5421), 1819-1921, (1999).

[8] A. A. Erchak, D. J. Ripin, S. Fan, P. Rakich, J. D. Joannopoulos, E. P. Ippen, G. S. Petrich and L. A. Kolodziejski, *Enhanced coupling to vertical radiation using a two-dimensional photonic crystal in a semiconductor light-emitting diode*, Appl. Phys. Lett. 78, 563 (2001).

[9] P. Russell, *Photonic Crystal Fibers*, Science, 299 (5605), 358-362, (2003).

[10] L. Zeng, Y. Yi, C. Hong, J. Liu, N. Feng, X. Duan, L. C. Kimerling and B. A. Alamariu, *Efficiency enhancement in Si solar cells by textured photonic crystal back reflector*, Appl. Phys. Lett. 89, 111111, (2006).

[11] E. Yablonovitch, T. J. Gmitter, R. D. Meade, A. M. Rappe, K. D. Brommer, and J. D. Joannopoulos, *Donor and acceptor modes in photonic band structure*, Phys. Rev. Lett. 67, 3380, (1991).

[12] P. Lalanne C. Sauvan and J. P. Hugonin, *Photon confinement in photonic crystal nanocavities*, Laser and Photonics Reviews 2 (6), 514-526, (2008).

[13] J. D. Joannopoulos, P. R. Villeneuve, S. Fan, *Photonic crystals: putting a new twist on light*, Nature 386, 143-149, (1997).

[14] S. Noda, M. Fujita, T. Asano, *Spontaneous-emission control by photonic crystals and nanocavities*, Nature Photonics 1, 449-458, (2007).

[15] D. Englund, D. Fattal, E. Waks, G. Solomon, B. Zhang, T. Nakaoka, Y. Arakawa, Y. Yamamoto and J. Vuckovic, *Controlling the Spontaneous Emission Rate of Single Quantum Dotsin a Two-Dimensional Photonic Crystal*, PRL 95, 013904, (2005).

[16] P. Lohdal, A. F. van Driel, I. S. Nikolaev, A. Irman, K. Overgaag, D. Vanmaekelbergh and W. L. Vos, *Controlling the dynamics of spontaneous emission from quantum dots by photonic crystals.*, Nature 430, 654-657, (2004).

[17] E. M. Purcell, Phys. Rev. 69, 681, (1946).

[18] E. Descrovi, T. Sfez, L. Dominici, W. Nakagawa, F. Michelotti, F. Giorgis and H. P. Herzig, *Near-field imaging of Bloch surface waves on silicon nitride one-dimensional photonic crystals*, Opt. Expr. 16 (8), 5453-5464, (2008).

[19] W. M. Robertson, G. Arjavalingam. R. D. Meade, K. D. Brommer, A. M. Rappe, and J. D. Joannopoulos, *Observation of surface photons on periodic dielectric arrays*, Opt. Lett. 18, 528-530 (1993).

[20] D. Artigas and L. Torner, *Dyakonov Surface Waves in Photonic Metamaterials*, Phys. Rev. Lett. 94, 013901, (2005).

[21] H. Raether, *Surface Plasmons*, Springer-Verlag, Berlin (1988).

[22] R. D. Maede, K. D. Brommer, A. M. Rappe and J. D. Joannopoulos, *Electromagnetic Bloch Waves at the surface of a photonic crystal* Phys. Rev. B, 44, 109601, (1995).

[23] E. Descrovi, T. Sfez, M. Quaglio, D. Brunazzo, L. Dominici, F. Michelotti, H. P. Herzig, O. J. F. Martin and F. Giorgis, *Guided Bloch surface waves on ultrathin polymeric ridges*, Nano Lett. 10, 2087-2091 (2012).

[24] N. Ganesh, I. D. Block and B. T. Cunningham, *Near ultraviolet-wavelength photonic-crystal biosensor with enhanced surface-to-bulk sensitivity ratio*, Appl. Phys. Lett. 89, 023901, (2006).

[25] L. Yu, E. Barakat, T. Sfez, L. Hvozdara, J. Di Francesco and H. P. Herzig, *Manipulating Bloch surface waves in 2D: a platform concept-based flat lens*, Light: Sci. Appl. 3, e124, (2013).

[26] M. Ballarini, F. Frascella, F. Michelotti, G. Digregorio, P. Rivolo, V. Paeder, V. Musi, F. Giorgis and E. Descrovi *Bloch surface waves-controlled emission of organic dyes grafted on a one-dimensional photonic crystal*, Appl. Phys. Lett 99, 043302 (2011).

[27] F. Michelotti, B. Sciacca, L. Dominici, M. Quaglio, E. Descrovi, F. Giorgisw and F. Geobaldo, *Fast optical vapour sensing by Bloch surface waves on porous silicon membranes*, Phys. Chem. Chem. Phys 12, 502-506, (2010).

[28] B. Hecht, H. Bielefeldt, L. Novotny, Y. Inouye and D. W. Pohl, *Local excitation, scattering, and interference of surface plasmons*, Phys. Rev. Lett. 77 (9), 1889, 1996.

[29] T. Sfez, E. Descrovi, L. Yu, D. Brunazzo, M. Quaglio, L. Dominici, W. Nakagawa, F. Michelotti, F. Giorgis, O. J. F. Martin and H. P. Herzig, *Bloch surface waves in ultrathin waveguides: near-field investigation of mode polarization and propagation*, JOSA B, 27 (8), 1617-1625, (2010).

[30] X. Wu, E. Barakat, L. Yu, L. Sun, J. Wang, Q. Tan, H. P. Herzig *Phase-sensitive near field Investigation of Bloch surface wave propagation in curved waveguides.* JEOS - RP, Europe, v. 9, oct. 2014. ISSN 1990-2573.

[31] A. Drezet, A. Hohenau, D. Koller, A. Stepanov, H. Ditlbacher, B. Steinberger, F. R. Aussenegg, A. Leitner, J. R. Krenn, *Leakage radiation microscopy of surface plasmon polaritons*, Mat. Sci.Eng. B 149, 220-229, (2008).

[32] A. Angelini, E. Enrico, N. De Leo, P. Munzert, L. Boarino, F. Michelotti, F. Giorgis and E. Descrovi, *Fluorescence diffraction assisted by Bloch surface waves on a one-dimensional photonic crystal*, New J. Phys. 15, 073002, (2013).

[33] E. Descrovi, F. Giorgis, L. Dominici and F. Michelotti, *Experimental observation of optical bandgaps for surface electromagnetic waves in a periodically corrugated one-dimensional silicon nitride photonic crystal*, Opt. Lett. 33 (3), 243-245, (2008).

[34] E. Descrovi, E. Barakat, A. Angelini, P. Munzert, N. De Leo, L. Boarino, F. Giorgis and H. P. Herzig, *Leakage radiation interference microscopy*, Opt. Lett. 38 (17), 3374-3376, (2013).

[35] M. S. Kim, T. Scharf, C. Etrich, C. Rockstuhl, and H. P. Herzig, *Longitudinal-differential interferometry: direct imaging of axial superluminal phase propagation.*, Opt. Lett. 37 (3), 305-307 (2012).

[36] J. Schwider, R. Burow, K. E. Elssner, J. Grzanna, R. Spolaczyk, and K. Merkel, *Digital wave-front measuring interferometry: some systematic error sources* Appl. Opt. 22 , 3421 (1983).

[37] P. Hariharan, B. F. Oreb, and T. Eiju,*Digital phase-shifting interferometry: a simple error-compensating phase calculation algorithm* Appl. Opt. 26 , 2504 (1987).

[38] A. Berrier, M. Swillo, N. Le Thomas, R. Houdre', and S. Anand, *Bloch mode excitation in two-dimensional photonic crystals imaged by Fourier optics* Phys. Rev. B 79 , 165116 (2009).

[39] W. L. Barnes, A. Dereux and T. W. Ebbesen, *Surface Plasmon subwavelength optics*, Nature 424, 824-830, (2003).

[40] J.-M. Yi, A. Cuche, E. Devaux, C. Genet, and T. W. Ebbesen, *Beaming Visible Light with a Plasmonic Aperture Antenna*, ACS Phot. 1, 365-370, (2014).

[41] T. Sfez, E. Descrovi, L. Yu, M. Quaglio, L. Dominici, W. Nakagawa and F. Michelotti, *Two-dimensional optics on silicon nitride multilayer: Refraction of Bloch surface waves*, Appl. Phys. Lett. 96, 151101, (2010).

[42] A. Angelini, E. Barakat, P. Munzert, L. Boarino, N. De Leo, E. Enrico, F. Giorgis, H. P. Herzig, C. F. Pirri, E. Descrovi, *Focusing and Extraction of Light mediated by Bloch Surface Waves*, Sci. Rep. 4, 5428, (2014).

[43] M. Liscidini, J. E. Sipe, *Analysis of Bloch-surface-wave assisted diffraction-based biosensors*, JOSAB 26 (2), 279-289, (2009).

[44] T. Holmgaard and S. I. Bozhevolnyi, *Theoretical analysis of dielectric-loaded surface plasmon-polariton waveguides*, Phys. Rev. B 75, 245405, (2007).

[45] E. Descrovi, F. Frascella, B. Sciacca, F. Geobaldo, L. Dominici, F. Michelotti, *Coupling of surface waves in highly defined one-dimensional porous silicon photonic crystals for gas sensing applications*, Appl. Phys. Lett. 91, 241109 (2007).

[46] S. Santi, V. Musi, E. Descrovi, V. Paeder, J. Di Francesco, L. Hvozdara, P. van der Wal, H. A. Lashuel, A. Pastore, R. Neier, H. P. Herzig, *Real-time Amyloid Aggregation Monitoring with a Photonic Crystal-based Approach*, Chem. Phys. Chem. 14, 3476-82, (2013).

[47] C. Zhao and J. Zhang, *Plasmonic Demultiplexer and Guiding*ACS Nano 4 , 6433 (2010).

[48] R. Ulrich, *Theory of the Prism-Film Coupler by Plane-Wave Analysis*, J. Opt. Soc. Am. 60 , 1337 (1970).

[49] F. Michelotti, A. Sinibaldi, P. Munzert, N. Danz, and E. Descrovi *Probing losses of dielectric multilayers by means of Bloch surface waves*, Opt. Lett. 38, 616-618, (2013).

[50] A. Angelini, A. Lamberti, S. Ricciardi, F. Frascella, P. Munzert, N. De Leo and E. Descrovi, *In-plane 2D focusing of surface waves by ultrathin refractive structures*, Opt. Lett. 39 (22), 6391-6394, (2014).

[51] M. Ballarini, F. Frascella, N. De Leo, S. Ricciardi, P. Rivolo, P. Mandracci, E. Enrico, F. Giorgis, F. Michelotti, and E. Descrovi, *A polymer-based functional pattern on one-dimensional photonic crystals for photon sorting of fluorescence radiation* Opt. Express 20 , 6703 (2012).

[52] G.M. Lerman, A. Yanai and U. Levy, *Demonstration of nanofocusing by the use of plasmonic lens illuminated with radially polarized light* Nano Lett. 9, 2139-2143, (2009).

[53] Z. Liu, J. M. Steele, W. Srituravanich, Y. Pikus, C. Sun and X. Zhang, *Focusing surface plasmons with a plasmonic lens*, Nano Lett. 5, 1726-1729, (2005).

[54] R. S. Meltzer, S. P. Feofilov, B. Tissue and H. B. Yuan, *Dependence of fluorescence lifetimes of* $Y_2O_3 : Eu_3^+$ *nanoparticles on the surrounding medium*, Phys. Rev. B 60, R14012(R), (1999).

[55] M. Megens, J. E. G. J. Wijnhoven, A. Lagendijk and W. L. Vos, *Fluorescence lifetimes and linewidths of dye in photonic crystals* Phys. Rev. A 59, 4727, (1999).

[56] N. Ganesh, W. Zhang, P. C. Mathias, E. Chow, J. A. N. T. Soares, V. Malyarchuk, A. D. Smith and B. T. Cunningham, *Enhanced fluorescence emission from quantum dots on a photonic crystal surface*, Nat. Nanotech, 2, 515-520, (2007).

[57] I. D. Block, L. L. Chan, B. T. Cunningham, *Photonic crystal optical biosensor incorporating structured low-index porous dielectric*, Sens. and Act. B 120, 187-193, (2006).

[58] W.-H. Chang, W.-Y. Chen, H.-S. Chang, T.-P. Hsieh, J.-I. Chyi and T. Hsu, *Efficient Single-Photon Sources Based on Low-Density Quantum Dots in Photonic-Crystal Nanocavities*, Phys. Rev. Lett. 96, 117401, (2006).

[59] K. G. Lee, X. W. Chen, H. Eghlidi, P. Kukura, R. Lettow, A. Renn, V. Sandoghdar and S. Gotzinger, *A planar dielectric antenna for directional single-photon emission and near-unity collection efficiency.*, Nat. Photon. 5, 166-169, (2011).

[60] L. Novotny and N. F. Van Hulst, *Antennas for light*, Nat. Photon. 5, 83-90, (2011).

[61] J. R. Lakowicz, *Radiative decay engineering 3. Surface plasmon-coupled directional emission*, An. Biochem. 324 (2), 153-169, (2004).

[62] R. Badugu, K. Nowazcyk, E. Descrovi, J. R. Lakowicz, *Radiative decay engineering 6: Fluorescence on one-dimensional photonic crystals.*, An. Biochem. 442 (1), 83-96, (2013).

[63] C. J. Regan, O. Thiabgoh, L. Grave de Peralta, and A.A. Bernussi, *Probing photonic Bloch wavefunctions with plasmon-coupled leakage radiation*, Opt. Expr. 20 (8), 8658-8666, (2012).

[64] S.P. Frisbie, C.J. Regan, A. Krishnan, C. Chesnutt, J. Ajimo, A.A. Bernussi and L. Grave de Peralta, *Characterization of polarization states of surface plasmon polariton modes by Fourier-plane leakage microscopy*, Opt. Comm. 283 (24), 5255-5260, (2010).

[65] Y. C. Jun, K. C.Y. Huang and M. L. Brongersma*Plasmonic beaming and active control over fluorescent emission*, Nat. Comm. 2, 283, (2011).

[66] H. Li, S. Xu, Y. Gu, H. Wang, R. Ma, J. R. Lombardi and W. Xu, *Active Plasmonic Nanoantennas for Controlling Fluorescence Beams*, J. Phys. Chem. C 117, 19154-19159, (2013).

[67] R. Esteban, T. V. Teperik, and J. J. Greffet, *Optical Patch Antennas for Single Photon Emission Using Surface Plasmon Resonances*, Phys. Rev. Lett. 104, 026802, (2010).

[68] C. J. Regan, R. Rodriguez, S. C. Gourshetty, L. Grave de Peralta, and A. A. Bernussi, *Imaging nanoscale features with plasmon-coupled leakage radiation far-field superlenses*, Opt. Expr. 20 (19), 20827-20834, (2014).

[69] M. F. Templin, D. Stoll, M. Schrenk, P.C Traub, C.F. VÃ¶hringer and T.O. Joos, *Protein microarray technology* Trend Biotechnol 20, 160, (2002).

[70] K. Iida and I. Nishimura, *Gene expression profiling by DNA microarray technology* Crit. Rev. Oral Biol. Med. 13, 35, (2002).

[71] C.R. Taitt, G.P. Anderson and F. S. Ligler, *Evanescent wave fluorescence biosensors* Biosens. Bioelectron. 20, 2470, (2005).

[72] J.R. Lakowicz, *Principles of Fluorescence Spectroscopy Third Edition*, Springer, (2006).

[73] L. A. Tessler and R.D. Mitra,*Sensitive single molecule protein quantification and protein complex detection in a microarray format*, Proteomics 11, 4 (2011).

[74] S. George, V. Chaudhery, M. Lu, M. Takagi, N. Amro, A. Pokhriyal, Y. Tan, P. Ferreira and B. T. Cunningham, *Sensitive detection of protein and miRNA cancer biomarkers using silicon-based photonic crystals and a resonance coupling laser scanning platform.* Lab Chip 13, 4053, (2013).

[75] H. Aouani, O. Mahboub, E. Devaux, H. Rigneault, T. W. Ebbesen, J. Wenger, *Plasmonic antennas for directional sorting of fluorescence emission*, Nano Lett. 11 (6), 2400-2406, (2011).

[76] H. Aouani, O. Mahboub, E. Devaux, H. Rigneault, T. W. Ebbesen, and J. Wenger*Large molecular fluorescence enhancement by a nanoaperture with plasmonic corrugations*, Opt. Expr. 19(14), 13056-13062, (2011).

[77] S. G. Aberra, J. Laverdant, C. Symonds, S. Vignoli and J. Bellessa *Spatial coherence properties of surface plasmon investigated by Young's slit experiment* Opt. Lett. 37, 2139-41, (2012).

[78] S. G. Aberra, J. Laverdant, C. Symonds, S. Vignoli, F. Bessueille and J. Bellessa, *Influence of surface plasmon propagation on leakage radiation microscopy imaging* Appl. Phys. Lett. 101, 123106, (2012).

[79] G. Rui, D. C. Abeysinghe, R. L. Nelson and Q. Zhan, *Demonstration of beam steering via dipole-coupled plasmonic spiral antenna.* Sci. Rep. 3, 2237 (2013).

[80] H. Aouani, O. Mahboub, N. Bonod, E. Devaux, E. Popov, H. Rigneault, T. W. Ebbesen, J. Wenger, *Bright unidirectional emission of molecules in a nanoaperture with surface corrugations.* Nano Lett. 11, 637-644 (2011).

[81] L. Han, D. Zhang, Y. Chen, R. Wang, L. Zhu, P. Wang, H. Ming, R. Badugu and J. R. Lakowicz, *Polymer-loaded propagating modes on a one-dimensional photonic crystal.*, Appl. Phys. Lett. 104, 061115 (2014).

[82] H. L. Offerhaus, B. van den Bergen, M. Escalante, F. B. Segerink, J. P. Korterik, and N. F. van Hulst, *Creating focused plasmons by noncollinear phasematching on functional gratings.*, Nano Lett. 5, 2144-2148, (2005).

[83] S. Kim, H. Kim, Y. Lim, B. Lee, *Off-axis directional beaming of optical field diffracted by a single subwavelength metal slit with asymmetric dielectric surface gratings*, Appl. Phys. Lett. 90, 051113, (2007).

[84] H. J. Lezec, A. Degiron, E. Deveaux, R. A. Linke, L. Martin-Moreno, F. J. Garcia-Vidal, T. W. Ebbesen, *Beaming light from a subwavelength aperture*, Science 297, 820-822, (2002).

[85] R. Lopez-Boada, C. Regan, D. Dominguez, A. Bernussi, L. Grave de Peralta, *Fundaments of optical far-field subwavelength resolution based on illumination with surface waves*, Opt. Expr. 21, 11928-11942, (2013).